

2

POR-2025(EX)
(WT-2025)(EX)
EXTRACTED VERSION

AD-A995 427

OPERATION DOMINIC, FISH BOWL SERIES

Project Officer's Report—Project 6.6

Long-Term Observations by Resonance Scattering Techniques

**E. R. Manring, Project Officer
Geophysics Corporation of America
Bedford, MA**

**DTIC
ELECTE
JUN 19 1986**

4 September 1964

NOTICE:

**This is an extract of POR-2025 (WT-2025), Operation DOMINIC, Fish Bowl Series,
Project 6.6.**

**Approved for public release;
distribution is unlimited.**

DTIC FILE COPY

**Extracted version prepared for
Director
DEFENSE NUCLEAR AGENCY
Washington, DC 20305-1000**

1 September 1985

86 6 19 001

AD-A995417

REPORT DOCUMENTATION PAGE

1a. REPORT SECURITY CLASSIFICATION UNCLASSIFIED		1b. RESTRICTIVE MARKINGS	
2a. SECURITY CLASSIFICATION AUTHORITY		3. DISTRIBUTION/AVAILABILITY OF REPORT Approved for public release; distribution is unlimited.	
2b. DECLASSIFICATION/DOWNGRADING SCHEDULE		5. MONITORING ORGANIZATION REPORT NUMBER(S) POR-2025 (EX) (WT-2025) (EX)	
4. PERFORMING ORGANIZATION REPORT NUMBER(S)		7a. NAME OF MONITORING ORGANIZATION Defense Atomic Support Agency	
6a. NAME OF PERFORMING ORGANIZATION Geophysics Corp. of America	6b. OFFICE SYMBOL (if applicable)	7b. ADDRESS (City, State, and ZIP Code) Washington, DC	
6c. ADDRESS (City, State, and ZIP Code) Bedford, Massachusetts		9. PROCUREMENT INSTRUMENT IDENTIFICATION NUMBER	
8a. NAME OF FUNDING/SPONSORING ORGANIZATION	8b. OFFICE SYMBOL (if applicable)	10. SOURCE OF FUNDING NUMBERS	
9c. ADDRESS (City, State, and ZIP Code)		PROGRAM ELEMENT NO.	PROJECT NO.
		TASK NO.	WORK UNIT ACCESSION NO.
11. TITLE (Include Security Classification) OPERATION DOMINIC, FISH BOWL SERIES; PROJECT OFFICER'S REPORT, PROJECT 6.6 - Long-Term Observations by Resonance Scattering Techniques, Extracted Version			
12. PERSONAL AUTHOR(S) E. R. Manring			
13a. TYPE OF REPORT	13b. TIME COVERED FROM TO	14. DATE OF REPORT (Year, Month, Day) 640904	15. PAGE COUNT 334
16. SUPPLEMENTARY NOTATION This report has had sensitive military information removed in order to provide an unclassified version for unlimited distribution. The work was performed by the Defense Nuclear Agency in support of the DoD Nuclear Test Personnel Review Program.			
17. COSATI CODES		18. SUBJECT TERMS (Continue on reverse if necessary and identify by block number)	
FIELD	GROUP	Dominic Blue Gill Star Fish	
18	3	Fish Bowl King Fish Tight Rope	
		Scattering Check Mate	
19. ABSTRACT (Continue on reverse if necessary and identify by block number) Some of the apparent conclusions of this project are (1) low-yield, low-altitude devices do not lend themselves to a study by resonance scatter techniques; (2) devices such as King Fish, Star Fish, very high yield weapons at 50 km or higher, and low-yield weapons salted with an appropriate material, give debris concentrations which can be followed for many days and over wide geographical areas; (3) an inventory of material cannot be made with a neutral species, unless the degree of ionization is established by independent techniques. Another species for which the neutral and ionized state can be observed should largely remove this uncertainty; (4) diffusion is an important mechanism for the long-term spread of debris over wide areas; and (5) early time observations were made but have not been studied. This data includes Tight Rope and some of the air drops.			
20. DISTRIBUTION/AVAILABILITY OF ABSTRACT <input checked="" type="checkbox"/> UNCLASSIFIED/UNLIMITED <input type="checkbox"/> SAME AS RPT. <input type="checkbox"/> DTIC USERS		21. ABSTRACT SECURITY CLASSIFICATION UNCLASSIFIED	
22a. NAME OF RESPONSIBLE INDIVIDUAL MARK D. FLOHR		22b. TELEPHONE (Include Area Code) 202-325-7559	22c. OFFICE SYMBOL DNA/ISCM

FOREWORD

Classified material has been removed in order to make the information available on an unclassified, open publication basis, to any interested parties. The effort to declassify this report has been accomplished specifically to support the Department of Defense Nuclear Test Personnel Review (NTPR) Program. The objective is to facilitate studies of the low levels of radiation received by some individuals during the atmospheric nuclear test program by making as much information as possible available to all interested parties.

The material which has been deleted is either currently classified as Restricted Data or Formerly Restricted Data under the provisions of the Atomic Energy Act of 1954 (as amended), or is National Security Information, or has been determined to be critical military information which could reveal system or equipment vulnerabilities and is, therefore, not appropriate for open publication.

The Defense Nuclear Agency (DNA) believes that though all classified material has been deleted, the report accurately portrays the contents of the original. DNA also believes that the deleted material is of little or no significance to studies into the amounts, or types, of radiation received by any individuals during the atmospheric nuclear test program.

UNANNOUNCED

Accession For	
NTIS CRA&I	<input checked="" type="checkbox"/>
DTIC TAB	<input type="checkbox"/>
Unannounced	<input type="checkbox"/>
Justification	
By	
Distribution /	
Availability Codes	
Dist	Avail and/or Special
A-1	



OPERATION DOMINIC

FISH BOWL SERIES

PROJECT OFFICERS REPORT—PROJECT 6.6

**LONG-TERM OBSERVATIONS BY RESONANCE
SCATTERING TECHNIQUES**

Edward R. Manring, Project Officer

**Geophysics Corporation of America
Bedford, Massachusetts**

This document is the author(s) report to the Director, Defense Atomic Support Agency, of the results of experimentation sponsored by that agency during nuclear weapons effects testing. The results and findings in this report are those of the author(s) and not necessarily those of the DOD. Accordingly, reference to this material must credit the author(s). This report is the property of the Department of Defense and, as such, may be reclassified or withdrawn from circulation as appropriate by the Defense Atomic Support Agency.

DEPARTMENT OF DEFENSE
WASHINGTON, D.C. 20301

ABSTRACT

Ten sites were equipped to observe resonance-scattered sunlight from selected debris species. These species were ionized and neutral barium, and neutral zirconium. The measurements were performed during twilight periods when the sky background was low and debris in the high atmosphere was sunlit. In general, debris was detectable by this technique only above heights of approximately ninety km.

Barium and zirconium were observed in small amounts in the Johnston Island area after Check Mate, King Fish, and Star Fish.

The measurements performed on the first twilight following Star Fish and King Fish are indicative of the detonation-induced motions of debris. Measurements on subsequent twilights gave information on the spread of debris by diffusion and wind transport.

CONTENTS

ABSTRACT -----	5
CHAPTER 1 INTRODUCTION -----	13
1.1 Objectives -----	13
1.2 Background -----	15
1.3 Theory -----	17
1.3.1 Signal Intensity and Signal-to-Noise Considerations -----	17
1.3.2 Backgrounds -----	27
1.3.3 Effects of Atmospheric Attenuation -----	34
1.3.4 Determination of the Relative Intensity of Photon Flux Caused by Nuclear Debris— Resonance Scattering -----	36
CHAPTER 2 PROCEDURE -----	48
2.1 Operations -----	48
2.2 Instrumentation -----	50
2.2.1 Filters -----	50
2.2.2 Photometer Background -----	61
2.2.3 Birefringent Photometers -----	62
2.2.4 Four-Barrel Interference Photometers -----	69
2.2.5 Photometer Accessories -----	71
2.2.6 Calibrations -----	72
CHAPTER 3 DATA PROCESSING -----	87
3.1 Data Reduction -----	87
3.1.1 Birefringent Photometers -----	88
3.1.2 Four-Barrel Photometers -----	90
3.2 Arithmetical Operations -----	92
CHAPTER 4 OBSERVATIONS AND RESULTS -----	96
4.1 Blue Gill -----	96
4.1.1 S-1, Summit County -----	97
4.1.2 Johnston Island -----	97
4.1.3 French Frigate Shoals -----	98
4.1.4 S-2, Henry County -----	98
4.1.5 S-4, Point Barrow -----	98
4.1.6 Tutuila and Tongatapu -----	99
4.1.7 Wake -----	99
4.1.8 Midway -----	99
4.2 King Fish -----	99
4.2.1 French Frigate Shoals -----	100

4.2.2 Wake	100
4.2.3 Tutuila	101
4.2.4 Midway	102
4.2.5 Johnston Island, S-2 and S-4	102
4.2.6 S-1, Summit County	104
4.2.7 Tongatapu	104
4.3 Check Mate	105
4.4 Star Fish	105
4.4.1 S-5	106
4.4.2 Johnston Island, S-2, and S-4	106
4.4.3 Wake	107
4.4.4 French Frigate Shoals and S-1	107
4.4.5 Tutuila and Tongatapu	107
4.4.6 Midway	108
4.5 Tight Rope	109
CHAPTER 5 DISCUSSION	233
CHAPTER 6 CONCLUSIONS AND RECOMMENDATIONS	247
6.1 Conclusions	247
6.2 Recommendations	248
APPENDIX A EFFECTS OF ATMOSPHERIC ATTENUATION	251
A.1 Introduction	251
A.2 Differential Refraction	256
A.2.1 General Discussion	256
A.2.2 Ray and Shadow Heights	261
A.2.3 Attenuation by Variable Refraction	264
A.3 Effects of Scattering	266
A.3.1 General Description	266
A.3.2 Rayleigh Scattering	267
A.3.3 Mie Scattering	269
A.4 Ozone Absorption	272
A.5 Total Atmospheric Attenuation	273
APPENDIX B AN EVALUATION OF THE CONCENTRATIONS	297
APPENDIX C DETERMINATION OF THE RELATIVE INTENSITY OF PHOTON FLUX CAUSED BY NUCLEAR DEBRIS-RESONANCE SCATTERING	311
C.1 General Equation for the Photon Flux	311
C.2 Determination of Abundance of Fission Products	313
C.3 Determination of Resonance Absorption Cross Section	315
C.4 Discussion	316
REFERENCES	326

TABLES

1.1 Solar Photon Flux Outside the Atmosphere -----	37
1.2 Transition Probabilities -----	38
1.3 Absolute Intensities of the Basic Night Sky Emissions -----	39
4.1 Island Locations -----	109
4.2 Location of Ships for Events -----	110
4.3 Sky Conditions, French Frigate Shoals, Wake, and Tutuila, King Fish -----	111
4.4 Sky Conditions, Midway and Johnston, King Fish -----	113
4.5 King Fish, French Frigate Shoals, 1 November 1962, AM -----	115
4.6 King Fish, French Frigate Shoals, 1 November 1962, PM -----	116
4.7 King Fish, French Frigate Shoals, 2 November 1962, AM -----	117
4.8 King Fish, French Frigate Shoals, 2 November 1962, PM -----	119
4.9 King Fish, French Frigate Shoals, 3 November 1962, PM -----	120
4.10 King Fish, French Frigate Shoals, 4 November 1962, AM -----	121
4.11 King Fish, French Frigate Shoals, 4 November 1962, PM -----	122
4.12 King Fish, French Frigate Shoals, 5 November 1962, AM -----	123
4.13 King Fish, French Frigate Shoals, 5 November 1962, PM -----	124
4.14 King Fish, French Frigate Shoals, 6 November 1962, AM -----	125
4.15 King Fish, French Frigate Shoals, 6 November 1962, PM -----	126
4.16 King Fish, French Frigate Shoals, 7 November 1962, AM -----	127
4.17 King Fish, Wake, 3 November 1962, AM -----	128
4.18 King Fish, Wake, 3 November 1962, PM -----	129
4.19 King Fish, Wake, 4 November 1962, AM -----	130
4.20 King Fish, Wake, 4 November 1962, PM -----	131
4.21 King Fish, Wake, 5 November 1962, AM -----	132
4.22 King Fish, Wake, 5 November 1962, PM -----	133
4.23 King Fish, Wake, 6 November 1962, AM -----	134
4.24 King Fish, Tutuila, 1 November 1962, AM -----	135
4.25 King Fish, Tutuila, 4 November 1962, AM -----	136
4.26 King Fish, Tutuila, 7 November 1962, AM -----	137
4.27 King Fish, Tutuila, 8 November 1962, AM -----	138
4.28 King Fish, Tutuila, 11 November 1962, AM -----	139
4.29 King Fish, Midway, 1 November 1962, AM -----	140
4.30 King Fish, Midway, 1 November 1962, PM -----	141
4.31 King Fish, Midway, 2 November 1962, AM -----	143
4.32 King Fish, Midway, 3 November 1962, PM -----	145
4.33 King Fish, Midway, 4 November 1962, AM -----	146
4.34 King Fish, Midway, 4 November 1962, PM -----	147
4.35 King Fish, Midway, 5 November 1962, AM -----	148
4.36 King Fish, Midway, 5 November 1962, PM -----	150
4.37 King Fish, Midway, 6 November 1962, AM -----	152
4.38 King Fish, Midway, 6 November 1962, PM -----	154
4.39 King Fish, Midway, 7 November 1962, PM -----	156
4.40 King Fish, Midway, 8 November 1962, AM -----	157
4.41 King Fish, Midway, 8 November 1962, PM -----	158
4.42 King Fish, Midway, 9 November 1962, PM -----	159
4.43 King Fish, Johnston Island, 1 November 1962, AM -----	160
4.44 King Fish, Johnston Island, 1 November 1962, PM -----	161

4.45	King Fish, Johnston Island, 2 November 1962, AM-----	162
4.46	King Fish, Johnston Island, 3 November 1962, AM-----	163
4.47	King Fish, Johnston Island, 3 November 1962, PM-----	164
4.48	King Fish, Johnston Island, 4 November 1962, AM-----	165
4.49	King Fish, Johnston Island, 5 November 1962, AM-----	166
4.50	Sky Conditions, Star Fish-----	167
4.51	Star Fish, S-5, 9 July 1962, AM-----	169
4.52	Star Fish, S-5, 9 July 1962, PM-----	172
4.53	Star Fish, S-5, 10 July 1962, AM-----	173
4.54	Star Fish, S-5, 10 July 1962, PM-----	174
4.55	Star Fish, S-5, 11 July 1962, AM-----	175
4.56	Star Fish, S-5, 11 July 1962, PM-----	176
4.57	Star Fish, S-5, 12 July 1962, AM-----	177
4.58	Star Fish, Tutuila, 9 July 1962, AM-----	178
4.59	Star Fish, Tutuila, 10 July 1962, AM-----	179
4.60	Star Fish, Tutuila, 10 July 1962, PM-----	180
4.61	Star Fish, Midway, 9 July 1962, AM-----	181
4.62	Star Fish, Midway, 9 July 1962, PM-----	183
4.63	Star Fish, Midway, 10 July 1962, PM-----	183
4.64	Star Fish, Midway, 11 July 1962, AM-----	184
4.65	Star Fish, Midway, 11 July 1962, PM-----	186
4.66	Star Fish, Midway, 12 July 1962, AM-----	187
4.67	Star Fish, Midway, 12 July 1962, PM-----	189
4.68	Star Fish, Midway, 13 July 1962, AM-----	190
4.69	Star Fish, Midway, 13 July 1962, PM-----	191
4.70	Star Fish, Midway, 15 July 1962, AM-----	192
4.71	Star Fish, Midway, 15 July 1962, PM-----	193
4.72	Star Fish, Midway, 17 July 1962, PM-----	194
4.72	Star Fish, Johnston Island, 9 July 1962, AM-----	194
A.1	Non-Refracted Ray Heights (km)-----	280
A.2	Refracted Ray Heights (km)-----	281
A.3	Refractive Diminution Factors, $F/F_0 = d/D(\delta)$ -----	282
A.4	Rayleigh Scattering Optical Depths-----	283
A.5	Mie Scattering Optical Depths, Cloud-Free Atmosphere-----	283
A.6	Mie Scattering Optical Depths, Cloudy Atmosphere-----	284
A.7	Ozone Optical Thickness-----	285
C.1	Fission Yields per Mass Number-----	319
C.2	Relative Abundance of Different Elements-----	323
C.3	Resonance Lines of Elements-----	325

FIGURES

1.1	Birefringent photometer-----	40
1.2	Four-barrel interference photometer-----	41
1.3	Computed and measured values of the radiance of the sky at sunset-----	42
1.4	Computed values of the radiance of the sky due to molecular scattering only-----	43
1.5	Average diffuse radiation from zenith, 0.3 to 1.3 microns-----	44
1.6	Atmospheric attenuation geometry-----	45

1.7 Atmospheric transmission coefficient versus height, for 8° depression angle -----	46
1.8 Atmospheric transmission coefficient versus height, for 14° depression angle-----	47
2.1 Shift in position of passband of an interference filter as a function of incidence angle -----	78
2.2 Broadening of the passband of an interference filter as a function of incidence angle and wavelength shift -----	78
2.3 Birefringent photometer block diagram -----	79
2.4 Power supply, front view -----	80
2.5 Power supply, inside removed -----	81
2.6 Two-channel Sanborn recorder (birefringent photometer) -----	82
2.7 Block diagram of four-barrel interference photometer -----	83
2.8 Interference power unit, open view -----	84
2.9 Four-barrel interference photometer with attached power unit -----	85
2.10 Eight-channel Sanborn recorder (interference photometer)-----	86
3.1 Typical recordings from birefringent unit at northern conjugate point, S-5 -----	95
4.1 Particle density, French Frigate Shoals, T + 3 and 39 hours, King Fish -----	195
4.2 Particle density, French Frigate Shoals, T + 15 and 27 hours, King Fish -----	196
4.3 Particle density, French Frigate Shoals, T + 63 and 75 hours, King Fish -----	197
4.4 Particle density, French Frigate Shoals, T + 87 and 99 hours, King Fish -----	198
4.5 Particle density, French Frigate Shoals, T + 111 and 123 hours, King Fish -----	199
4.6 Particle density, French Frigate Shoals, T + 135 and 147 hours, King Fish -----	200
4.7 Particle density, Wake, T + 41 and 53 hours, King Fish -----	201
4.8 Particle density, Wake, T + 65 and 77 hours, King Fish -----	202
4.9 Particle density, Wake, T + 89 and 101 hours, King Fish -----	203
4.10 Particle density, Tutuila, T + 4 and 76 hours, King Fish -----	204
4.11 Particle density, Tutuila, T + 148 and 172 hours, King Fish -----	205
4.12 Particle density, Tutuila, T + 244 hours, King Fish -----	206
4.13 Particle density, Midway, T + 4 hours, King Fish -----	207
4.14 Particle density, Midway, T + 16 and 28 hours, King Fish -----	208
4.15 Particle density, Midway, T + 64 and 76 hours, King Fish -----	209
4.16 Particle density, Midway, T + 88 and 100 hours, King Fish -----	210
4.17 Particle density, Midway, T + 112 and 124 hours, King Fish -----	211
4.18 Particle density, Midway, T + 136 hours, King Fish -----	212
4.19 Particle density, Midway, T + 160 and 172 hours, King Fish -----	213
4.20 Particle density, Midway, T + 184 and 208 hours, King Fish -----	214
4.21 Particle density, Johnston Island, T + 3 and 27 hours, King Fish-----	215
4.22 Particle density, Johnston Island, T + 15 and 51 hours, King Fish -----	216
4.23 Particle density, Johnston Island, T + 63 and 75 hours, King Fish -----	217
4.24 Particle density, Johnston Island, T + 99 hours, King Fish -----	218

4.25 Barium and zirconium, density versus height, Johnston Island, 1 November 1962	219
4.26 Particle density, S-5, T+6 hours, Star Fish	220
4.27 Particle density, S-5, T+18 and 30 hours, Star Fish	221
4.28 Particle density, S-5, T+42 and 54 hours, Star Fish	222
4.29 Particle density, S-5, T+66 and 78 hours, Star Fish	223
4.30 Particle density, Tutuila, T+7 and 43 hours, Star Fish	224
4.31 Particle density, Tutuila, T+31 hours, Star Fish	225
4.32 Particle density, Midway, T+7 and 19 hours, Star Fish	226
4.33 Particle density, Midway, T+43 and 55 hours, Star Fish	227
4.34 Particle density, Midway, T+67 and 79 hours, Star Fish	228
4.35 Particle density, Midway, T+103 hours, Star Fish	229
4.36 Particle density, Midway, T+115 and 151 hours, Star Fish	230
4.37 Particle density, Midway, T+163 and 201 hours, Star Fish	231
4.38 Particle density, Johnston Island, T+6 hours, Star Fish	232
5.1 Concentration profile, R = 0 km	240
5.2 Concentration profile, R = 100 km	241
5.3 Concentration profile, R = 300 km	242
5.4 Concentration profile, R = 600 km	243
5.5 Concentration profile, R = 1000 km	244
A.1 General geometry of debris observations	286
A.2 Index of refraction as a function of altitude	287
A.3 Passage of light ray through the refracting atmosphere	288
A.4 Ray heights and refractive separations	288
A.5 Method of ray path tracing	289
A.6 Ozone concentration models	290
A.7 Solar illumination curves, 6° solar depression angle	291
A.8 Solar illumination curves, 9° solar depression angle	292
A.9 Solar illumination curves, 12° solar depression angle	293
A.10 Solar illumination curves, 15° solar depression angle	294
A.11 Upper atmospheric debris model	295
A.12 Photometric signal levels as a function of solar depression	296
B.1 Solar illumination coefficient (ϵ); average values for SDA 6 through 16 degrees	307
B.2 Density distribution, Case I	308
B.3 Density distribution, Case II	309
B.4 Density distribution, Case III	310

CHAPTER 1

INTRODUCTION

1.1 OBJECTIVES

The primary objective of this project was the measurement of the amount of selected nuclear debris constituents above observing sites which were widely separated geographically. The species selected for observation were atoms or ions which possessed a resonance line in the visible portion of the spectrum. When such species are present in sufficient numbers in the upper atmosphere, they scatter sufficient sunlight at their characteristic wavelength to be measured photometrically from ground observing stations during twilight periods. Six installations were instrumented with single-barrel photometers (Figure 1.1) which employed a rotating filter turret equipped with interference filters. These filters isolated each wavelength to be observed, and a birefringent filter was employed to provide maximum discrimination between sky background and the monochromatic signal. One site employed a simple photometer in which three interference filters were rotated in front of the objective lens. One filter was centered on the emission line to be observed, and the other two had passbands on each side of the emission

lines. Some twilight data was obtained from three other sites utilizing four-barrel photometers discussed in the next paragraph. In general, however, these units were unsatisfactory during the brighter portions of twilight.

A secondary objective included the measurement of early time debris history by observation with relative fast response, four-barrel photometers (Figure 1.2) employing a separate interference filter for each barrel. Three such units were placed at sites close to the detonation location. Early time debris arrival at conjugate areas was studied with birefringent units located near these areas. The detonation times precluded extensive measurements of early time debris by resonance scattering, since only minor amounts of debris moved beyond the earth's shadow. Measurements of that debris which did become sunlit were made, and other early time measurements which may be related to thermal, photochemical, or electron excitation of debris species were also made. It should be noted, however, that these measurements were far short of those obtainable for a detonation time selected specifically to take advantage of this technique (i.e., detonation just prior to twilight).

The data collected represents direct observations of the long-term geographical distribution of selected debris species

for the high-altitude events. It should be possible to determine the proper processes (i.e., diffusion, magnetic guiding, wind transport, or turbulence) which act to distribute this debris and their relative importance. With proper scaling factors to account for relative abundance, degree of ionization, and atomic weight, the distribution of other debris species may be computed. This information should correlate with, and assist in the interpretation of, data relating to such phenomena as RF blackout and trapping of ionized particles by the earth's magnetic field.

1.2 BACKGROUND

The dispersion of nuclear debris deposited in the upper atmosphere as a result of a high-altitude detonation depends markedly upon the height at which such material is released as well as several other physical parameters. Above about ninety kilometers, chemical reactions are relatively slow, so that any artificially injected material may be expected to preserve its optically active properties (that is, remain in the original atomic state) over extended periods of time. In this uncombined form it is possible to trace the material as it is transported by wind and the applicable diffusion mechanism (turbulent or molecular processes, according to its resident altitude).

The techniques employed in atmospheric airglow analysis to study twilight phenomena are well known, and several have direct application to the problem of interest here. By such methods the distribution with height of a suitable trace element in the upper atmosphere may be determined with high sensitivity (References 1 and 2). Recently, the authors of References 3 and 4 have successfully performed a series of experiments in which relatively small amounts of an artificially injected contaminant were released into the atmosphere in the form of a filament at altitudes of about eighty to two hundred kilometers. These were detected and subsequently traced with appropriate ground-based optical equipment (Reference 5). The techniques employed for these tests have been an outgrowth of such experiments and of such observations (References 6 and 7).

Below ninety kilometers, previous experimental attempts to track atomic trace materials by the resonance scattering technique described above have been unsuccessful. As shown by the authors of Reference 8, for the alkali family metals released at these altitudes, on the order of one-half the atomic material has chemically recombined in fractions of a second. The product molecules possess different optical properties and do not scatter light at the resonance wave-

lengths of the original atomic or ionized species.

The Star Fish event afforded the opportunity to observe nuclear debris at high altitudes over extremely large geographical areas. The detection and tracking by optical resonance scattering techniques is described in greater detail in subsequent sections of this report.

1.3 THEORY

In order to discuss the theory underlying the experiment, it is most convenient to subdivide the area into a part concerned with signal levels expected and one concerned with the backgrounds expected.

1.3.1 Signal Intensity and Signal-to-Noise Considerations.

Resonance scattering involves the ground state of the atom or ion, and for practical reasons is almost always limited to the first permitted level. Since only very thin clouds are considered, such processes as collisional de-activation may be neglected. Each atom or ion which absorbs a photon from the solar radiation upon it will subsequently emit isotropically a photon of the same wavelength. A coordinate system fixed in the particle is assumed so that Doppler shifts need not be considered for the present. It is convenient for the purpose at hand to obtain an optical absorption coefficient for each

resonance transition of interest. This is a useful parameter and will be defined such that the product of this coefficient and the solar flux will yield the energy scattered at the resonance wavelength per unit time per particle. The units and definitions used by various authors (References 9, 10, 11, and 12) and workers in the field of radiation are rather confused. Hence, the units and expressions to be used here will be defined in some detail.

Energy levels one and two are designated for the ground level and first permitted level, respectively, of the atom or ion. The frequency corresponding to this energy difference is ν and the wavelength λ . The probability that an atom (or ion) will absorb a photon from the incident radiation is

$$B_{1-2} \rho(\nu) \quad (1.1)$$

where B_{1-2} is the Einstein coefficient for absorption and $\rho(\nu)$ is the density of radiation at frequency ν . The energy (Reference 9) of radiation between ν and $\nu + d\nu$ per unit volume is $\rho(\nu) d\nu$. The term B_{1-2} is related to the Einstein coefficient for spontaneous emission A_{2-1} (transition probability) by the relation

$$B_{1-2} = \frac{c^3}{8\pi h \nu^3} \frac{S_1}{S_2} A_{2-1} \text{ cgs} \quad (1.2)$$

where S_1 and S_2 are the statistical weights of levels one and two. For an atomic energy level, $S = 2J + 1$, and for a term as a whole, $G = (2S + 1)(2L + 1)$ where J , S , and L have the conventional spectroscopic meaning. Then, where P is the probability of an absorption per atom (average number of photons absorbed per second per atom from solar radiation),

$$P = \frac{c^3}{8\pi h \nu^3} \frac{S_1}{S_2} A_{2-1} \rho_e(\nu) \text{ cgs} \quad (1.3)$$

The quantity $\rho_e(\nu)$ is in units of erg/cm³-unit frequency interval. $\rho_e(\nu) = \rho_p(\nu) \times h\nu$, where units of ρ_p are photons/cm³-unit frequency interval. The energy density resulting from a unidirectional flux of light is $\rho = \frac{\Phi}{c}$, where c is velocity of light, and Φ has units of photons/cm²-sec-unit frequency interval if ρ has units of ρ_p above. Since $\nu = \frac{c}{\lambda}$; $d\nu = -\frac{c}{\lambda^2} d\lambda$, then

$$\rho_e(\nu) = \frac{h\nu}{c} \lambda^2 \Phi$$

where Φ has units of photons/cm² of wavelength interval. Then

$$P = \frac{S_2}{S_1} \frac{A_{2-1} \lambda^4}{8\pi c} \Phi \quad (1.4)$$

where φ has the units above. The quantity

$$\frac{S_2}{S_1} \frac{A_{2-1}}{8\pi c} \lambda^4 \quad (1.5)$$

is defined as the absorption coefficient for the transition in question and is designated as σ . If the absorption cross section of the atom is plotted on a wavelength scale, then σ is equal to the integral underneath the curve for absorption in units of $\text{cm}^2 \times \text{angstroms} (\text{\AA})$.

Values of the solar flux above the earth's atmosphere are listed in Table 1.1. Table 1.2 lists some transition probabilities and computed absorption coefficients as well as the probability for scattering, P. Values of P are determined from the solar flux obtained from Table 1.1 and hence are valid only for clouds near the earth. Probability for scattering and absorption are identical, since secondary processes are ignored.

On the basis of the numerical values of Tables 1.1 and 1.2, the following wavelengths have been chosen for observation:

neutral Ba (5,535 \AA), neutral Zr (6,130 \AA),
and ionized Ba⁺ (4,554 \AA). The four lines chosen have wavelengths in the visible and have reasonably high signal strengths.

Only debris clouds which are optically thin need be considered. For this case each atom or ion may be considered as bathed in sunlight independently of other like atoms in the cloud. It is easy to show that the debris cloud will become optically thin within a second or less. At room temperature (300°K), the optical cross section, δ , per atom is about 10^{-11}cm^2 for resonance absorption. This cross section is given by σ defined above divided by the Doppler line width. At room temperature this width is of the order of $2 \times 10^{-2}\text{ \AA}$ and increases as the square root of temperature. The optical cross section multiplied by the number of atoms/ cm^2 column (σ) is a measure of the optical thickness. If I_0 is the light flux at the resonance wavelength and I the amount transmitted through the cloud,

$$I = I_0 \exp (-S\sigma)$$

If $S\sigma = 1$, the column is said to be one optical thickness. If $S\sigma$ is small, then only a small fraction of the incident light is absorbed, and the cloud is said to be optically thin. Consider 10^{26} total atoms of one kind in a cloud expanding at 10^8 cm/sec , then in one second σ is of the order of 2×10^9 atoms/ cm^2 . It is difficult to define a meaningful temperature for a cloud after velocities are frozen in, but

effective optical cross sections are certainly less than the 10^{-11} cm^2 by perhaps a factor of 1,000. Hence, for all practical purposes the sunlight incident upon each atom in the cloud has not been diminished by the presence of like atoms in the cloud. By the same argument, subsequent absorption of light once scattered is completely negligible and need be considered no further.

The light flux falling upon a detector is a function of the various optical components used in the detecting instrument. If the cloud is small compared to the acceptance angle of the photometer used for detection, the light flux received from the cloud and incident upon the detector is given by

$$\theta_s = \frac{N A T P}{4\pi R^2} \quad (1.6)$$

Where: θ_s is the signal flux upon the detector in units of photons/sec

N is the total number of atoms in the cloud of a single species

A is the photometer aperture area

T is the transmission of the instrument and the intervening atmosphere, if any

P is the scattering probability defined in Equation

1.4

R is the cloud to photometer distance

In Equation 1.6 a filter which isolates the resonance wavelength of a single species in the cloud and which is broad enough to pass the entire Doppler shifted line is assumed.

For a cloud which more than fills the photometer acceptance angle, the signal flux received is given by

$$\theta_s = \frac{\sigma P A T \Omega}{4\pi} \quad (1.7)$$

where σ is the number of atoms/cm² column, and Ω is the photometer acceptance angle in steradians. It is assumed in Equation 1.7 that the value of σ over the photometer field Ω is constant. If σ is not reasonably constant, then a mean value must be used or individual contributions summed or integrated over the field angle. For most cases that will be encountered in practice, either Equation 1.6 or 1.7 provides sufficient precision for the initial estimates required for instrument design.

In addition to signal light, a significant contribution to the received light flux is due to background. The background may be sunlight scattered by the earth's atmosphere as encountered during daytime and during twilights, or it may be

starlight, airglow, or galactic light during night hours. Values of sky backgrounds have been tabulated and plotted for various twilight and night conditions in a later section.

At the detector, light from the cloud and background light produce an electrical effect which is a simple superposition of the two quantities. Some method of discrimination is required to separate the two effects, and the lower limit of detectability is frequently determined by the ability to discriminate. Discrimination techniques will be discussed in a following section. It is sufficient now to state that by proper techniques the limit of detectability is set by the noise inherent in the detector output.

There is a noise component in the light flux falling upon the detector. This is due to the fact that the light is made up of discrete photons which arrive at the detector at an average rate but with random or statistical variations. The effect of these statistical fluctuations is termed noise (Reference 13). At the cathode of a photo-emissive surface, photons are absorbed and photo-electrons emitted. Since the number of electrons emitted is less than the number of incident photons (about one electron for five photons for the most optimum conditions), the noise at the point in the instrument is greater than in the incident light flux. In practice the

noise present at the photocathode of a good photomultiplier is the dominant source for the entire instrument, and all other sources of noise may be ignored by comparison to it.

For a purely random process, fluctuations from the average value occur which are predictable. If n electrons are emitted in the time interval τ , the average value is n/τ with an uncertainty of \sqrt{n} . With a photomultiplier, amplifier, and direct-current recording system, the recorder deflection measures the average number of electrons emitted (direct current), and the time interval τ is determined by the instrumental response time. τ is also given by $\tau = \frac{1}{2\pi\Delta f}$ where Δf is the electrical band-pass frequency.

Signal-to-noise ratio (S/N) is defined as

$$\frac{S}{N} = \frac{k \theta_s}{\sqrt{n_c}} \sqrt{\tau} \quad (1.8)$$

where k is the conversion factor relating the number of electrons emitted per incident photon, θ_s as before is the photon flux due to signal, and n_c is the total number of cathode electrons per unit time. The term n_c is a summation of various components

$$n_c = k \theta_s + k e_c + i_d$$

where θ_b is the light flux due to background flux, and i_d is the dark current. Dark current is a combination of thermally emitted electrons and some leakage current. It would be present if no light were incident upon the cathode. In any case of interest for the present work, i_d and $k \theta_s$ are very small compared to $k \theta_b$. Therefore

$$\frac{S}{N} = \frac{\theta_s}{\sqrt{\theta_b}} \sqrt{k \tau} \quad (1.9)$$

Unless strong stars or some other source such as the sun or the moon are directly in the photometer field, the photometer light flux due to background is given by

$$\theta_b = \frac{R_\lambda A T W \Omega \lambda}{hc} \quad (1.10)$$

where R_λ is the background intensity at wavelength λ taken from a subsequent section. R_λ has units of $\text{erg/cm}^2 \cdot \text{sec} \cdot \text{\AA} \cdot \text{steradian}$. A is the aperture area; T , the transmission of the instrument and of the atmosphere at wavelength λ ; W is the filter width in \AA ; Ω , the photometer field angle in steradians; and λ/hc , the number of photons per erg at wavelength λ .

Hence,

$$\frac{S}{N} = \frac{\sigma}{\sqrt{R_\lambda}} \times \frac{P}{4\pi} \sqrt{\frac{A T \Omega h c k \tau}{W}} \quad (1.11)$$

Equation 1.11 is written in the form above so that for any set of photometer characteristics and specific resonance line the right-hand portion is constant. The term σ depends upon the cloud and the time of observation, while R_λ depends upon time of day and also upon position in the sky at which the photometer is pointed.

1.3.2 Backgrounds. A study of the twilight sky has interested numerous investigators for many years. The early studies were confined to qualitative explanations of the readily observable phenomena; such as, intensity, spatial, and color changes and earth shadow heights. Later studies have primarily been directed toward quantitative investigations concerning (1) upper air densities, (2) dust layers in the higher atmosphere, and (3) airglow.

The first two of these objectives have met with limited success for two primary reasons. First, a satisfactory analytical expression for the brightness variation has not been found. The extinction over the long, oblique path has never been integrated in a closed form; and although the labor of numerical or graphical methods has been reduced by the use of

computers, the accuracy has increased only slightly, since results are strongly dependent on the distribution and variations of dust, ozone, and other small impurities which become important for the long optical paths.

Secondly, the intensity variations during the twilight are so great and so rapid that instrumentation to record the spectral and spatial variations is difficult. Present-day photomultiplier tubes and interference filters are a satisfactory solution to this problem. However, even though some measurements have been made rather recently, none are very complete, and comparison of results from different observers is difficult, since no uniform system has been used. The angle of view, spectral bandwidth, range of solar angles, spectral sensitivity of the receiver, wide variation in units, as well as geographic and time variation of the observations are some of the major difficulties of comparison. A large number of the observations were made only in the zenith with wide-band filters and reported only in relative units. Such measurements can indicate daily and seasonal variations but can give little reliable information concerning other sky positions without an accurate theory and mathematical analysis.

One of the more complete sets of spatial and spectral measurements was made by the author in Reference 14. However,

the spectral measurements were made only for solar depression angles less than 8 degrees, and absolute intensity measurements are not easily attained from the reported values. The authors in References 15 and 16 independently measured the zenith brightness in absolute units which in some cases differed by an order of magnitude. The authors in Reference 17 also made absolute measurements but only for an elevation angle of 20 degrees in the sun's azimuth. They also chose several models for dust and ozone from which to compute brightness values for comparison with the measurements. The reported values show the pronounced effect of the ozone as computed. Figure 1.3 shows both the measured and computed values. Since no complete set of measurements have been found, a composite of the measurements of several investigations must be used. Figure 1.4 shows computed values due only to molecular scattering for a solar elevation angle of 6 degrees.

The radiance from the night sky is composed of two major parts. One is a continuum due to starlight (direct and scattered), various galactic sources, and zodiacal light. Since these sources all have spatial variation, the integrated flux received at the earth varies with viewing direction. However,

if the angular field of view is large enough so that local variations such as bright nebulae, star clouds, and emission regions may be neglected, the variations are much reduced in magnitude. An average value of continuum is shown in Figure 1.5.

The other part of the night sky radiance is due to the airglow which consists of line and band emission from various constituents in the earth's upper atmosphere. The exact mechanisms which cause the emission are not satisfactorily understood, but many of the observable characteristics have been thoroughly investigated. Figure 1.5 shows the major features of the night airglow superimposed on the continuous spectrum of the night sky. Table 1.3 also shows an average intensity of these emissions and a probable range of intensity variations.

The radiation received from the airglow emission is also dependent on direction of viewing, the maximum occurring at a large zenith angle. This effect is the result of an increase due to a longer optical path through the emitting region and a decrease due to the increased extinction in the lower atmosphere. The exact magnitude and position of the maximum depends in a very insensitive manner on the height of the emitting region. For a height of 100 km, this effect causes a spatial variation of about two for emission in the visible

spectrum. This is small compared to daily, seasonal, and sporadic variation as shown by Table 1.3.

The attenuation of light by the earth's atmosphere is caused by:

1. Molecular scattering (Rayleigh scattering). The Rayleigh scattering coefficient is, in the first approximation, given by

$$\beta_M = \frac{32\pi^3(\mu - 1)^2}{3N\lambda^4} \quad (1.12)$$

where μ is the refractive index of air ($\mu \sim 1.0003$), N is the number density of air ($1/\text{cm}^3$), and λ is the wavelength of the light.

2. Large particle scattering (Mie scattering). The Mie scattering coefficient is given by $\beta_p = \pi r^2 NE$, where r is the radius of the particle, and E is the efficiency factor which is dependent on the refractive index of the particles, the radius of the particles, and the wavelength of the light. However, in the atmosphere where the primary scattering particles are large (i.e., $> 0.5 \mu$) and have a broad size distribution the scattering is almost independent of wavelength, and E is about two.

3. Absorption by atmospheric gas molecules. Absorption

within the visible is relatively unimportant, since less than 3 percent of the incoming radiation is absorbed along the total path within the atmosphere. The ultraviolet is completely absorbed by ozone below 2,900Å, and the infrared has many absorption bands due to molecular oxygen and water vapor.

The total effect of atmospheric attenuation on incoming radiation may be expressed as,

$$I = I_0 \exp - (\beta_M l_1 + \beta_p l_2 + \beta_o l_3) \quad (1.13)$$

where I is the intensity reaching the ground, I_0 is the intensity outside the atmosphere, β_o is the total absorption coefficient, and l_1 , l_2 , and l_3 are the corresponding path lengths reduced to a standard temperature and pressure.

For this report, values of β_M were those given by the standard atmosphere. The path length l_1 was taken as the distance from the sun to the earth's surface. Altitude variations of β_M were neglected and are related by

$$\beta_M(h) = \beta_{M_0} \exp(-h/H_M) \quad (1.14)$$

where h is the altitude, and H_M is considered a constant for all altitudes, namely, the scale height, and has the value of 8.2 km. Temperature variations of β_M were ignored, and values

computed at 0°C and pressure of 1,013 mb were used.

The values of β_p were deduced from actual extinction measurements of the authors in Reference 19. The attenuation coefficient over the visible region was found to be $\beta_{T_v} + \beta_{P_v} = 0.180 \text{ km}^{-1}$ for a standard clear atmosphere at sea level. The single Rayleigh scattering coefficient, β_{M_v} , has to be based on the luminosity function, ψ_λ , of the light-adapted eye of a standard observer. Then

$$\beta_{M_v} = \frac{\int_0^\infty I_\lambda \psi_\lambda \beta_{M_\lambda} d\lambda}{\int_0^\infty I_\lambda \psi_\lambda d\lambda} \quad (1.15)$$

where I_λ is the intensity of the solar radiation outside the atmosphere. β_{M_v} has been evaluated by many investigators who agree that the value is 0.0126 km^{-1} at normal temperature pressure. The value of β_{P_0} then is 0.1647 km^{-1} . Measurements up to 38,000 feet showed that height variation of β_p could be expressed as

$$\beta_p(h) = \beta_p(0) \exp(-h/H_p) \quad (1.16)$$

where $H_p = 1.12$ km. Extinction due to absorption by atmospheric gases was considered to be contributed only by ozone. All radiation below $2,900\text{\AA}$ was completely absorbed, and a slight correction was added to the blue region and to the region around $6,000\text{\AA}$ for large zenith angles.

1.3.3 Effects of Atmospheric Attenuation. During twilight intervals, some of the sunlight falling upon the debris to be measured is attenuated by the earth's atmosphere. Figure 1.6 describes this situation graphically. If $I(\delta)$ is the total light flux incident upon the detector at solar depression angle δ when the instrument is pointed at the zenith, then

$$I(\delta) = k \int_0^{\infty} \epsilon(\delta, h) \rho(h) dh \quad (1.17)$$

k includes constants such as the instrumental field of view, angle of acceptance, transmission of instrument, transmission of the atmosphere between the cloud and instrument, and the rate at which each debris atom scatters light when illuminated by unattenuated sunlight. $\epsilon(\delta, h)$ is the transmission factor to be applied to raw sunlight to determine the sunlight striking debris at height h and at solar depression angle δ . $\rho(h)$

is the number of debris scattering material per unit volume at height h , and dh is an elemental height interval.

If a height, h_0 , is defined such that

$$\cos \delta = \frac{a}{a + h_0}$$

$$h_0 \text{ (km)} \approx 0.97 \delta^2 \text{ (degree)}^2$$

for $\delta < 20$ degrees

where a is the radius of the earth in km; then ϵ may be considered as a function of h_0 and h . The value of ϵ varies from zero a few kilometers below h_0 to unity at heights of the order of $h_0 + 40$ km. For depression angles less than about twenty degrees, ϵ may be considered as a function of a single variable h' if $h' = h_r - h_0$ to a very good approximation. Figures 1.7 and 1.8 show curves of $\epsilon(h)$ at depression angles of 8 and 14 degrees for a particular atmosphere to illustrate this point.

It might be thought that the local weather conditions would markedly influence the nature of ϵ . This is true only for the values of ϵ near h_0 . Values at heights of 3 to 5 km above h_0 are not affected by local weather since solar rays striking such heights pass through the earth's atmosphere

well above local weather. The variable effects of weather near the earth's surface do not appreciably affect Equation 1.17, since ϵ near h_0 is extremely small in all cases. Figure 1.7 shows ϵ versus h' for three sets of weather conditions—average clear day, perfectly clear day, and large storm in the path of the solar rays.

1.3.4 Determination of the Relative Intensity of Photon Flux Caused by Nuclear Debris—Resonance Scattering. This is discussed in Appendix C.

TABLE 1.1 SOLAR PHOTON FLUX OUTSIDE THE ATMOSPHERE

$\psi_A = \text{photons/cm}^2 \cdot \text{sec} \cdot \text{\AA}$

Range: 2200\AA-6000\AA, $\Delta\lambda = 50\text{\AA}$; 6000\AA-11000\AA, $\Delta\lambda = 100\text{\AA}$;
11000\AA-20000\AA, $\Delta\lambda = 1000\text{\AA}$.

Range (\AA)	ψ_A photons $\text{cm}^2 \cdot \text{sec} \cdot \text{\AA}$	Range (\AA)	ψ_A photons $\text{cm}^2 \cdot \text{sec} \cdot \text{\AA}$	Range (\AA)	ψ_A
2200-2250	3.14×10^{11}	3400-3450	2.00×10^{13}	4600-4650	5.04×10^{13}
2250-2300	5.98	3450-3500	2.04	4650-4700	5.16
2300-2350	6.32	3500-3550	2.10	4700-4750	5.12
2350-2400	6.74	3550-3600	2.12	4750-4800	5.22
2400-2450	7.10	3600-3650	2.24	4800-4850	5.12
2450-2500	7.52	3650-3700	2.36	4850-4900	4.96
2500-2550	9.66	3700-3750	2.48	4900-4950	5.08
2550-2600	1.38×10^{12}	3750-3800	2.36	4950-5000	5.18
2600-2650	2.52	3800-3850	2.32	5000-5050	4.98
2650-2700	3.24	3850-3900	2.20	5050-5100	5.02
2700-2750	3.14	3900-3950	2.26	5100-5150	4.98
2750-2800	3.06	3950-4000	2.82	5150-5200	5.02
2800-2850	4.44	4000-4050	3.54	5200-5250	5.10
2850-2900	7.02	4050-4100	3.90	5250-5300	5.20
2900-2950	9.08	4100-4150	4.00	5300-5350	5.30
2950-3000	9.12	4150-4200	4.08	5350-5400	5.38
3000-3050	1.09×10^{13}	4200-4250	4.04	5400-5450	5.42
3050-3100	1.16×10^{13}	4250-4300	3.80×10^{13}	5450-5500	5.40×10^{13}
3100-3150	1.23	4300-4350	3.80	5500-5550	5.42
3150-3200	1.30	4350-4400	4.16	5550-5600	5.40
3200-3250	1.50	4400-4450	4.64	5600-5650	5.40
3250-3300	1.82	4450-4500	4.84	5650-5700	5.44
3300-3350	1.84	4500-4550	4.98	5700-5750	5.54
3350-3400	1.92	4550-4600	5.04	5750-5800	5.58
5800-5850	5.60	7700-7800	4.88	9900-10000	3.79
5850-5900	5.66	7800-7900	4.92	10000-10100	3.71
5900-5950	5.68	7900-8000	4.86	10100-10200	3.67
5950-6000	5.66	8000-8100	4.84	10200-10300	3.64
		8100-8200	4.78	10300-10400	3.58
6000-6100	5.48	8200-8300	4.79	10400-10500	3.54
6100-6200	5.47	8300-8400	4.84	10500-10600	3.49
6200-6300	5.44	8400-8500	5.57	10600-10700	3.46
6300-6400	5.42	8500-8600	4.52	10700-10800	3.40
6400-6500	5.41	8600-8700	4.45	10800-10900	3.38
6500-6600	5.44	8700-8800	4.47	10900-11000	3.31
6600-6700	5.47	8800-8900	4.43		
6700-6800	5.39	8900-9000	4.36	11000-12000	3.07
6800-6900	5.33×10^{13}	9000-9100	4.23×10^{13}	12000-13000	2.66×10^{13}
6900-7000	5.28	9100-9200	4.21	13000-14000	2.32
7000-7100	5.34	9200-9300	4.20	14000-15000	2.02
7100-7200	5.20	9300-9400	4.14	15000-16000	1.78
7200-7300	5.20	9400-9500	4.07	16000-17000	1.56
7300-7400	5.17	9500-9600	3.97	17000-18000	1.38
7400-7500	5.19	9600-9700	3.97	18000-19000	1.22
7500-7600	5.19	9700-9800	3.99	19000-20000	1.08
7600-7700	5.02	9800-9900	3.79		

TABLE 1.2 TRANSITION PROBABILITIES

Element	$\lambda(\text{\AA})$	$J_2 - J_1$	g_2/g_1	$\sigma, \text{cm}^2/\text{\AA}$	P photons atom sec	N (atoms/kg)
Rb I	7947.60	1/2-1/2	1	1.89×10^{-21}	9.1	7.1×10^{24}
	7800.227	1 1/2-1/2	2	3.65×10^{-21}	17.8	
Sr I	4607.331	1-0	3	3.52×10^{-23}	0.18	6.85×10^{24}
Sr II	4077.714	1 1/2-1/2	2	1.1×10^{-22}	0.39	
Zr I	6121.49	4-4	1	1.03×10^{-21}	5.6	6.6×10^{24}
	6136.58	2-2	1	9.9×10^{-22}	5.4	
Zr II	3391.96	3 1/2-4 1/2	6/5	3.8×10^{-22}	0.75	
Nb I	4058.933	3 1/2-4 1/2	6/5	1.8×10^{-21}	7.0	1.48×10^{25}
Mo I	3798.259	4-3	9/7	4.37×10^{-22}	1.03	6.25×10^{24}
	3864.115	3-3	1	3.45×10^{-22}	0.76	
	3902.968	2-3	5/7	2.5×10^{-23}	0.06	
Te I	4298.2	3 1/2-2 1/2	7/6	8.6×10^{-22}	3.25	1.4×10^{25}
	4263.4	2 1/2-2 1/2	1	7.22×10^{-22}	2.75	
Tc I	4239.4	1 1/2-2 1/2	2/3	4.80×10^{-22}	1.92	
Ru I	3799.1	5-4	11/9	4.2×10^{-22}	0.99	5.9×10^{24}
		4-3				
Rh I	3692.357	3 1/2-4 1/2	4/3	2.36×10^{-22}	0.51	5.95×10^{24}
	3657.987	2 1/2-3 1/2	3/4	1.93×10^{-21}	4.55	
Ag I	3280.682	1 1/2-1/2	2	5.1×10^{-22}	0.93	5.6×10^{24}
	3382.890	1/2-1/2	1	2.37×10^{-22}	0.43	
Cd I	2288.7	1-0	3	7.35×10^{-22}	.044	5.4×10^{24}
In I	4511.310	1/2-1 1/2	1/2	1.08×10^{-22}	.54	5.24×10^{24}
	4101.764	1/2-1/2	1	1.24×10^{-22}	.50	
Sn I	3175.046	1-2	3/5	8.75×10^{-24}	.010	5.08×10^{24}
	3036.120	0-1	1/3	1.1×10^{-23}	.012	
	3009.136	1-1	1	8.0×10^{-24}	.009	
Co I	8521.10	1 1/2-1/2	2	4.58×10^{-21}	15.1	4.9×10^{24}
	8943.50	1/2-1/2	1	2.40×10^{-21}	4.82	
Ba I	5535.484	1-0	3	5.12×10^{-21}	27.7	4.4×10^{24}
Ba II	4354.033	1 1/2-1/2	2	1.45×10^{-21}	7.3	
	4934.086	1/2-1/2	1	8×10^{-22}	4.03	
La I	7270.11	2 1/2-2 1/2	1	1.87×10^{-21}	9.7	4.34×10^{24}
Li I	6707.74	1 1/2-1/2	2	2.95×10^{-21}	15.9	8.65×10^{25}
	6707.89	1/2-1/2	1			
	8126.52	1/2-1 1/2	1/2	1.05×10^{-21}	5.0	
		1/2-1/2	1			
Ne I	5896.92	1/2-1/2	1			
	5889.95	1 1/2-1/2	2	2.56×10^{-21}	0.72	2.63×10^{25}
	3302.94	1/2-1/2	1			
K I	3303.34	1 1/2-1/2	2	6.74×10^{-24}	.0006	
	7664.907	1 1/2-1/2	2	3.45×10^{-21}	17.3	1.54×10^{25}
	7698.979	1/2-1/2	1	1.88×10^{-21}	8.95	
	4044.143	1 1/2-1/2	2			
	4047.214	1/2-1/2	1	1.05×10^{-23}	.036	
Ca I	4227	1-0	3	2.58×10^{-21}	.52	1.52×10^{25}
Ca II	3934	1 1/2-1/2	2	9.6×10^{-22}	.108	
	3968	1/2-1/2	1	4.65×10^{-22}	.065	
Al I	3962	1/2-1 1/2	1/2	1.82×10^{-22}	.51	2.23×10^{25}
Fe I	3860	4-4	1	1.08×10^{-23}	.024	1.04×10^{25}
	3720	5-4	11/9	1.53×10^{-23}	.037	
Fe II	4233	3 1/2-2 1/2	4/3	1.10×10^{-22}	.44	

TABLE 1.3 ABSOLUTE INTENSITIES OF THE BASIC NIGHT SKY EMISSIONS

Index	λ	I_{av}		I_{av} (ergs/cm ² sec ster)	Deviation $\frac{\Delta I}{I}$ %	I_{from} (8)	I_{max} (Rayleighs)	I_{min}	No. of measure- ments	
		(Rayleighs)								
OI	5577 A	560		15.9×10^{-5}	220	39	250	1100	174	14
Na	5890	203		5.5	90	44	240	427	51	20
	5896									
OI	6300	590		14.8	270	15	150	1100	184	20
	6364									
H	6562	17		0.41	5	29	---	27	12	14
(8, 2)	5890	19		0.51	34	37	60	163	61	20
(5, 0)	6170	48		1.23	15	31	10	81	16	11
(9, 3)	6257	138		3.48	35	25	170	308	94	20
(6, 1)	6500	96		2.33	25	26	60	320	62	20
(6, 2)	8347	980		18.6	300	30	820	3000	660	9
(7, 3)	8833	1750		31.3	400	23	1940	5470	1120	9

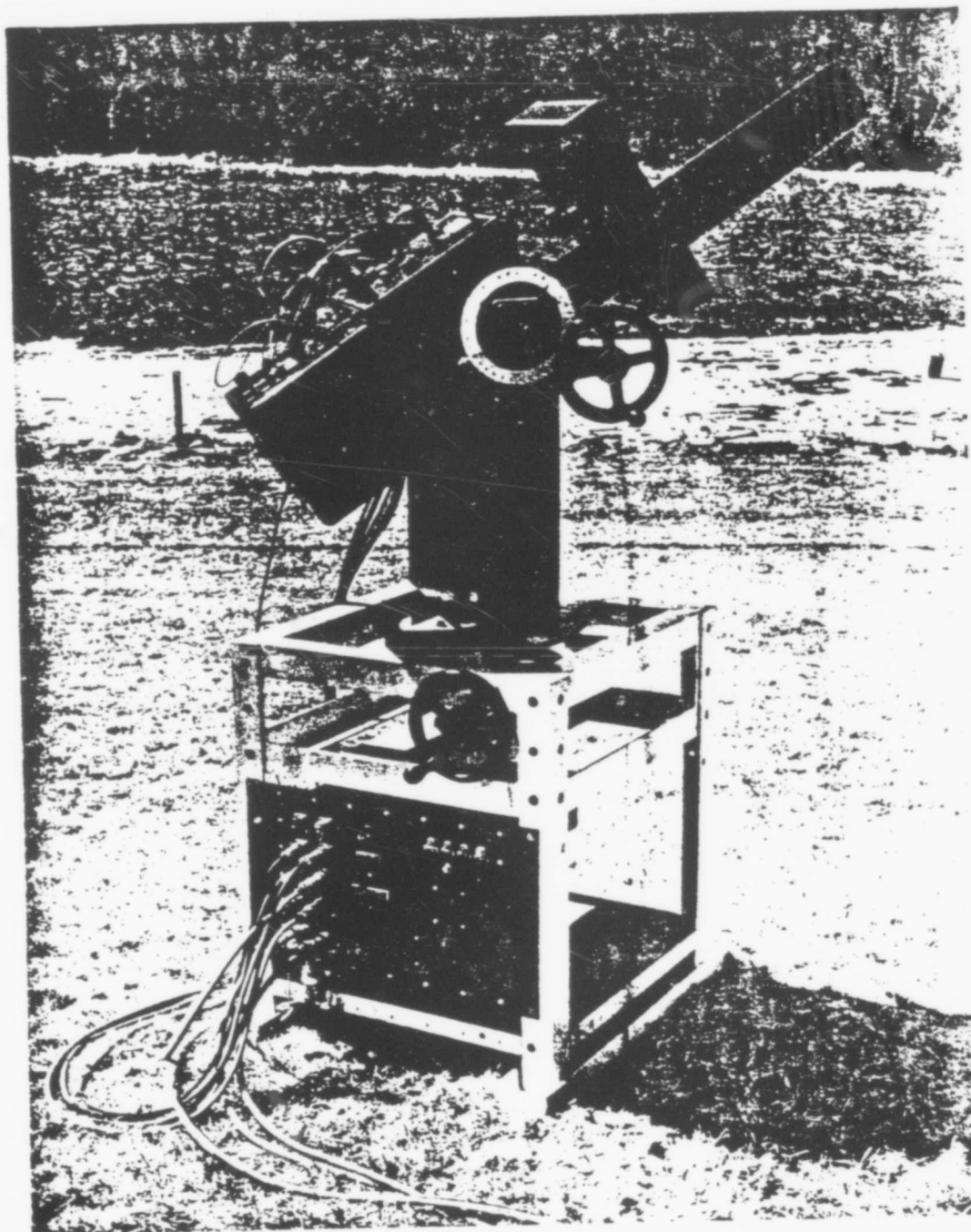


Figure 1.1 Birefringent photometer. (GCA photo)

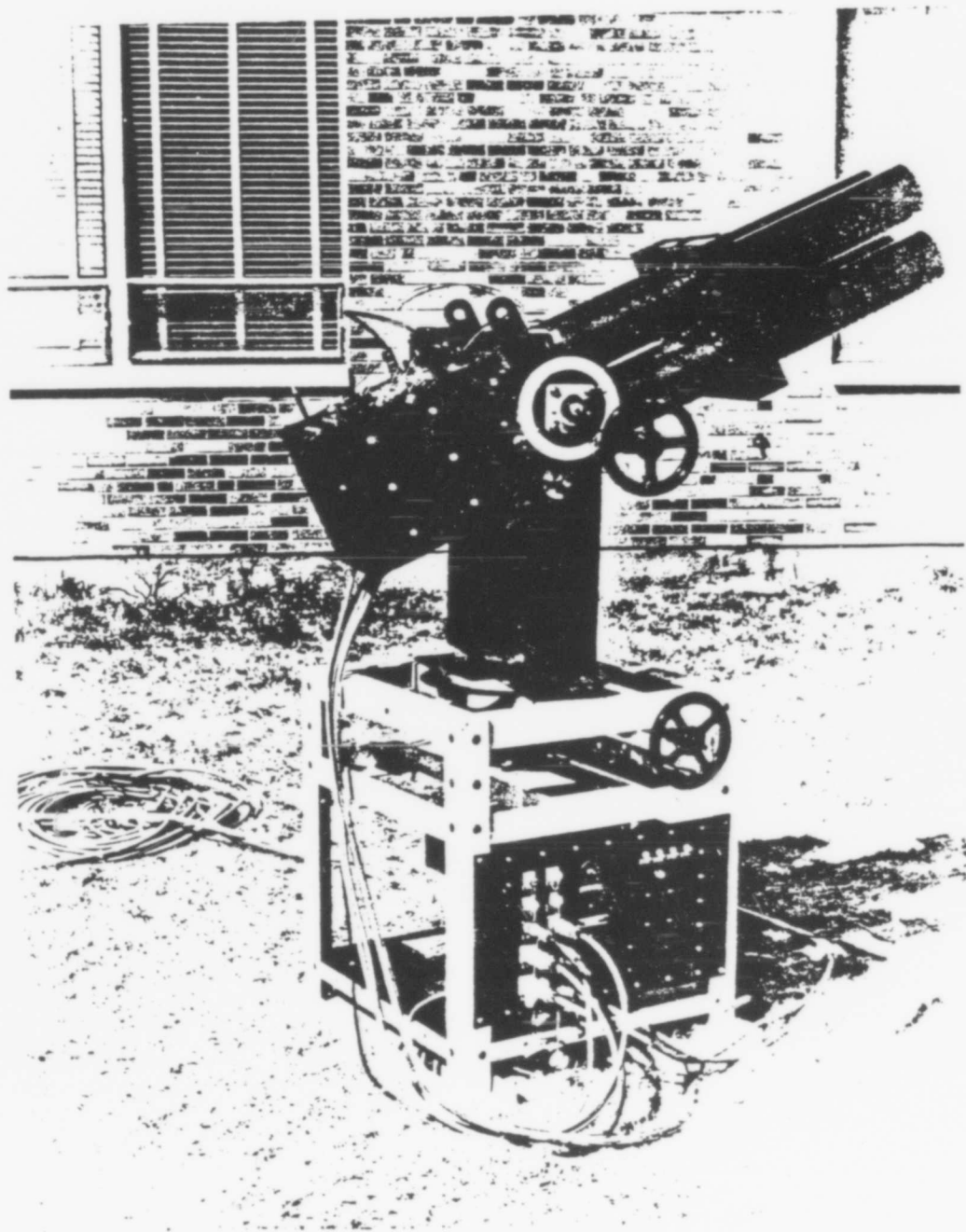


Figure 1.2 Four-barrel interference photometer. (GCA photo)

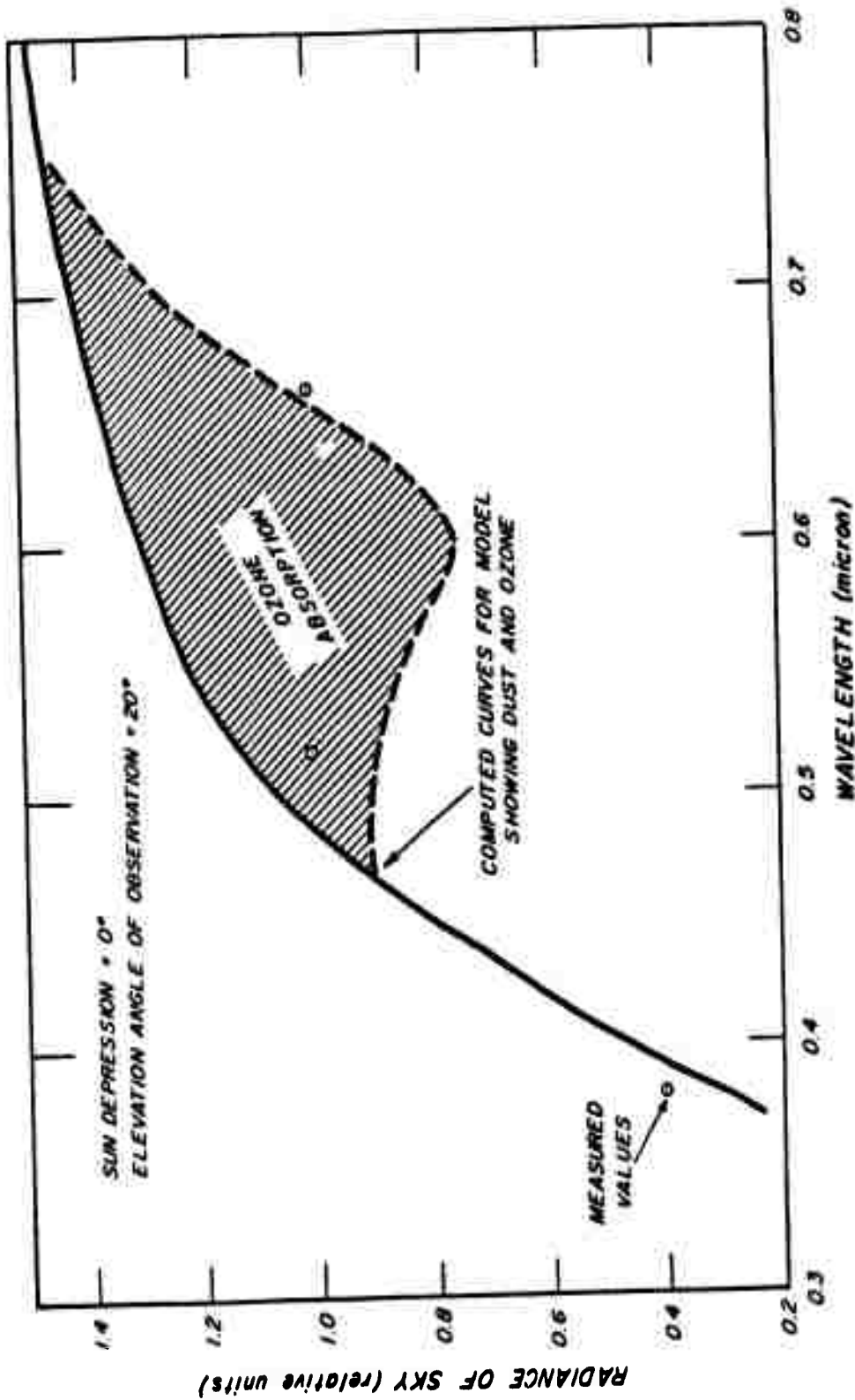


Figure 1.3 Computed and measured values of the radiance of the sky at sunset (Reference 17).

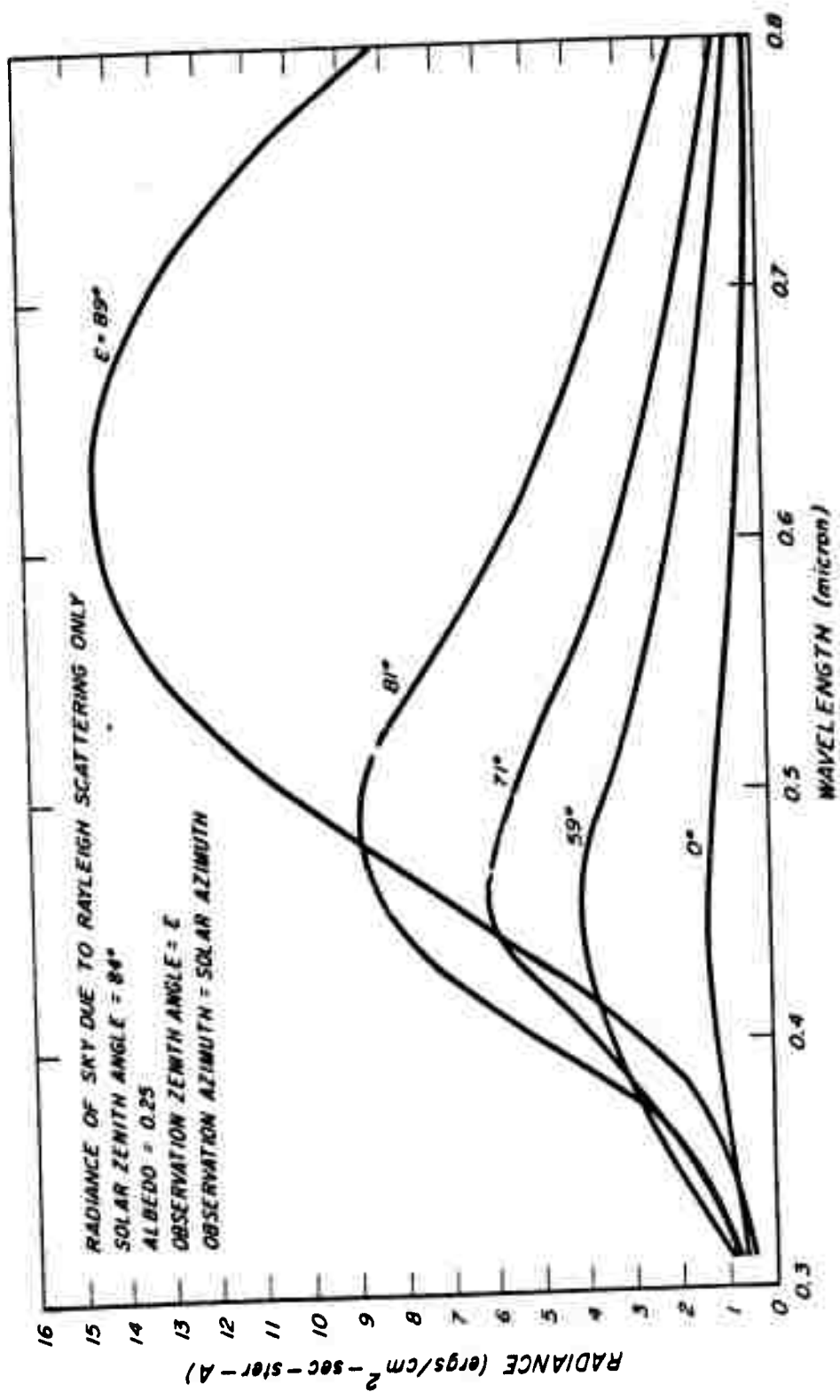


Figure 1.4 Computed values of the radiance of the sky due to molecular scattering only.

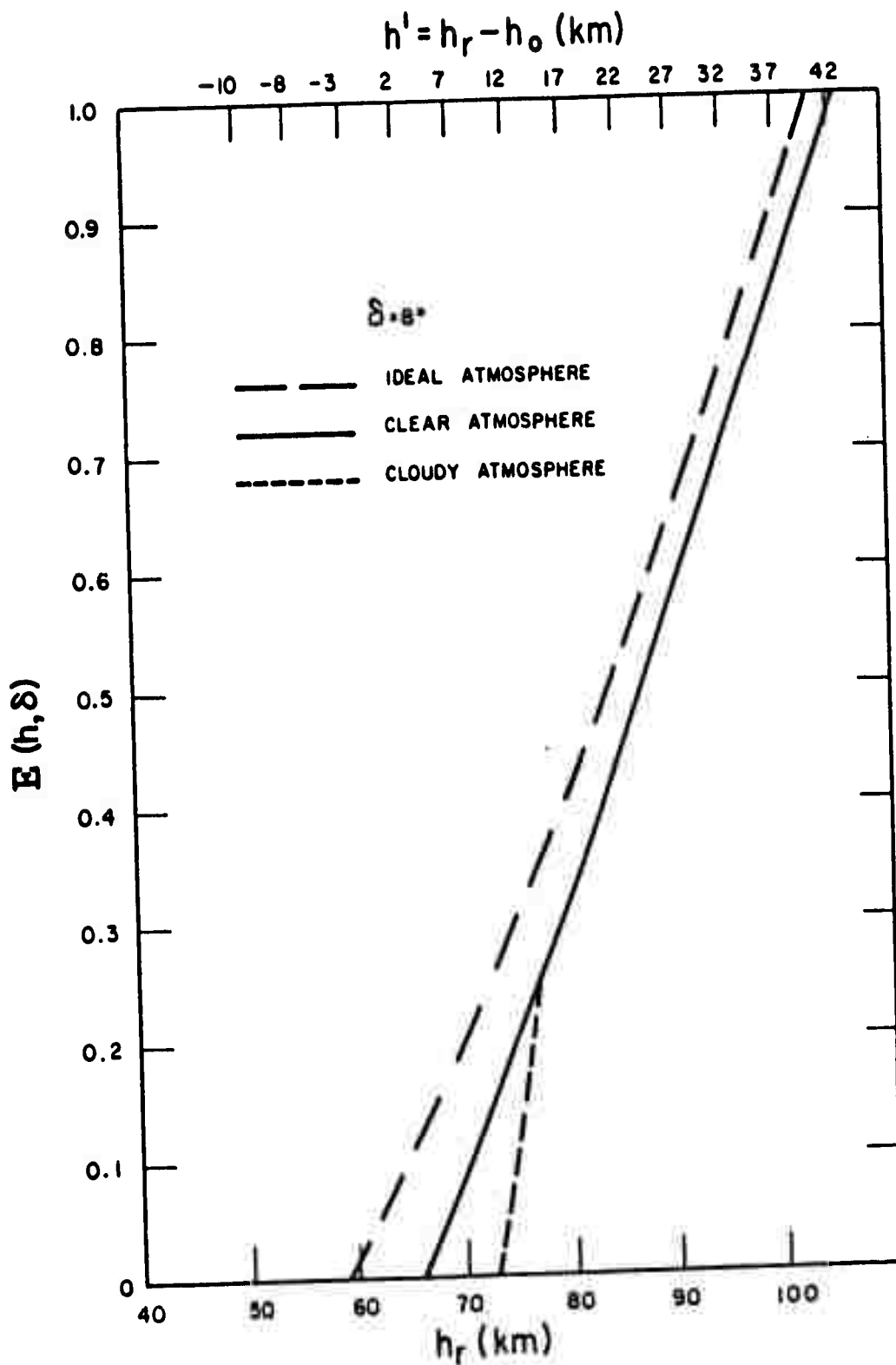


Figure 1.7 Atmospheric transmission coefficient versus height, for 8° depression angle.

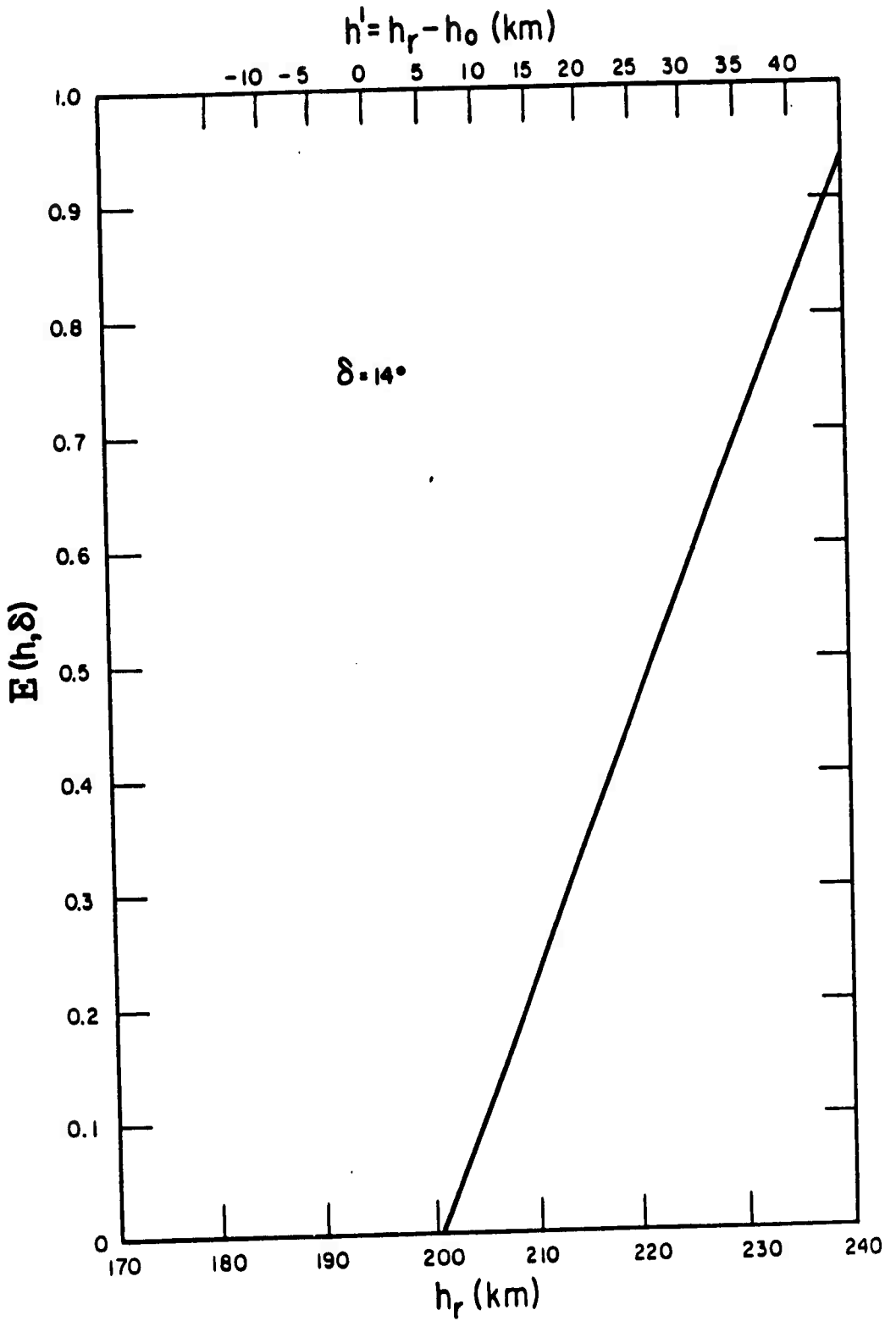


Figure 1.8 Atmospheric transmission coefficient versus height, for 14° depression angle.

CHAPTER 2

PROCEDURE

2.1 OPERATIONS

Observations were made during and following all events including some of the air drops. Only the high-altitude events—Star Fish, King Fish, and to a very limited extent Blue Gill and Check Mate—yielded meaningful data. Twilight backgrounds were observed at all sites except during periods of rain, when sites were unmanned, and when ships were at Pearl Harbor.

All sites were manned and operating at event time. In all cases of interest, events occurred under night conditions with very little opportunity to view material expanding into sunlit areas during early times (seconds to minutes after event). Sites within view of the burst (Johnston Island, S-1, S-2, and S-4) had their photometers covered at event time and opened them as soon as possible. This varied from a few seconds to minutes. The self-luminous area of the sky was scanned along a magnetic meridian and in a plane passing through the visible center of luminosity and perpendicular to the magnetic meridian. The light thus recorded may have been due to thermal excitation, collision processes, fluorescence,

electrons, or ionic recombination of the species having a resonance line at the filter passband. The recorded light may also have been due to leakage through filter skirts or filter transmission at the passband of complicated transitions of higher levels or continuous emissions. These recordings, filter passbands, and instrument sensitivities are available for reduction. In general, however, the light sources were of such a complicated nature that little specific information can be deduced; and detailed reduction has not been performed.

Stations along the magnetic meridian (French Frigate Shoals, Tutuila, and Tongatapu) were uncovered and operating at event time. Their initial pointing was at the conjugate region, or more specifically a region where the magnetic field line through the burst point intersected the 130-km height, or as nearly as possible to this point depending upon local clouds.

Stations to the west (Midway and Wake) were instructed for Star Fish to point along a great circle through Johnston Island and, clouds permitting, at a zenith angle less than 40 degrees which would be optimum for observing material which might reach sunlit regions. For the other events they were to be guided by visual observations and point to regions

which might become illuminated.

Major resonance scattering data was expected during twilight intervals following the events. During these periods all stations operated continuously between solar depression angles of 4 degrees to 18 or more degrees. Sufficient readings were taken at the zenith position to provide a continuous curve with solar depression angle (each two minutes or so). In addition the sky was scanned between zenith readings to determine if the distribution of debris over the station was uniform. When clouds were present, the observer tried to point to clear patches as near the zenith as possible, keeping a careful record of time and pointing angles on the recorder chart.

The four-barrel instruments were not well suited for twilight observations and ceased to yield meaningful data after about the third twilight following each high-altitude event.

2.2 INSTRUMENTATION

2.2.1 Filters. The basic principles involved in the detection of a line emission with a continuous sky background have been discussed previously. In general, the detection limit is determined by the statistical noise in the background signal. For specific cases, other considerations,

such as cloud dynamics and Doppler shift, are important and have been considered. Practical application of these principles also requires consideration of the availability and proper use of optical components and detection. Characteristics of optical filters and radiation detectors which are required and available for this application will now be discussed followed by a somewhat detailed description of the two photometric systems.

Interference filters, as the name implies, utilize the phenomenon of optical interference of multi-reflected light to pass selected wavelengths. Basically, a filter consists of two highly reflecting but partially transmitting surfaces separated by a spacer layer of non-absorbing material. When the optical separation of the reflecting surface is a half wavelength or an even multiple of a half wavelength, the multi-reflected beams emerge in phase, and the filter has high transmission. Other wavelengths suffer destructive interference during the multiple passages in the layer and are reflected. The principle is so similar to that of a Fabrey-Perot interferometer that the early type filters were called Fabrey-Perot interference filters.

The simplest type of interference filter utilizes thin evaporated films of silver separated by a layer of magnesium

fluoride (MgF_2) which has a refractive index of 1.38 or cryolite (sodium aluminum fluoride, $3\text{NaF} \cdot \text{AlF}_3$) which has a refractive index of 1.35. These substances have high optical transmission over a wide range of wavelengths and may be successfully evaporated into thin film of controlled thickness. A more efficient filter is obtained if the silver surfaces are replaced by alternate layers of transparent materials of high and low index of refraction. This system utilizes the optical interference at the boundaries of the different materials to obtain a high reflectance which depends on the layer thicknesses, index of refraction, and wavelength of the light. Selective wavelength reflectors of this type which contain as many as nineteen separate layers are available. These reflectors are often used as beam splitters or wide-band filters where maximum rejection or transmission is desired. When two such wavelength selective reflectors are separated by a controlled spacer layer, a high efficiency filter results. For filters with transmission in the visible and red, the materials most often used are cryolite and zinc sulfide (ZnS) with a refractive index of 2.25 after being evaporated. (The index of ZnS is usually given as 2.4 but apparently is somewhat less due to the process of evaporation into thin films.) Alternate layers one-quarter wavelength

thick are evaporated, starting and ending with zinc sulfide, and the reflectors are separated by a cryolite layer of thickness equal to an even multiple of one-half of a wavelength. Filters containing as many as twenty-three evaporated layers are available. For wavelengths less than about 450 μ , zinc sulfide absorbs the radiation, so it is generally replaced by antimony trioxide (Sb_2O_3) which has a refractive index of 2.0 but transmits to about 230 μ . Various applications of this technique may be used to obtain filters specifically designed for special purposes. For instance, if a very narrow passband is not required but a sharp cutoff of the passband is desired, the filter may be made by evaporating two fifteen-layer filters separated by a quarter wavelayer of cryolite. Such a filter is often used when it is required that a nearby strong line emission be excluded.

The films must be evaporated onto a solid base called the substrate. This substrate also performs another important function. Since the filters utilize an interference principle, the presence of passbands other than that desired, must be considered. Passbands occur whenever the optical thickness of the spacer layer is any whole multiple of a half-wavelength. The exact position of passbands is somewhat subject to variation due to absorptions or other

properties of the materials used in the filter. A filter in which the optical thickness of the spacer layer is one-half wavelength at the passband for which it is designed is called a first-order filter. Such a filter will have a second-order passband at a wavelength of about one-half of that of the desired passband. These extra passbands are usually detrimental to the specific purpose of the filter and may be eliminated by use of the proper substrate. For instance, for filters in the visible, the substrate may be a colored glass which absorbs strongly at the unwanted passband and is highly transparent in the desired regions. A large variety of such glasses is available from the Corning Glass Works. When transmission is desired far into the red region of the spectrum, other materials are used, such as special calcium aluminate glass, lithium fluoride, magnesium oxide, and calcium fluoride. If the optical thickness of the spacer layer is equal to two half-wavelengths at the desired passband, the filter is called a second-order filter. Usually the passband of a second-order filter can be made appreciably narrower than that of a first-order filter. However, the second-order filter will have a first-order passband relatively close to the long wavelength side as well as a third-order passband to the short wavelength side. This generally

requires more blocking of unwanted transmission and as a result causes a reduction in desired transmission due to substrate absorption. Generally, careful consideration of the amount of blocking required is important, since excessive blocking reduces overall transmission.

An interference filter is described optically by the wavelength position, λ , of the peak of the passband, by the transmittance, T , at the peak of the passband and by the half-width (HW) which is defined as the width of the passband at the level where the transmittance is one-half the peak transmittance. Sometimes additional characteristics are specified to indicate the sharpness of the passband. Then such criteria as tenth-width (tw), or hundredth-width (hw), are used. Also the amount of blocking is sometimes specified as free filter range (FFR) given as a percentage of the wavelength of maximum transmittance. These specifications are given to characterize the filter action upon a parallel beam of light normally incident on the filter.

If light is incident on a filter at some angle other than the normal, the optical path through the spacer layer changes, and the wavelength position of the passband is shifted to a shorter wavelength. This effect may be analyzed as follows. As in a Fabrey-Perot interferometer, the

condition for transmission is that the optical path through the spacer layer be an integral number of half-wavelengths.

Thus

$$\frac{n\lambda}{2} = u d \cos \alpha \quad (2.1)$$

where d is the thickness of the spacer layer; u , the index of refraction of the layer; α , the angle of refraction in the layer; and n is an integer.

For normal incidence, $\alpha = 0$ degrees and $\lambda_0 = 2 ud/n$, where λ_0 is the transmission peak for normal incidence, then

$$\lambda = \lambda_0 \cos \alpha \quad (2.2)$$

In order to consider λ as a function of the angle of incidence of the light, note that $\cos \alpha = \sqrt{1 - \sin^2 \alpha}$ and $u \sin \alpha = \sin \theta$, where θ is the angle of incidence.

$$\lambda = \lambda_0 \sqrt{1 - \frac{\sin^2 \theta}{u^2}}$$

and

$$\Delta \lambda = \lambda - \lambda_0 = \lambda_0 \left(\sqrt{1 - \frac{\sin^2 \theta}{u^2}} - 1 \right) \quad (2.3)$$

A plot of this function for a particular filter is shown in Figure 2.1. Several important considerations for

the proper use of interference filters may be deduced from this function and Figure 2.1. First, the passband shift is always toward a shorter wavelength, and the magnitude of the shift is proportional to λ_0 . This effect is very useful, since a filter may be constructed so that the wavelength of maximum transmission is either exactly where desired or slightly greater than desired. If the latter is the case, the filter may be tuned for maximum transmission at the desired wavelength by tilting the filter with respect to the incident light. The effect of non-parallel light is also evident. It tends to broaden the filter passband toward the shorter wavelength side. This is an important consideration when designing an instrument which utilizes interference filters. If a small bandwidth is required, the field angle must also be small. As can be seen from Figure 2.2 the bandwidth of 10\AA filter would be useful only if the field angle were no more than five degrees. If large field angles are required, a broader bandwidth should be used so that the broadening is a small percent of the total width. This effect is even more objectionable if normal incidence is not used. The slope of the curve increases rapidly after about five degrees so that even a five-degree field angle would greatly broaden a passband if used at incident angles greater than five degrees.

Parallel light incident at angles other than normal also broadens the passband of the filter. This effect depends greatly on the materials and methods used in the filter construction. It is caused by polarization of the beam due to the multiple reflection. The passband for the light vibrating at right angles to the plane of incidence is at a shorter wavelength than the passband for the component which vibrates only in the plane of incidence. For the filters using multi-dielectric films as reflectors, this effect is primarily evidenced as a broadening of the passband. This effect is shown in Figure 2.2 for the same filter as used in Figure 2.1. Other types of filters, especially those using silver film reflectors, actually develop a splitting of the passband into a doublet of increasing separation as the angle of incidence is increased. Measurements and calibrations with filters used at large incidence angles must be carefully done.

A different technique for construction of interference filters has recently been studied in detail in Reference 20. A thin sheet of mica was used in place of the evaporated dielectric spacer layer. Filters of half-width less than 1\AA and transmission of as high as 70 percent were reported. A detailed theoretical study was made and production tech-

niques developed. The basic properties of these filters are similar to those already discussed, the major difference being the narrow bandwidth which has been attained. This requires also the use of very narrow field angles and accurate position of the filter wavelength. This latter requirement may be a source of difficulty in manufacture, since the thickness of the layers in a mica film may not be controlled to the desires of the filter maker. Also, large apertures may be a problem. As yet, these filters are not available as a standard item but probably can be made if the requirement exists.

The birefringent properties of such materials as quartz, calcite, and other transparent crystals have frequently been used to produce optical filters. Detailed description of the optical principles involved and the various techniques of filter construction are given in widely distributed scientific reports (References 21, 22, and 23). The filter consists, essentially, of a block of quartz oriented with its optical axis in the plane face of the crystal and placed between two polaroids. The filter transmits radiation in sinusoidal passbands which scan in wavelength as the back polaroid is rotated. Thus, a spectrum line is optically modulated while a continuous background is not. The width

and separation of the passbands may be controlled in manufacture, and filters have been made with 3-Å passbands (Reference 21). The passbands extend over the wavelength range of transmission of the quartz, so that in practice a narrow-band interference filter is used to isolate the emission line, and the birefringent element is used to modulate the line.

In recent years, the most-used detector for visible radiation has been the photomultiplier tube. Continuing improvements are being made in the efficiency of photocathodes and amplifier stages. At the present time, a quantum efficiency of greater than 20 percent in some parts of the spectrum is available with a dark current of about 2×10^{-3} microampere which is equivalent at high sensitivity to an input of about 10^{-11} lumen. This figure can be lowered by a factor of between 10 and 100 by coating the cathode. Current amplification is as high as 10^8 and may be usefully varied down to about 10^5 by varying the supply voltage.

A very significant advantage of the birefringent photometer is its ability to discriminate between background and line emission. Its use assures that the photometer at all light levels is limited only by signal-to-noise considerations. This is in contrast to photometers which employ

two or more interference filters, one of which is centered on the emission line to be detected, and discrimination is accomplished by comparison techniques. A further advantage of the birefringent photometer is a practical one, that is, that the output electrical signal is directly proportional to signal strength, and no computation is required to perform discrimination. The birefringent element may be used with relatively wide field angles; this does not increase the effective field of an instrument which is limited by the accompanying interference filter, but it does reduce the aperture required for the more complex and expensive birefringent element. Birefringent elements must be specifically designed for individual uses, but they are easily produced by a competent optical shop.

2.2.2 Photometer Background. Considerable thought and planning have gone into specific photometer design before the decision to resume high-altitude nuclear tests. This work was performed under the Vela Sierra program for Air Force Technical Applications Center (AFTAC). During September 1961, photometers were built and manned at an Alaska observing site for AFTAC. Over the past several years, photometers have been built and operated by Geophysics Corporation of America (GCA) for various purposes including the detection

of resonance scattering from contaminants released into the upper atmosphere over Wallops Island to study atmospheric dynamics. The optical, electrical, and mechanical characteristics of the field equipment for detecting resonance scattering from debris released during the 1962 high-altitude tests evolved from this backlog of previous work and experience.

Two types of photometers were designed and built for the 1962 tests. Their general characteristics will be discussed in detail below. In both types of instruments, photomultipliers with high cathode efficiency and filters have been used. As discussed previously, the filters are manufactured to tolerances as close as the state-of-the-art permits, consistent with short delivery time and large quantity production. Improvements are possible for future instruments by advancing the manufacturing techniques and by constructing over a longer time interval, permitting the use of more selective and exacting methods.

2.2.3 Birefringent Photometers. The optical characteristics of a birefringent photometer are treated in detail in several publications. In its simplest form, it consists of an interference filter followed by an objective lens, a birefringent element, a field stop, photomultiplier, and

subsequent electronic or recording units (Figure 2.3). This combination permits the modulation of an emission line in the presence of background in such a manner that the modulated component of the photomultiplier is proportional to the emission line strength but independent of the intensity of the background.

It is desirable for most photometric purposes to have the aperture of the instrument as large as possible. Since the first element is an interference filter, this unit really determines the aperture area. The conventional dimension for interference filters is about two inches or less; on occasion, experimental filters five to six inches in diameter have been built, but the cost and production difficulties make them almost impossible to obtain in quantity on short notice. Furthermore, the lack of homogeneity over such large surfaces usually affects the bandwidth adversely, such that the optical value of these units is possibly less than that of a smaller filter of narrower effective bandwidth. After some investigation, testing, and evaluation, it was determined that, considering all parameters, it was feasible to produce circular filters 3-1/2 inches in diameter with the inner three inches utilized for the aperture. The outside 1/4 inch around the disk showed considerable deterioration in band-

width and was masked off by the mounting arrangement. The filters utilized were produced by Thin Films, Incorporated, of Cambridge, Massachusetts, and were tested, measured, and evaluated by GCA. The procurement was a joint effort between these two organizations in that filters were made in small batches, tested immediately, and production techniques modified as required before others were produced.

It is very difficult to produce an interference filter which is centered exactly at the desired wavelength for light of normal incidence. As the filters are tilted with respect to the normal, the passband shifts toward the blue side of the spectrum. Hence, filters are usually made with their passbands a few Angstrom units to the red of the desired wavelength. The filters are then tuned by tilting them to the required angle. Cossets, or filter holders, were built which were later machined to the required angle to properly tilt the filter. Tilt angles were determined for each filter individually and were based upon the measured filter characteristics.

The objective elements were simple positive lenses of about ten-inch focal length and four inches in diameter. Since the purpose of the objective lens is simply to define a field angle, they need be nothing more than simple lenses.

The birefringent elements were manufactured to GCA specifications by the Valpey Crystal Company. They were made from natural optically clear quartz crystals which showed neither twinning, needles, nor other optical flaws. They were cut into an octagonal form to assist in mounting. Two blocks per complete filter were employed, measuring about 29 mm along the photometer optical axis (perpendicular to the z-axis of the quartz which is frequently termed the crystal optical axis). The faces perpendicular to this axis were oriented to within one minute of arc and were polished. The octagonal faces were parallel to the above axis and were not polished. The remaining two axes of the quartz elements were oriented in the above plane such that they passed through corners of the octagon to within one minute of arc. The aperture diameter (corner to opposite corner of the octagon) was 1-1/2 inches or longer depending upon the original quartz crystal from which it was cut.

The birefringent blocks were then mounted in a heavy aluminum slug which had been built to assure proper alignment of the elements and which could maintain a constant temperature. Polaroid, half-wave, and quarter-wave material was cut in octagonal shape to fit the aluminum holder and to aid in assembly. Lucite end plates were utilized as well. The

aluminum holder was wrapped with heating wire and insulated. A Fenwall off-on thermal switch was utilized to maintain the quartz elements at about 105^oF. The entire unit was assembled with layers of transparent mineral oil between all components to reduce the light losses from surface reflections.

Field stops were placed at the focal plane of the objective lens-birefringent combination. The field was tailored to five degrees, which is about the maximum permissible through the interference filter before the effective optical passband is adversely affected.

The photomultipliers employed were RCA 7265 tubes. These units have a tri-alkali cathode surface, which possesses good quantum efficiency throughout the visible portion of the spectrum, and have a gain of about 10^7 for total dynode voltage of 2,500 volts.

During the twilight interval, the light intensity varies over about four orders of magnitude. To accommodate this large range, the power supply driving the photomultiplier was made to be adjustable in 100-volt steps. The sensitivity of a photomultiplier is logarithmic with input voltage and covers more than four orders of magnitude between 1,200 and 2,800 volts. In this range the sensitivity increases by roughly a factor of two for each 100-volt increase in supply voltage.

Power supplies were built with the required regulation of voltage and freedom from ripple and voltage variations. The power supplies incorporated an indicating meter and a selector switch to adjust voltage in specific 100-volt steps. The power supplies were mounted to the photometer telescope physically following the photomultiplier. The supplies were made such that a complete unit could be quickly replaced in case of failure. They were hermetically sealed in anticipation of possible salt spray environment in which they might have to operate as in the case of the ship sites. In addition to hermetic sealing of the unit, potting and other precautions were taken to avoid corona discharge and ohmic leakage. A salt spray ambient places severe requirements on any equipment requiring high voltages. Figures 2.4 and 2.5 show views of this power supply. The photomultiplier tube socket is a part of this supply and is in the plane resting upon the table shown in Figure 2.4. Two outputs are normally used; one is a fraction of the supply voltage to record on a Sanborn two-channel recorder. This voltage and the second from the photomultiplier anode are amplified and displayed upon a second channel of the same recorder.

The back element of the birefringent photometer is rotated by a synchronous motor at 100 rpm. Hence, the anode

current contains an alternating component at about three cycles per second which is proportional to the line emission as described above. This 3-cps signal is amplified by a two-stage vacuum tube amplifier in the photometer telescope housing before it is sent to the recorder. A coding switch on the modulating motor shaft sends a signal to an event marker on the same Sanborn recorder. This serves as a phase reference signal and facilitates analysis of the data for those cases where the signal is comparable to or less than the noise fluctuations recorded on the chart. Figure 2.6 is a view of the two-channel Sanborn recorder used with the birefringent photometers.

During the initial few seconds after detonation, the birefringent photometers will record intensity at a single wavelength At the conjugate points the manifestation may last for longer intervals, and during twilight observations the time interval over which measurements are made is of the order of an hour. For such observations a turret wheel which accepts five interference filters has been provided. The various filters are indexed into the optical system by hand. In this manner, the utility of each photometer is considerably extended.

2.2.4 Four-Barrel Interference Photometers. During the early times after a detonation, it is extremely difficult to predict the light intensity which will exist via the resonance scattering mechanism. Hence, selection of the operating voltage by an operator is impossible, and time sharing of an optical channel by indexing filters into it would seriously degrade the data. The four-barrel photometer has been built to overcome these uncertainties. Four separate optical channels have been joined into a single unit with each channel functioning optically and electrically as an independent unit. The optical axes of the photometers are parallel and utilize the same mounting and pointing base. Each telescope employs a different interference filter centered on the emission wavelength for neutral lithium, neutral and ionized barium, and neutral zirconium. Figure 2.7 is a block diagram of the four-barrel interference photometer.

Due to uncertainty in the magnitude of the light intensity, the electrical output is logarithmic with light intensity. This has been accomplished by utilizing the logarithmic sensitivity of a photomultiplier with supply voltage. A supply voltage of 5,000 volts was the starting point for each channel. By means of a series resistor and two Victoreen corona discharge tubes, this input was dropped to 4,000 volts

regulated. A pentode in series with this 4,000 volts and the dynode resistor string permitted the total dynode voltage to swing from 1,000 to 2,800 volts with a voltage swing of 0 to 2-1/2 volts into the pentode grid. This voltage was derived from the anode current through a 1-megohm resistor. With this arrangement, it is possible to operate with light levels at the low point corresponding to the background created by starlight up to levels 10^5 times greater, with the total dynode voltage swinging from 2,600 to about 1,200 volts depending somewhat on the particular photomultiplier employed. Four separate power supplies were built into a single power unit which mounts behind the four telescopes and photomultipliers. Figure 2.8 shows one such power unit open, and Figure 2.9 shows a power unit with four barrels attached to the front of it. This power unit was hermetically sealed and utilized many potted components to avoid corona and leakage problems as discussed in a previous section.

Recording for the four individual photometers was accomplished with a Sanborn recorder with eight analog channels, two for each photometer, as shown in the foreground of Figure 2.10. The signal to the recorder consists of a portion of the dynode resistor current. Gain on one of the two channels is set to cover a range of light intensities

corresponding to night sky at the chart zero to light levels 10^5 times higher. The second channel gain causes a deflection from zero at the night sky intensity to fifteen times this value for full scale. The response time of the entire system is of the order of 10 milliseconds and is determined by the recorder response time.

The measurement of interference filter characteristics, selection of specific filters, and selection of filter tilt angles followed the same procedures described for the birefringent photometer.

2.2.5 Photometer Accessories. Both of the above photometer installations use the same base, azimuth and zenith angle controls, as well as the same general method for recording these two directions. The base is built of heavy steel to assure rigidity and is fitted with a sheet metal cover to protect it from the elements. A vertical shaft supported by two journals gives azimuth motion. It is adjusted in azimuth by a gear and worm arrangement. To the vertical shaft a yoke arrangement cradles the photometer and provides zenith angle adjustment also via a gear and worm arrangement.

Both the two-channel and eight-channel Sanborn recorders are equipped with eight-event markers or side pens. These have a total throw of about 1/4 inch and simply indicate

signal or no signal. Identical encoding units are attached to the azimuth shaft and to the zenith shaft of each photometer unit. The encoding units consist of a stationary printed circuit card and a moveable arm attached to the azimuth or zenith shaft which connects conducting elements on the printed circuit card. A series of five separate pulse groups are generated by a motor and rotary switch. Each pulse group is connected electrically to elements on the printed circuit. By connecting three of the event markers to each of the azimuth and zenith encoding units, it is possible to record information which defines azimuth and zenith angle to within three degrees. Since the photometers have a five-degree field, this accuracy is quite sufficient.

2.2.6 Calibrations. The optical parameters necessary to perform a calibration were all measured in the laboratory before the instruments went to the field and again when they returned from the field. While in the field, natural sources such as the Moon, Venus, and Jupiter were used to maintain a continuous record of instrument sensitivity.

The four-barrel photometers employed a feed-back arrangement between the photomultiplier anode and the high-voltage power source which gave a logarithmic response. It was necessary to use several sources of various known intensities to

obtain calibration points throughout the dynamic range of the instrument. For the birefringent photometers, only a single known source was necessary to perform the calibration.

In all cases the optical characteristics of the interference filter are important. Calibration is always performed with a known source of continuum light. The transmission, $T(\lambda)$, of each filter as a function of wavelength, λ , was measured with a high dispersion monochromometer. These measurements were made before going into the field and after returning from the field. The sun was used as a known source on clear days. Neutral density filters of known transmissions and diaphragm stops were used to reduce sunlight incident upon the instrument being calibrated. If the light of flux, $I(\lambda)$, from a point source is known, and if the instrument is pointed such that the source is within its field of view, then

$$R = T_f A k \int_0^{\infty} I(\lambda) T(\lambda) d\lambda \quad (2.4)$$

Where: R is recorder deflection

T_f is the transmission of any neutral density material employed

A is the aperture area of the objective or diaphragm if used

$I(\lambda)$ is the incident intensity from the source in photons/cm²-sec

$T(\lambda)$ is the interference filter as described above

λ is the wavelength

k is the instrumental calibration factor to be determined. It involves the photomultiplier sensitivity, electronic gain, and instrumental transmission. The integral appearing in Equation 2.4 is performed with a desk computer using intervals of about 1\AA for $d\lambda$. Since R is in chart units of recorder deflection, the units on k are units of deflection per photon with the other units as defined.

The birefringent photometers employed a power supply for the photomultiplier which was adjustable from 1,000 to 2,500 volts in 100-volt steps. It was necessary to determine for each photometer a value of k for each of the voltage settings employed. The birefringent element can be considered a device which modulates an emission line, but not continuum. Continuum light produces a direct-current deflection; therefore, the above values of k were determined by observing such deflections. For a line emission which fills the photometer field of view, the light flux, Φ , incident upon the photocathode is given by

$$\Phi = \frac{B A T (\lambda_0) \Omega}{4\pi} \quad (2.5)$$

Where: ϕ is the light flux in photons per second

B is the intensity of the line emission in
photons/cm²-sec-steradian

T(λ) is the net transmission of the instrument at
wavelength λ_0 of the line emission

Ω is the instrument field angle in steradians

The debris signal is a line emission which fills the field of view, and the value of B is to be determined from the recorded level and from calibration data. This line emission is modulated sinusoidally, and the recorder deflection can be thought of as a direct-current component proportional to the continuum background plus an alternating-current component proportional to the line emission.

Where R_{pp} is the peak to peak deflection of the alternating-current component,

$$R_{pp} = k \phi \quad (2.6)$$

where k is determined from Equation 2.4 and ϕ from Equation 2.5. Values of b are determined from these relations. In practice, values of k were determined with a vacuum tube voltmeter at the photomultiplier anode, and the alternating-current signal was amplified with an amplifier of known gain before applying the electrical signal to a Sanborn recorder.

Amplifier gain and recorder sensitivity was then independently measured to obtain an effective k for the entire system.

For the four-barrel instruments with direct-current recording and logarithmic response, Equation 2.4 is still valid, but k is itself a function of light intensity incident upon the instrument. For this type instrument the observed deflection is the sum of line emission and continuum. These instruments were calibrated by measuring the interference filters, and using the sun plus neutral density filters to determine sunlight entering the optics. Deflections were then plotted on semi-log paper against known light fluxes. As described previously, they were meant to record the rapid motion of debris into sunlit regions for events scheduled just prior to morning twilight. To use them to detect debris during twilight several hours after event time, it was necessary to subtract values of a normal twilight (no debris present) from readings following an event. For the first twilights following an event when debris concentration was fairly high and for large depression angles where the background to be subtracted was low, this process was fairly accurate. Under other circumstances, the four-barrel instruments were not considered reliable.

The various parameters involved in the calibrations

were measured with sufficient precision to permit determinations of debris signal intensities to within 10 percent. However, some deterioration in interference filters during the field operation was noted by comparing the $T(\lambda)$ measured before and after going into the field. This effect varied from instrument to instrument and filter to filter, but caused an uncertainty of about twenty percent on the average. This uncertainty is comparable to or less than that caused by local sky transmission. The effect of clouds upon the data will be discussed in Chapter 3.

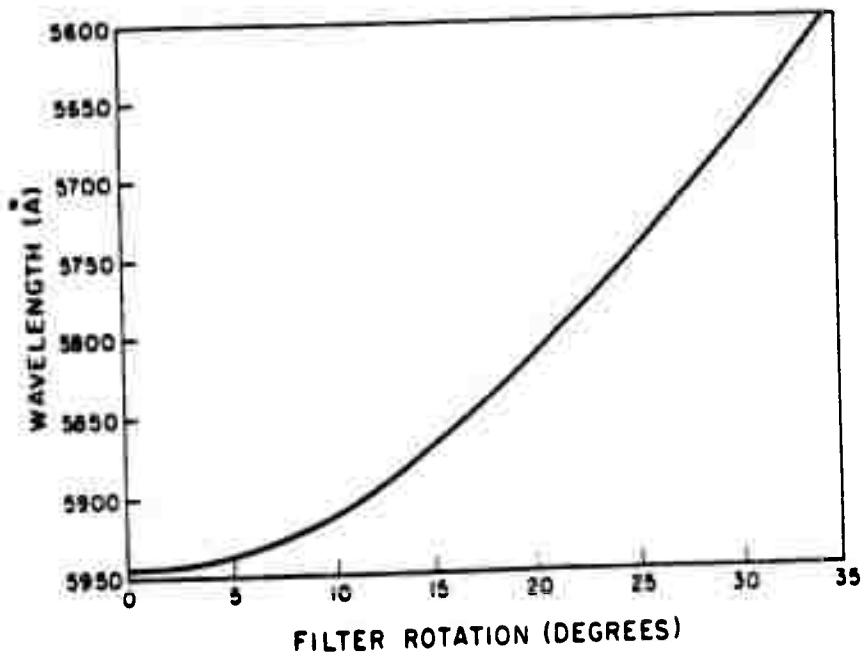


Figure 2.1 Shift in position of passband of an interference filter as a function of incidence angle.

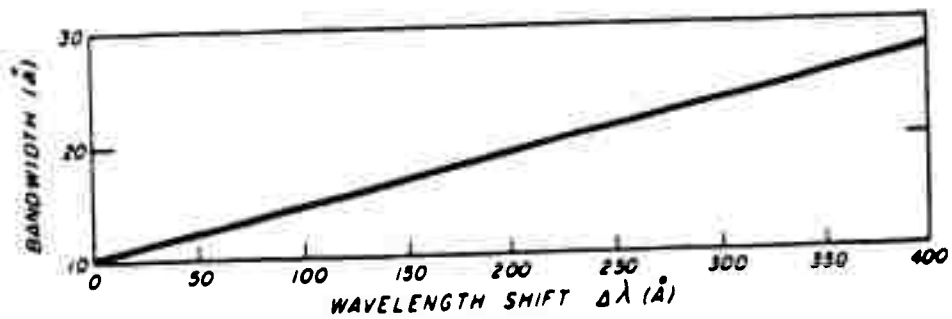
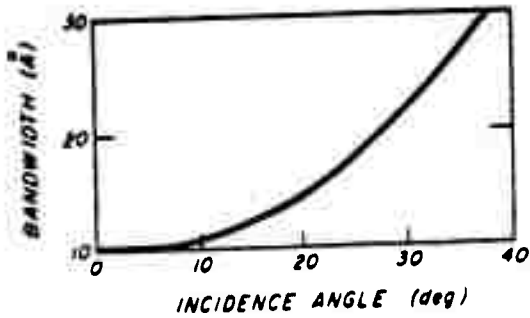
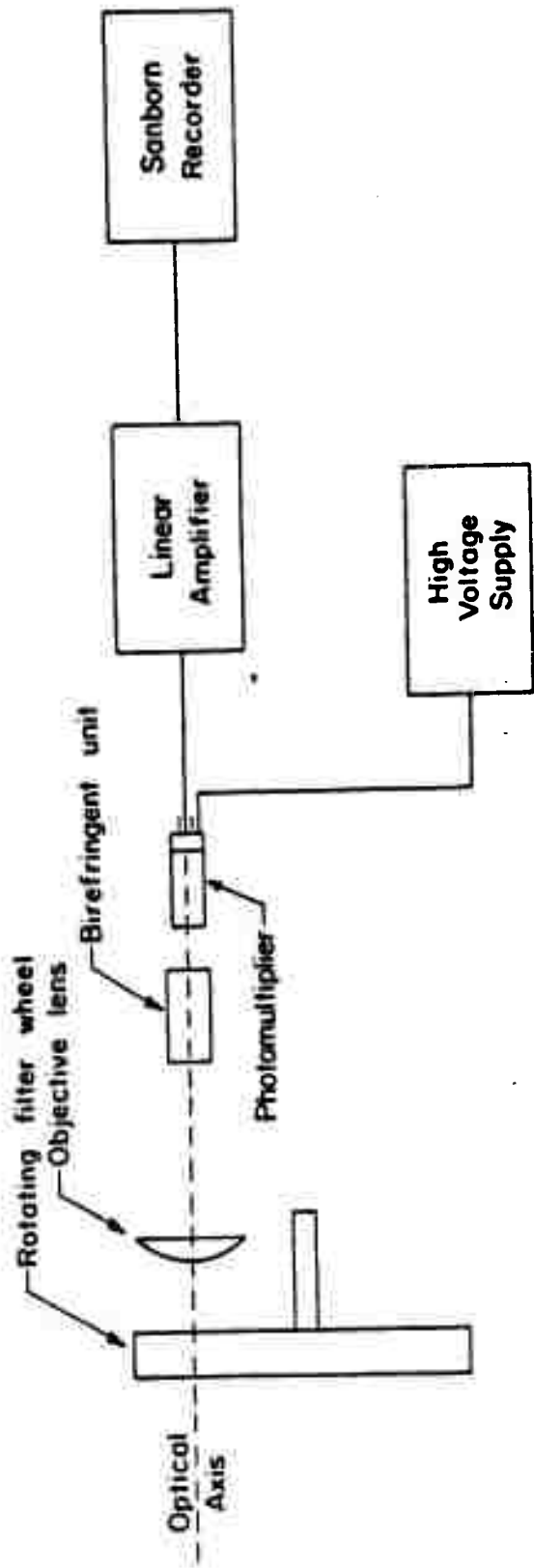


Figure 2.2 Broadening of the passband of an interference filter as a function of incidence angle and wavelength shift.



Manual selection of filter position and of high voltage

Figure 2.3 Birefringent photometer block diagram.

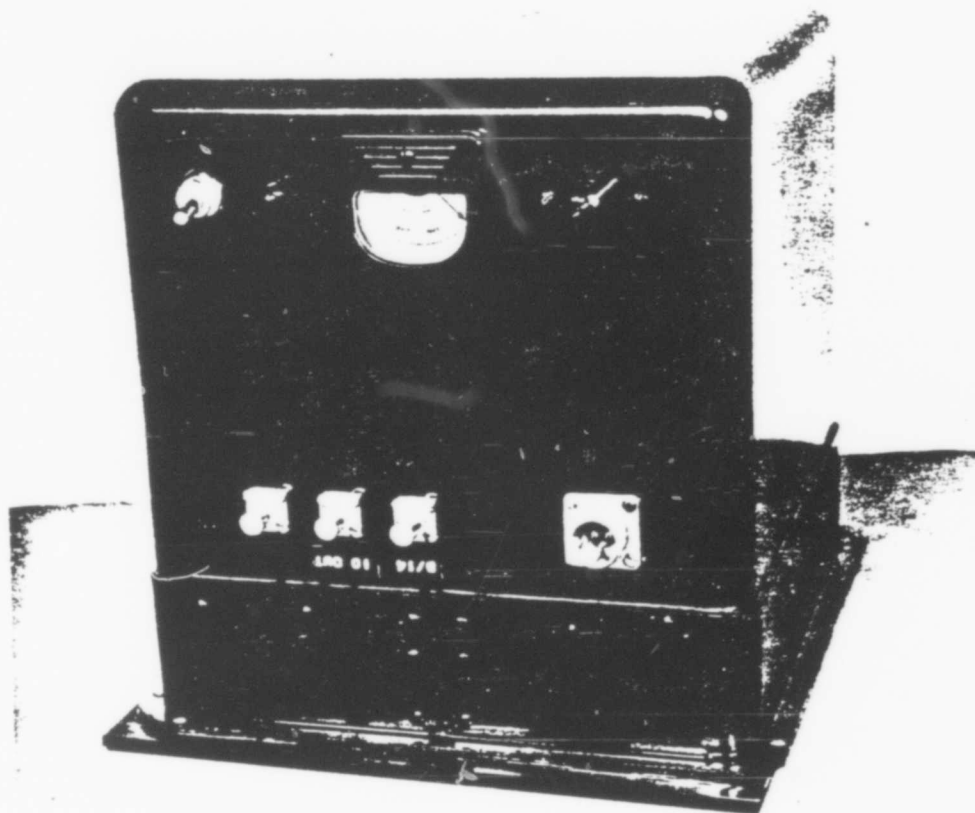


Figure 2.4 Power supply, front view. (GCA photo)

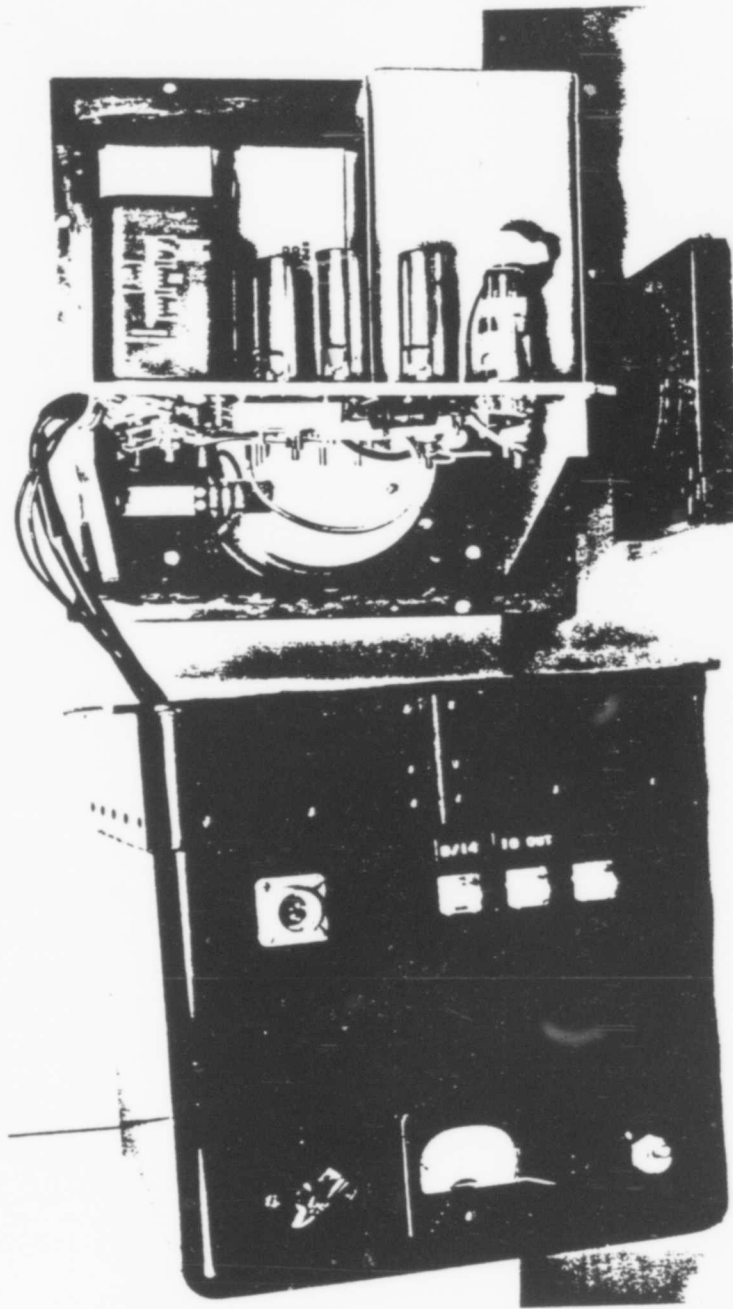


Figure 2.5 Power supply, inside removed. (GCA photo)

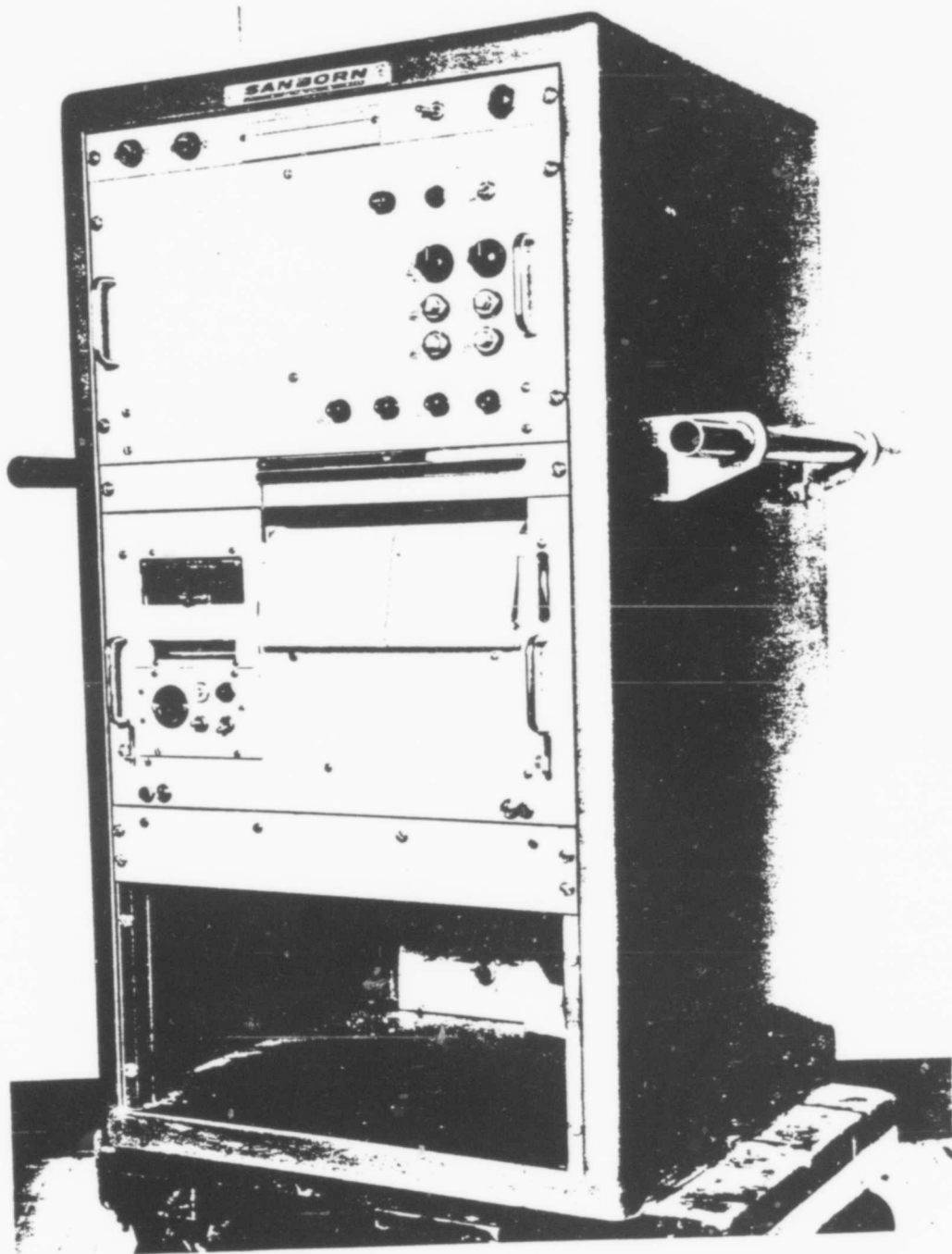


Figure 2.6 Two-channel Sanborn recorder (birefringent photometer).
(GCA photo)

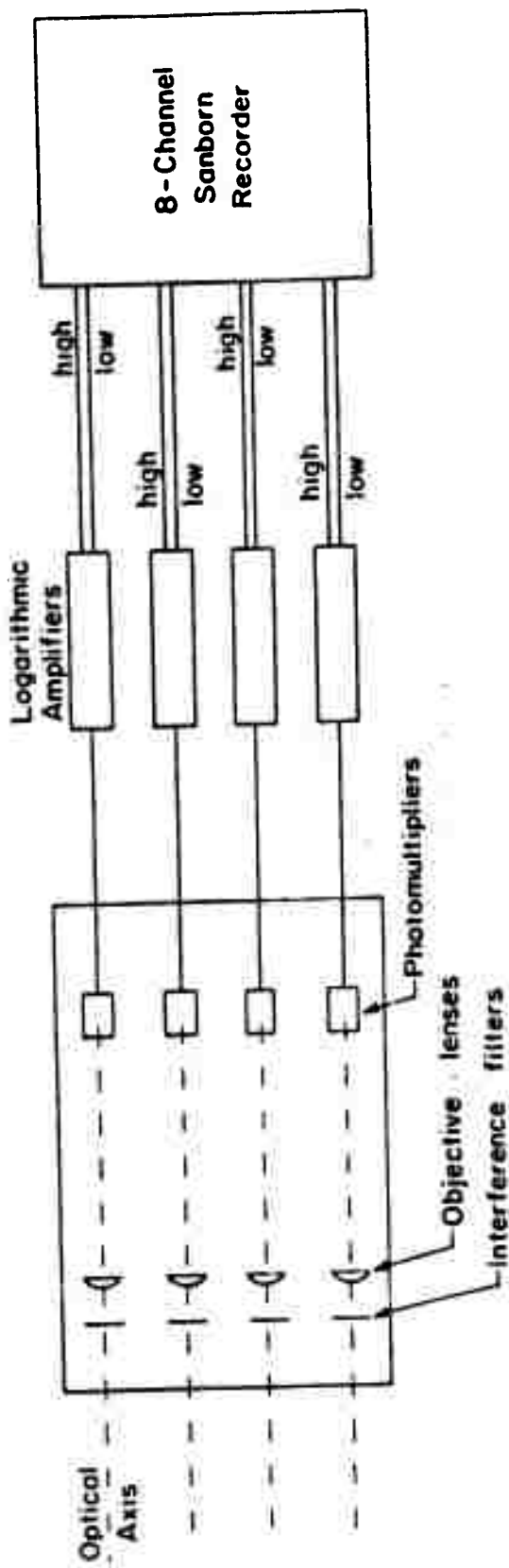


Figure 2.7 Block diagram of four-barrel interference photometer.

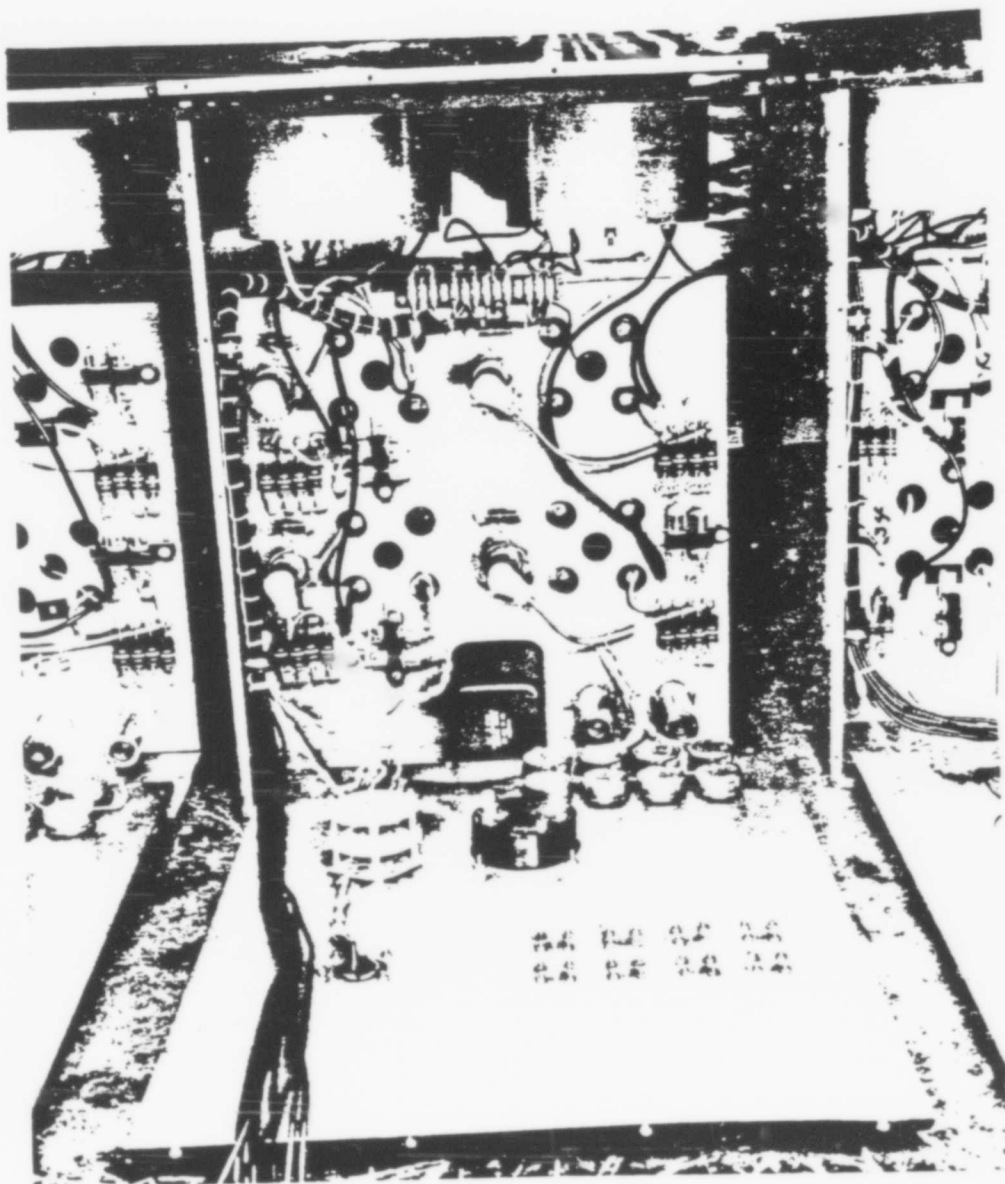


Figure 2.8 Interference power unit, open view. (GCA photo)

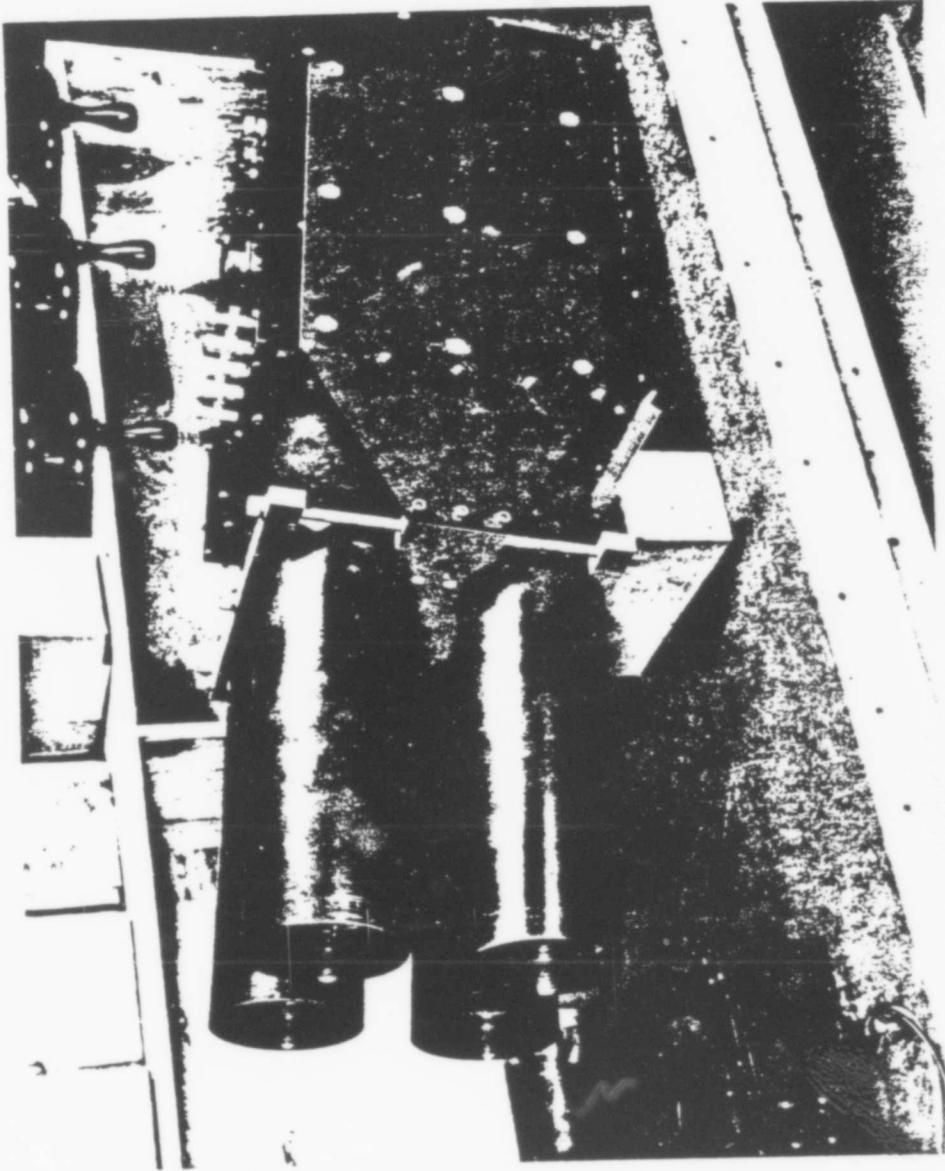


Figure 2.9 Four-barrel interference photometer with attached power unit. (GCA photo)

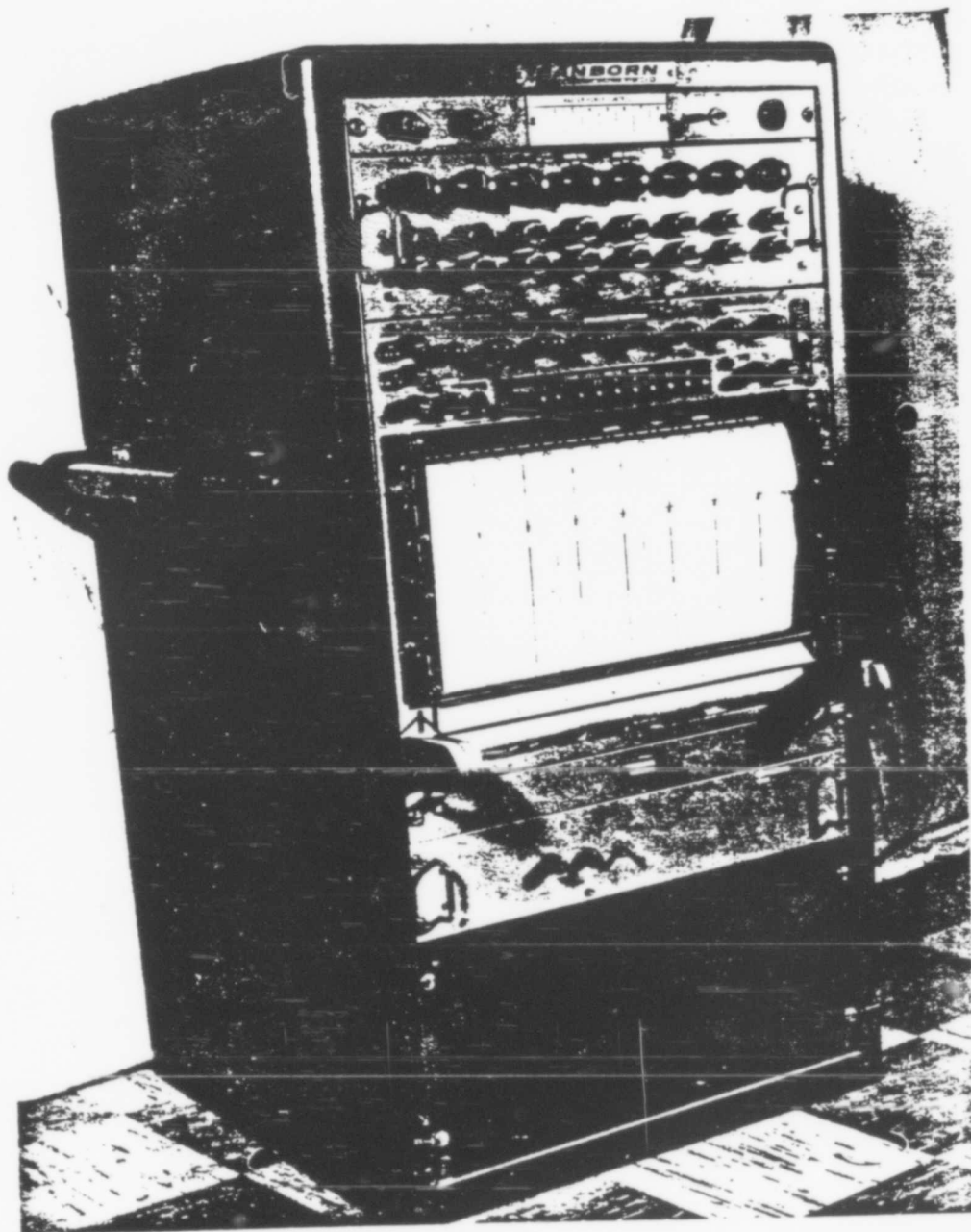


Figure 2.10 Eight-channel Sanborn recorder (interference photometer).
(GCA photo)

CHAPTER 3

DATA PROCESSING

3.1 DATA REDUCTION

The following two sections will consider specific details in the process of data reduction. Light intensities were recorded in an analog fashion on Sanborn recorders utilizing thermal-sensitive recording paper. Time was marked along the abscissa (axis of paper transport) of the charts utilizing chronometers set to WWV. Between these time marks (placed each 3 to 5 minutes) a linear interpretation was used to determine specific times. In most cases, the frequency of the 110-volt ac power was not constant enough to interpolate over time intervals greater than 5 minutes. Utilizing the latitude, longitude, and calendar date, curves of solar depression angle against time were plotted for each twilight interval at each site. Data was read and tabulated as a function of solar depression angle. The depression angle parameter determines the earth's shadow height and the intensity of continuum background.

At regular time intervals, the reading of galvanometer deflection (along chart ordinate) was tabulated. From calibration factors these readings were converted into absolute

units of intensity due to debris. These intensities were then related to the quantities of sunlit debris above the observing sites. Some details of these conversions and methods are given below.

3.1.1 Birefringent Photometers. As explained previously, the rotating polaroid component of the birefringent element modulated monochromatic light scattered from debris, but it did not modulate continuum light. The rotation frequency of this component was $1\frac{2}{3}$ rev per sec which gave a modulation frequency to the photomultiplier output of twice this value, $3\frac{1}{3}$ cps. For very high continuum levels, the ideal filter characteristics begin to break down, and extraneous continuum modulation at $1\frac{2}{3}$ and at $3\frac{1}{3}$ cps can occur. The $3\frac{1}{3}$ -cps modulation of continuum is due to the interference filter passband characteristics and is usually quite small. It was negligible for solar depression angles greater than about 5 to 8 degrees as evidenced by twilight runs when no debris was present. The instruments went into the field with slightly defective polaroid material in May 1962. The defect was an inhomogeneity in transmission over the surface of the disk. This generated an error signal of $1\frac{2}{3}$ cps. It was not possible to analyze and correct the problem prior to the Star Fish event. After Star Fish, the problem was analyzed and better polaroid disks provided for all subsequent events.

The ac photomultiplier output was amplified and displayed as a 3-1/3-cps signal on the Sanborn recorder. Peak-to-peak deflections were read from the charts in chart units as a function of time. These units were multiplied by appropriate calibration factors to convert peak-to-peak readings to the number of sunlit atoms above the observing site. For solar depression angles where the 1-2/3-cps error signal was appreciable, the combined signals required special analysis to extract the peak-to-peak value of the 3-1/3-cps component.

The separation of these two signals was accomplished by generating a waveform like the observed waveform from known sources of 1-2/3- and 3-1/3-cps components in the laboratory. It was necessary that the amplitudes of the 1-2/3- and 3-1/3-cps inputs as well as their relative phase be selectable if a perfect match of waveforms was to be achieved. After a match was obtained in waveform, the ratio of a characteristic dimension of the combined wave to the peak-to-peak amplitude of the 3-1/3-cps component was determined. The ratio was then applied to readings from observations and the debris densities determined as before. Figure 3.1 shows an almost pure 3-1/3-cps debris signal during the morning twilight following Star Fish as observed from S-5, and a

trace twenty days later when the debris signal had greatly diminished and at a solar depression angle when the 1-2/3-cps extraneous signal was significant. As mentioned above, for very high continuum levels a 3-1/3-cps extraneous signal sometimes appeared. This effect is not considered further since it was too small to influence the data presented in this report.

3.1.2 Four-Barrel Photometers. The four-barrel photometers had a logarithmic response as described in the instrumentation and calibration sections. Their response was a function of all light transmitted by their interference filters; that is, debris signal plus background. The outputs of each of the four photometers of the unit were recorded on two channels of a Sanborn in order to provide a greater dynamic range. The sensitivity of each photometer was adjusted to give about one-fourth scale deflection from night sky alone on the most sensitive recording channel. This assured that the instrument was as sensitive as background levels would permit. Since the lunar phase changed appreciably during the field runs, frequent adjustments of sensitivity were required. Calibrations using direct light from the moon and planets were performed each time the sensitivity was altered.

The normal twilight background can be subtracted from a measurement containing background plus debris to determine the debris contribution to observed light levels. This procedure is very imprecise due to uncertainty in cloud cover, haze, and other variables from twilight to twilight. It was found that zirconium signals, when they appeared at all, were only evident from solar depression angles below about twelve degrees. This is due no doubt to the relatively small amount of zirconium released and to its atomic weight. By determining the ratio of the zirconium deflections to others, it was possible to eliminate in large measure the effects of cloud cover. The method assumed, however, that for a particular depression angle the zirconium present was small compared to the other constituent being determined. In those cases where small amounts of zirconium were present, the determined value of the other constituent would be too small by an amount about equal to the zirconium contribution. This method was used to evaluate and reduce data reported for barium, and ionized barium above twelve to fourteen degrees' solar depression angle. The uncertainty in the data for these species is perhaps thirty percent above fourteen degrees' depression angle, and greater for lower angles to a point (ten or twelve degrees) where this type photometer is no longer reliable.

Zirconium concentrations had to be determined by subtracting twilight without debris from twilight plus debris data. The fact that zirconium concentrations were near the instrumental threshold and that signals appeared only at low depression angles makes these readings quite inaccurate. They are probably not to be relied upon to better than a factor of ten.

3.2 ARITHMETICAL OPERATIONS

CHAPTER 4

OBSERVATIONS AND RESULTS

Each twilight was observed at all sites when operators were on site with equipment installed. This procedure was established to insure that the equipment was maintained in good order and to familiarize the operators with various sky conditions and methods of observing. The data obtained prior to event times was useful in evaluating instrument stability and provided a backlog of calibration characteristics. In the case of the four-barrel interference photometers, it also provided a series of typical twilight levels which could be compared with data obtained after the events.

Island site locations are given in Table 4.1 and ship locations at event time in Table 4.2. The positions of the S-1, S-2, and S-4 for all events except Star Fish were so close to Johnston Island that, for the purposes of the present project, they may be considered as a single observing station.

4.1 BLUE GILL

4.1.2 Johnston Island. Following detonation, signals were well above background on all four filters and continued

so for about sixty minutes. The photometer was used to scan through the cloud along two diameters during this interval. The first scan started at the magnetic north edge of the cloud, passed through the cloud center, and continued out through the magnetic south edge. The second scan was perpendicular to the first passing through the cloud center.

No signals significantly above background were detected during any of the subsequent twilight observations.

4.1.3 French Frigate Shoals.

4.1.4 S-2, Henry County.

4.1.5 S-4, Point Barrow.

4.1.6 Tutuila and Tongatapu. At these sites a visible auroral-type streamer was observed. It contained negligible light at the filter passbands and was of short duration.

4.1.7 Wake. At event time, the sky was 75 percent covered with a hazy hole at the zenith. There was no visual phenomena and no detectable signal on the photometer at this time or during subsequent twilights.

4.1.8 Midway. Heavy overcast and intermittent rain hampered observations at event time.

No further signals were observed during the following twilights.

4.2 KING FISH

4.2.3 Tutuila. At event time, there was a general illumination of the clouds in the conjugate area. The photometer had the 4554 \AA filter in place to detect the presence of ionized barium. A short pulse of a few seconds' duration was recorded. Other filters were indexed into place, but nothing was detected.

Ionized and neutral barium were last detected during the morning twilight at H plus 51 hours. The morning twilight at H plus 27 hours permitted a determination of the concentration of ionized and neutral barium as 8×10^6 and 2×10^6 atoms/cm² column, respectively. The zirconium channel did not show more than a trace of signal, if at all.

4.2.6 S-1, Summit County.

4.3 CHECK MATE

The only signals from debris which were positively identified were due to ionized and neutral barium at and near Johnston Island. The first morning twilight gave signals corresponding to 8×10^7 ions/cm² and 10^7 atoms/cm² column. The signals decayed rapidly and were not detected beyond the first evening twilight.

4.4 STAR FISH

Barium and zirconium signals comparable to King Fish were observed from Johnston Island.

4.4.1 S-5. The sky was clear for the event and illuminated to the horizon in all directions.

The sky was mostly clear during the twilight following the event.

4.4.2 Johnston Island, S-2, and S-4. The four-barrel photometer detected strong signals through all filters for about thirty minutes after event time. Scattered high clouds increased to partly cloudy with both cirrus and altocumulus for the first morning twilight. Quantitative measurements were

Subse-

quent twilights were subject to bad weather and varying background conditions that precluded accurate determinations with this type of photometer.

4.4.3 Wake. This birefringent site had a solid overcast and rain showers at event time with no visual or instrument indications recorded.

4.4.4 French Frigate Shoals and S-1. Bright auroral effects with general sky illumination that decayed in a matter of minutes were observed from these sites at H-hour. For

4.4.5 Tutuila and Tongatapu. Although these sites were almost completely covered by clouds, they observed the same type effects as did the northern conjugate points at event

time.

No other observations were available because of rain. The instrument at Tongatapu was unable to detect any debris during the few twilights available subsequent to the event.

4.4.6 Midway. Observations lasting several minutes were made at event time, both visually and with the interference photometer. During subsequent twilights, this site had a total of eleven observations between the period 9 July AM through 13 July.

The measurements made during the latter days of this period are subject to some scrutiny because of a variable background created by a combination of moon and clouds.

4.5 TIGHT ROPE

The two southern sites saw no manifestation at event time. French Frigate Shoals saw a very brief flash but no indication on the instrument. The shipboard sites in close to Johnston Island and the Johnston Island site detected self-luminous radiation for approximately thirty minutes.

None of the sites detected signals that could be attributed to the Tight Rope event during subsequent twilights.

TABLE 4.1 ISLAND LOCATIONS

Site	Latitude	Longitude	Distance from Johnston Island km
Johnston Island	16 20'N	169 30'W	-----
French Frigate Shoals	23 10'N	166 10'W	910
Tutuila	14 20'S	170 50'W	3,880
Tongatapu	21 10'S	175 10'W	4,300
Midway	28 10'N	177 20'W	1,500
Wake	19 20'N	166 40'E	2,320

TABLE 4.2 LOCATION OF SHIPS FOR EVENTS

Event	CHECK MATE	BLUE GILL	KING FISH	TIGHT ROPE	STAR FISH ^a
Ship					
	1 2	1 2	1 2	1 2	1 2
S-1	392 191	24 198	74 198	3 191	575 0
S-2	152 271	24 186	80 012	7 209.5	275 180
S-4	140 112	29 186	64 187	12 204.5	275 90
S-5	-- --	-- --	-- --	-- --	575 180
The location of Johnston Island from ground zero					
J.I.	78 191	35 192	70 191	3 191	31 190

Column 1, kilometers from ground zero

Column 2, azimuth in degrees from true north from station to GZ

^a Equipment from S-5 was removed after S.ar Fish for use in the Gamma Delta program.

TABLE 4.2 LOCATION OF SHIPS FOR EVENTS

Event	CHECK MATE		BLUE GILL		KING FISH		TIGHT ROPE		STAR FISH ^a	
Ship	1	2	1	2	1	2	1	2	1	2
S-1	392	191	24	198	74	198	3	191	575	0
S-2	152	271	24	186	80	012	7	209.5	275	180
S-4	140	112	29	186	64	187	12	204.5	275	90
S-5	--	--	--	--	--	--	--	--	575	180
The location of Johnston Island from ground zero										
J.I.	78	191	35	192	70	191	3	191	31	190

Column 1, kilometers from ground zero

Column 2, azimuth in degrees from true north from station to GZ

^a Equipment from S-5 was removed after S.ar Fish for use in the Gamma Delta program.

TABLE 4.3 SKY CONDITIONS, FRENCH FRIGATE SHOALS, WAKE,
AND TUTUILA, KING FISH

Site	Date (Local)	Local Twilight	Hours After Event	Sky Condition	Comment
French Frigate Shoals	1962 1 Nov	AM	T + 3	Clear	Bright visible aurora after 10.8°
	1 Nov	PM	T + 15	Clear	100% overcast to 14°. Balance of run in clear sky
	2 Nov	AM	T + 27	Clear	
	2 Nov	PM	T + 39	Clear from 7 - 10° SDA	20% overcast at 10°. 50% overcast by 10.5°. Clear again at 11°
	3 Nov	PM	T + 63	Clear	
	4 Nov	AM	T + 75	Clear	
	4 Nov	PM	T + 87	Clear	
	5 Nov	AM	T + 99	Clear	
	5 Nov	PM	T + 111	Mostly clear	Variable 5% cover through run.
	6 Nov	AM	T + 123	Solid Overcast	100% overcast entire run. Rain for balance of twilight
	6 Nov	PM	T + 135	Clear	
	7 Nov	AM	T + 147	Solid Overcast	100% overcast entire run.

TABLE 4.3 (CONTINUED)

Site	Date (Local)	Local Twilight	Hours After Event	Sky Condition	Comment
Wake	1962 3 Nov	AM	T + 29	Variable Overcast	Partly clear from 8 - 9.2°. Heavy cloud prior to 9.2°
	3 Nov	PM	T + 41	Clear	Maximum concentration measured subsequent to event
	4 Nov	AM	T + 53	Clear	
	4 Nov	PM	T + 65	Clear	"Tight Rope" occurred at \approx 0730 GMT. No indication.
	5 Nov	AM	T + 77	Variable Overcast	Haze and scattered clouds. Run terminated by rain at \approx 7.0°
	5 Nov	PM	T + 89	Clear	
Tutuila	6 Nov	AM	T + 101	Mostly Clear	Some light scattered clouds up to \approx 8.6°
	1 Nov	AM	T + 4	Variable Overcast	Solid overcast by 10°
	4 Nov	AM	T + 76	Mostly Clear	Scattered light clouds.
	7 Nov	AM	T + 148	Mostly Clear	Scattered light clouds.
	8 Nov	AM	T + 172	Variable Overcast	Clear to overcast to rain.
11 Nov	AM	T + 244	Clear		

TABLE 4.4 SKY CONDITIONS, MIDWAY AND JOHNSTON, KING FISH

Site	Date (Local)	Local Twilight	Hours After Event	Sky Condition	Comment
Midway	1962				
	1 Nov	AM	T + 4	Clear	Heavy cumulus
	1 Nov	PM	T + 16	Mostly Overcast	Heavy cumulus most of run. 1/4 moon at 45° zenith.
	2 Nov	AM	T + 28	Overcast	Solid overcast entire run.
	3 Nov	PM	T + 64	Mostly Clear	Scattered cumulus. Heavy at end of run. 1/3 moon at 40° zenith.
	4 Nov	AM	T + 76	Clear	
	4 Nov	PM	T + 88	Mostly Overcast	Scattered cumulus to solid overcast. 1/2 moon at 45° zenith.
	5 Nov	AM	T + 100	Mostly Overcast	
	5 Nov	PM	T + 112	Variable Overcast	Scattered cumulus. 1/2 moon at 45° zenith.
	6 Nov	AM	T + 124	Mostly Clear	Scattered clouds latter part of run.
	6 Nov	PM	T + 136	Mostly Clear	Scattered cumulus. 2/3 moon at 45° zenith.
	7 Nov	PM	T + 160	Mostly Clear	Scattered cumulus. 3/4 moon at 50° zenith.

TABLE 4.4 (CONTINUED)

Site	Date (Local)	Local Twilight	Hours After Event	Sky Condition	Comment
Midway	8 Nov	AM	T + 172	Clear	
	8 Nov	PM	T + 184	Overcast	Intermittent Rain
	9 Nov	PM	T + 208	Overcast	Intermittent Rain
Johnston	1 Nov	AM	T + 3	Variable	Scattered cumulus
	1 Nov	PM	T + 15	Mostly Clear	Scattered cumulus. Clear in between.
	2 Nov	AM	T + 27	Mostly Clear	Scattered cumulus. Clear in between.
	3 Nov	AM	T + 51	Variable	Scattered cumulus. High haze.
	3 Nov	PM	T + 63	Mostly Overcast	70% cumulus
	4 Nov	AM	T + 75	Mostly Clear	
	5 Nov	AM	T + 99	Mostly Clear	Some scattered cumulus.

TABLE 4.50 SKY CONDITIONS, STAR FISH

Site	Date (Local)	Local Twilight	Hours After Event	Sky Condition	Comment
S-5	1962				
	9 July	AM	T + 6	Mostly Clear	Scattered cirrus
	9 July	PM	T + 18	Mostly Overcast	Cirrus plus scattered cumulus.
	10 July	AM	T + 30	Mostly Clear	Cirrus
	10 July	PM	T + 42	Overcast	Cirrus - altocumulus
	11 July	AM	T + 54	Solid Overcast	
	11 July	PM	T + 66	Clear	Light cirrus
	12 July	AM	T + 78	Overcast	Cirrus - altocumulus
Tutuila	9 July	AM	T + 7	Solid Overcast	Run terminated by rain
	10 July	AM	T + 31	Partly Cloudy	Cirrus. Scattered cumulus
	10 July	PM	T + 43	Mostly Overcast	Cumulus. Stratus. Rain.
Midway	9 July	AM	T + 7	Variable	Scattered cumulus. 50% cover.
	9 July	PM	T + 19	Solid Overcast	Stratus. Cumulus
	10 July	PM	T + 43	Solid Overcast	Intermittent rain
	11 July	AM	T + 55	Clear	

TABLE 4.50 (CONTINUED)

Site	Date (Local)	Local Twilight	Hours After Event	Sky Condition	Comment
Midway	11 July	PM	T + 67	Solid Overcast	Intermittent rain
	12 July	AM	T + 79	Mostly Overcast	Cirrus plus scattered cumulus
	13 July	AM	T + 103	Variable	Scattered cumulus
	13 July	PM	T + 115	Partly Cloudy	Thin altocumulus. 3/4 moon at 50° zenith
	15 July	AM	T + 151	Clear	
	15 July	PM	T + 163	Clear	Slight haze. Full moon at 65° zenith
	17 July	PM	T + 201	Partly Cloudy	Cirrus. Scattered cumulus
Johnston	9 July	AM	T + 6	Partly Cloudy	Cirrus. Scattered cumulus

CHAPTER 5

DISCUSSION

The first two considerations above have received considerable theoretical and experimental attention. The third is covered in large measure by Project 9.1 b. The fourth, that of diffusion, has received considerably less attention.

These observations are consistent with a model which showed King Fish debris to be stopped within a few tens of km, and then to have a subsequent rise by buoyancy to 400 or so km. During the rise, the debris cloud expanded, maintaining local pressure equilibrium, and at 400-km height was several hundred to a thousand km in diameter. Peak intensity at Wake in two days and at Tutuila in five days is attributed to expansion by wind, diffusion, or by both processes. The faint signal observed the first morning at Tutuila is not

explained by this process. Relatively hot or dynamic ions may have diffused or otherwise traveled along magnetic field lines during the early time or in the rising phase of the debris motion.

The detonation height of Star Fish was responsible for a broad distribution of material during early times. Strong signals were observed the first morning at all sites except the southern conjugate area, where bad weather makes interpretation of these records difficult. A weak signal was observed through clouds at Tutuila during first twilights; however, maximum signals were observed on about the fourth day. This was due presumably to diffusion from the detonation area, or from the point of deposition in the southern conjugate area. Tongatapu experienced very bad weather throughout the period and may have had instrumental problems. No signals were observed from Tongatapu. Wake observed a maximum about 36 hours after the event, presumably due to diffusion from the detonation region. Measurements from the S-5 indicate that debris went well north of the supposed northern conjugate region for Star Fish. This ship had been

placed below a point where undisturbed field lines through the detonation would intersect approximately the 150-km height region. During the first morning, north-south scans indicated that signal increased as far north as the instrument could look, which was limited by atmospheric attenuation at low elevation angles. Assuming a height of 130 km for the concentration maximum and an elevation angle of 20 degrees where attenuation is not serious, it is then surmised that the maximum concentration was 300 or more km to the north of S-5. Figure 5.6 shows the relative north-south intensities from S-5.

The amount of specific debris constituents for each device is fairly well known. It might be hoped that, using concentrations determined over each site, a total inventory might be performed. One of the uncertainties,

is the unknown degree of ionization.

represent this effect. The morning measurements are marked with an M and evening with an E.

Reliability to be associated with the tabular data is of the order of 90 percent from instrumental calibration. Uncertainty in atmospheric transparency is of the order of 60 percent for observations marked clear. Observations made through heavy clouds in some cases have been included for times and at sites where it was felt that data should be included, even where uncertain. Such data is probably no better than 10 percent. In the observing and reduction process, readings were made at times and positions near the zenith where the sky was clearest. Intermittent clouds, therefore, did not seriously degrade the results. The data from the southern conjugate area following Star Fish is generally inadequate to perform total or even relative inventory estimates. Bad weather and large distances between the two sites there does not permit an adequate representation of this important area.

In general, the instrumentation performed well. All sites were functioning except Tongatapu following Star Fish. Signals were observed in all other cases down to nearly the theoretically predicted thresholds. The bunching of ships near the detonation, except for Star Fish, was wasteful, and a considerable loss in spatial resolution resulted.

Appendix B contains later evaluation of the data.

CHAPTER 6

CONCLUSIONS AND RECOMMENDATIONS

6.1 CONCLUSIONS

Some of the apparent conclusions are summarized: (1) Low-yield, low-altitude devices do not lend themselves to a study by resonance scatter techniques. (2) Devices such as King Fish, Star Fish, very high yield weapons at 50 km or higher, and low-yield weapons salted with an appropriate material, give debris concentrations which can be followed for many days and over wide geographical areas. (3) An inventory of material cannot be made with a neutral species, unless the degree of ionization is established by independent techniques. Another species for which the neutral and ionized state can be observed should largely remove this uncertainty. (4) Diffusion is an important mechanism for the long-term spread of debris over wide areas. (5) Early time observations were made but have not been studied. This data also includes Tight Rope and some of the air drops. This data cannot be readily interpreted, and further study must involve other inputs. No resonance scattering was observed for any of these low-yield, low-altitude events.

Appendix B contains later evaluation of the data.

6.2 RECOMMENDATIONS

Recommendations are divided into two parts. The first deals with the present data and how it may best be used. The second deals with measurements and devices which, during any subsequent series, can yield important information by better utilization of resonance scattering measurements.

In the first case, it is recommended that this data be analyzed in conjunction with other experimental data such as riometer measurements, wind measurements, and experimental determinations of the diffusion coefficient at all heights of interest. Theoretical computations of long-term expansion which have been performed should be checked in terms of this existing data. If necessary, extensions of theoretical work should be performed. A good fit between theoretical prediction and observation will provide valuable knowledge for estimating the effects of nuclear detonations at all heights.

Spectral data from other projects should be studied. This will provide a determination of the event time luminosity. The photometer traces reported above may then be studied to evaluate temperature of the self-luminous areas and the atmospheric emissions excited by the detonation energy released. This information may be very helpful in the description of short-time expansion and initial cloud dynamics.

In the second case, hindsight clearly indicates improvements in observing techniques and modifications of experiments which can yield superior results. These are listed as follows:

(1) In view of launching difficulties, it seems improbable that events can be scheduled at precise depression angles when the four-barrel photometers can best be employed. However, these instruments have made significant short-time measurements and probably should be retained. It is recommended that a birefringent instrument be provided for at least one of the close-in sites to provide longer time data. This modification would require no additional personnel at the site. (2) Installations on ships are very desirable because of the ability to place them in predetermined locations and to change these from event to event. During the present series, however, ship locations were determined not by the photometric requirements but by other projects. Ships which can be deployed in accordance with all experiments aboard without too much sacrifice to anyone are especially suggested. (3) In the past, only debris species which occur naturally in the weapon have been observed. Where rocket capabilities exist, it is recommended that a few pounds of trace material (inert as far as the weapon is concerned) can provide an excellent source for photometry.

For example, barium beyond that expected from fission could be carried and provide measurements of both an ionized and neutral species fully as good as

Calcium, magnesium, and aluminum are cited as other possible constituents with which a nuclear weapon may be salted. In such cases, it would not be necessary to use a high-yield device to obtain very valuable data. A moderate-to small-yield weapon (10 kt) at the proper altitude and salted with one or many species could yield a vast amount of debris motion data. This includes both the short-time magnetically guided debris as well as the neutral debris which expands by wind and diffusion processes.

Aircraft should be considered as an observing platform, since they can fly above most cloud cover, can cover broad geographical areas, and can modify their flight plan if the data, or other data, indicates that debris has spread to other than predicted areas.

APPENDIX A

EFFECTS OF ATMOSPHERIC ATTENUATION

A.1 INTRODUCTION

The debris-tracking program utilized the resonance scattering of incident sunlight by atoms deposited in the upper atmosphere to study the long-term distribution of the material resulting from a high-altitude nuclear detonation. Photometric measurements of specific spectral lines were made during morning and evening twilight periods. Figure A.1 illustrates the general geometry of the situation and indicates that an important portion of the sunlight which is eventually incident on the debris must first pass through the earth's atmosphere. The effects of the atmosphere on the solar radiation passing through it, in terms of refraction, scattering, and attenuation must therefore be considered.

The resonance radiation from an atomic species in the upper atmosphere as received by a detector on the earth's surface is given by

$$I(\delta) = K \int_0^{\infty} \epsilon(\delta, h) \rho(h) dh \quad (A.1)$$

K includes constants of the optical system such as field of view, also instrument transmission between the source and the instrument, and the scattering rate of the observed debris when fully illuminated by unattenuated sunlight. $\epsilon(\delta, h)$ is the transmission factor to be applied to unattenuated sunlight to determine the actual solar energy incident on the debris at height, h , and at solar depression angle, δ . $\rho(h)$ is the number of debris particles per unit volume at height, h , and dh is an elemental height interval. If the effects of the atmosphere are neglected, the illumination function $\epsilon(\delta, h)$ will be unity outward from the earth's shadow line and zero within the shadow zone. Since the term $\epsilon(\delta, h)$ is a constant, it may then be taken outside the integral, so that for a given signal $I(\delta)$, a solution is found in terms of the integral of $\rho(h)$.

However, if atmospheric effects are considered, $\epsilon(\delta, h)$ will be a variable function of several atmospheric parameters, and because of certain smearing processes, the shadow line cutoff will no longer be sharp or well defined. The illumination function cannot then be taken outside the integral, and its variation with height must be investigated.

A preliminary survey of the literature revealed that comparatively little work has been done on the subject of

twilight illumination. Because of its importance in the investigation of airglow phenomenon, the subject has been investigated by workers in airglow and upper atmospheric physics. Chamberlain (Reference 25) has included a discussion of the general problem in his book on the aurora and airglow. Additional studies of the problem have been undertaken by various authors (References 26 through 29), and reference to their work will be made throughout this report. Unfortunately, none of the above papers are very detailed, and they generally concern themselves with situations and parameters not applicable to the area of interest.

Because of this lack of acceptable data, it was decided to carry out a detailed analysis of the effects of the earth's atmosphere on twilight illumination

The

following atmospheric processes were considered in the analysis: (1) differential refraction of incident radiation, (2) Rayleigh (molecular) scattering, (3) Mie (particle) scattering, and (4) ozone absorption. Each of these processes will be examined individually for its effect on a light ray passing at various heights above the earth's surface, i.e., selected rays will be traced through the atmosphere. Then the combined effect will be considered, and the final

results of the various ray tracings will be applied to the problem of debris in the upper atmosphere.

It should be noted that several simplifying assumptions have been made, owing to the requirement of generating transmissivity functions early enough to permit computer operation on the photometric data. These include the following:

(1) The field of view of the photometer is small such that horizontal variations of density over the linear field of the instrument may be neglected. The field of the photometer used is 5 degrees.

(2) The solar azimuth considered by Chamberlain (Reference 25) as a basic geometrical parameter has been neglected. Since this program was interested in ascertaining the corrections to be applied to the photometric data based on model atmospheres, it was felt that the application of solar azimuth was more appropriate to possible synoptic analysis in the future. It is to be noted that tables of solar azimuth can be prepared quite easily for each observation station in much the same manner as solar depression angle based on latitude and longitude of earth station and solar position. However, instead of considering all the individual stations, calculations of refraction and attenuation

of the rays have been made using only the depression angle δ as the solar position parameter.

(3) The effect of diffraction of the solar rays has been neglected. As the results of this analysis will show, the lowest altitude rays suffer appreciable diminution. It can be seen that diffraction effects are manifest in precisely the region of maximum attenuation (where $F(h)$ is so small that the $\rho(h)F(h)$ product is very small) so that it may be neglected.

(4) The fact that the finite size of the sun subtends an angle has not been considered. According to Huntten, (Reference 26), to a first approximation, one may consider the derived patterns to be smeared over a distance corresponding to about a half degree of arc, or about 10 km. For the sake of simplicity, all solar rays were considered initially parallel.

(5) Apart from the aforementioned effects of the various mechanisms influencing the solar illumination in its passage through the earth's atmosphere, i.e., refraction, Mie and Rayleigh scattering, and ozone absorption, no other effects were considered.

The purpose of this study was to determine the effects of refraction and attenuation of solar illumination on a distribution of material observed photometrically during

twilight. The previously mentioned references on the subject have shown that owing to the complexity of the problem, no unified solution is available. The effect of atmospheric attenuation of sunlight was investigated for three atmospheric models with widely varying characteristics. In subsequent sections, there are discussions of the several models assumed for each influencing factor. In general, three sets of final curves are presented for each solar depression angle which is considered: optimistic case (minimum attenuation), average case, and pessimistic case (including a tropical storm yielding variable and maximum attenuation).

A.2 DIFFERENTIAL REFRACTION

A.2.1 General Discussion. Owing to the difference in density between a finite value in the earth's atmosphere and a negligible value in free space, a ray of light incident on the atmosphere will undergo refraction, i.e., it will be bent away from its original direction of travel. Because of the variation of density with height within the atmosphere, the light ray will trace a curved path and emerge into free space at a fixed angle of inclination (the total angle of refraction) to its original direction.

Application of Snell's law of refraction to spherical surfaces leads to the relation

$$\mu r \sin i = \mu_0 r_0 \sin i_0 = \text{constant} \quad (\text{A.2})$$

Where: μ = index of refraction

r = radius vector to a point on ray path

i = angle of incidence of ray to the normal at this point

μ_0 = index of refraction at earth's surface

r_0 = radius of the earth = 6,371 km (assumed equatorial radius)

The index of refraction, $\mu(h, \lambda)$ is a function of the atmospheric density and the wavelength of the light being refracted and may be calculated by means of the relation (Reference 30)

$$\mu = n + 1 = \frac{A p}{T} \times 10^{-6} + 1 \quad (\text{A.3})$$

where

$$A = 77.5 \left(1 + \frac{5.15 \times 10^{-3}}{\lambda^2} + \frac{1.07 \times 10^{-4}}{\lambda^4} \right)$$

λ = wavelength of light in microns

p = atmospheric pressure in millibars

T = atmospheric temperature in $^{\circ}\text{K}$.

A graph of $n(= \mu - 1)$ as a function of altitude above the earth's surface is given in Figure A.2.

For the case of a ray of light from an object (e.g., a star) just on the horizon, i.e. with $i_0 = 90$ degrees, the total amount of refraction recorded by an observer at the earth's surface will be approximately thirty-five minutes of arc (Reference 25). If this ray were to pass completely through the earth's atmosphere, and emerge into free space, the total refraction would amount to twice this figure or about seventy minutes of arc.

Assuming an exponentially decreasing atmosphere, the angle of refraction for a ray of light which passes completely through the atmosphere is given by the expression: (Reference 31)

$$\alpha = \sqrt{2\pi a} v \exp(-a h_{\min}/r_0) \quad (\text{A.4})$$

Where: α = total angle of refraction in radians

$$a = 7.67 \times 10^2$$

$$v = \frac{\rho_0}{\rho} n - 1$$

ρ = atmospheric density

h_{\min} = altitude of closest approach of the light ray to the earth's surface

For purposes of calculation, the earth's atmosphere was assumed to approach zero density at an altitude of 40 km and to be horizontally homogeneous along the appropriate spherical surfaces in all its important properties. These assumptions will hold throughout the report unless otherwise noted.

For an earth with no atmosphere, an impact parameter may be defined by: $r_i = 6,371 + h_i$, where h_i is the distance of closest approach to the earth's surface (see Figure A.3). At large distances from the earth, μ approaches unity, and the incidence angle i approaches 90 degrees. Then

$$\mu r \sin i = r \sin i = \text{constant} = r_i \quad (\text{A.5})$$

which then fixes the constant to Snell's equation.

Because of the refractive properties of the earth's atmosphere, however, the ray will be bent and pass closer to the earth's surface than would be the case if there were no atmosphere. At the position of closest approach, the angle of incidence $i = 90$ degrees, and

$$\mu_{\min} r_{\min} = r_i \quad (\text{A.6})$$

where $r_{\min} = h_{\min} + r_0$, h_{\min} being defined in Equation A.4. Knowing the variation of μ with altitude, r_{\min} can be calculated for any given value of r_i (and vice versa). It can

be shown that the point of closest approach represents an axis of symmetry for a refracted ray path, the light ray following identical paths on either side of the minimum point. For convenience in initial calculations, it was assumed that the position of closest approach occurred along the normal XY (see Figure A.3) for all rays, regardless of altitude, an assumption which introduced a maximum error of approximately thirty minutes of arc into certain later calculations on optical path lengths.

As applied to the study of resonance scattering from debris in the upper atmosphere, the refractive properties of the earth's atmosphere produce the following three effects:

(1) Since the ray is bent away from its original direction and in toward the earth's surface, it will eventually illuminate part of the region within the earth's idealized shadow zone, thereby effectively lowering the earth's shadow height.

(2) A ray of light undergoing refraction will traverse a longer path through the earth's atmosphere than a non-refracted ray.

(3) Since a ray passing through the atmosphere at high altitude will experience less refraction than a ray at a somewhat lower height, originally parallel rays of light

will tend to spread apart resulting in a diminished solar illumination. (Note that the assumption is made that the sun's rays are initially parallel. As was mentioned in the introduction, no serious error is believed to result from this assumption).

Each of these effects will be discussed separately in the following sections.

A.2.2 Ray and Shadow Heights. Neglecting atmospheric effects, the height of a light ray above the earth's surface as seen by an observer located at a solar depression angle δ may be calculated from the relation (see Figure A.4),

$$h(\delta) = \frac{r_i}{\cos \delta} - r_o \approx 0.97\delta^2 \quad (\text{A.7})$$

Where: $r_i = 6,371 + h_i$ (km)

h_i = minimum ray altitude above the earth

δ = solar depression (degrees)

Note that the height of the earth's shadow is given by considering the ray with $h_i = 0$.

However, as previously discussed, after passage through the refracting atmosphere, a light ray will be bent away from its original straight line path and will illuminate part of the unrefracted shadow region. For accurate

calculations of twilight effects, it is necessary to compute the refracted heights of various solar rays as a function of solar depression. Both Link (Reference 27) and Fesenkov (Reference 28) have considered the problem of refracted ray heights for various values of h_{\min} and for solar depression angles between 0-15 degrees. Link, however, fails to discuss the procedure used for arriving at his results in any great detail, and a careful examination of his work reveals certain inconsistencies, especially for small angles of solar depression (i.e. < 6 degrees). Fesenkov does present a detailed discussion of his methods; however, his work, while very accurate, requires a time-consuming set of computations to produce final results.

It was decided to use an iterative approximation method for the initial set of calculations. It can be shown that the angular refraction (at least for non-horizon values) occurring between two points can be written as (Reference 32)

$$\Delta\alpha_{k,k+1} = C \left(n_{h_{\min}} - \frac{1}{h} \int_{h_k}^{h_{k+1}} n(h) dh \right) \quad (A.8)$$

where C is a constant of the geometry. Since this analysis is concerned with solar depression angles greater than 0, the expression is valid.

For a first approximation, Link's height data as a function of solar depression was used to fix the limits on the integral in Equation A.8. Starting from the known positions of minimum ray height ($h_k = h_{\min}$), the refractive angle was calculated for an increment of one degree solar depression by means of the equation

$$r_o + h_{k+1} = \frac{\cos (\alpha_k + \alpha_{k+1})}{\cos [\delta - (\alpha_k + \alpha_{k+1})]} (r_o + h_{\min}) \quad (\text{A.9})$$

Where: $\alpha_k = \alpha_{\min}$

$\alpha_{k+1} = \alpha_k + \Delta\alpha_{k,k+1}$ from Equation A.8

The height result thus obtained was then used as the initial point for the next increment of solar depression. Ray heights were traced for one-degree solar depression increments up to a height of 40 km. At this point, the refraction effects of the atmosphere were equated to zero, and the ray assumed a direction of travel at a fixed angle (the angle of total refraction) to its original non-refracted path.

The results of these calculations are presented in Tables A.1 and A.2. Table A.1 gives values for ray heights

resulting from use of Equation A.6, i.e., for a non-refracting atmosphere, while Table A.2 lists the results arrived at by use of the refractive approximation method described above. It should be noted that the ray which just grazes the earth's surface ($h_1 = 0$ km) in the non-refractive case is bent into the surface upon undergoing refraction. The ray in Table A.2 listed as having $h_{\min} = 0$ km would, for the non-refractive atmosphere, actually have passed at an altitude of approximately 1.7 km.

Also note that although refraction ceases after a light ray reaches altitudes greater than 40 km, the ray emerges at an angle to its original direction, and as the solar depression δ increases, the difference in altitude between the refracted and non-refracted cases will also increase.

A.2.3 Attenuation by Variable Refraction. Because of the exponential decrease of density with altitude, light rays passing at different heights will undergo variable refraction; in general, the higher the ray, the less the refraction. Let d be the separation between two rays before refraction. After passing completely

through the atmosphere, the originally parallel rays diverge, and the observed refracted separation D is a function of their original heights and the solar depression angle. As a consequence, the energy flux will be correspondingly decreased, and a new refracted intensity is given by

$$F(\delta) = \frac{d}{D(\delta)} F_0 \quad (\text{A.10})$$

where F_0 = original energy flux (solar constant in the wavelength interval of interest). From Tables A.1 and A.2, the separation between two adjacent beams is tabulated as a function of solar depression angle, and the attenuation factor $d/D(\delta)$ can then be calculated. The results are presented in Table A.3. An examination of these calculations reveals that even for a non-absorbing atmosphere the solar flux will suffer noticeable attenuation due to the effects of variable refraction. Applications of these results to the general debris problem will be made in Section A.5.

A.3 EFFECTS OF SCATTERING

A.3.1 General Description. Among the most impressive attenuation factors influencing solar energy incident on the earth's atmosphere is the effect of molecular and atomic (Rayleigh) scattering as well as particulate or Mie scattering caused by dust, water vapor, etc. The net result of these scattering mechanisms is a diminution in the intensity of a light beam. The resultant intensity is usually defined by

$$F = F_0 e^{-\tau} \quad (\text{A.11})$$

Where: F_0 = initial intensity of the ray

τ = optical thickness of the scattering medium

This is strictly true only for single scattering processes. Because of the computational difficulties involved in dealing with multiple scattering, this assumption of single processes was made.

The value of the factor τ depends upon the scattering efficiency of the individual particles and upon the total number of particles encountered. In turn, this total particle number is a function of the number density and the path length of the ray through the medium. In order to calculate the attenuation experienced by a ray of light, it is necessary to calculate values of τ for all paths of interest.

Generally, atmospheric scattering effects can be broken into two independent classes: (1) scattering from atoms, molecules, and other particles with dimensions much smaller than the wavelength of the incident light (Rayleigh scattering), and (2) scattering from aerosols and other particles with dimensions large compared to the wavelength of the incident light (Mie scattering).

Each of the above will be examined separately in the following sections.

A.3.2 Rayleigh Scattering. The method used for calculation of the Rayleigh optical thickness (τ_R) is illustrated in Figure A.5. The various ray paths of interest were considered to be symmetrical about their points of minimum approach (h_{min}). The path followed by a ray as it leaves its minimum approach position was traced through one-degree solar depression intervals. Using previous data (see Table A.2), the height of the ray above the surface at the initial and final boundaries of each of these one-degree increments was known, and the total path length of the ray across the interval could be approximated as follows: (see Figure A.5 for explanation of symbols)

$$\Delta X_{n,n+1} = (r_o + h_n) \Delta \delta$$

$$\Delta h_{n,n+1} = h_n - h_{n+1}$$

$$\frac{\Delta h_{n,n+1}}{\Delta X_{n,n+1}} \approx \tan \alpha_{n,n+1}$$

$$S_{n,n+1} = \Delta h_{n,n+1} \left(\frac{1}{\sin \alpha_{n,n+1}} \right) = \Delta h_{n,n+1} \csc \alpha_{n,n+1} \quad (\text{A.12})$$

The optical thickness due to Rayleigh scattering may then be calculated for each path interval if the scattering coefficient is known. For an exponentially decreasing Rayleigh atmosphere (in the case of the earth, this is a good approximation below about 100 km), the scattering coefficient is given by the relation

$$\beta_h = \beta_o \text{ Ray} \exp(-h/H) \quad (\text{A.13})$$

Where: $\beta_o \text{ Ray} =$

=

h = altitude of scattering particles

H = scale height = 8.0 km for Rayleigh atmosphere

Then

$$\tau_{n,n+1}^R = \beta_o \text{ Ray} \csc \alpha_{n,n+1} \int_{h_n}^{h_{n+1}} \exp(-h/H) dh \quad (\text{A.14})$$

The total optical thickness for a ray path extending from the position of minimum approach to the limits of the scattering atmosphere can then be found by summing the individual optical thicknesses over the region of interest. Since the ray path was assumed symmetrical about the minimum point, the total optical thickness for ray passage through the complete atmosphere will be twice that calculated above. Final results for ray paths of interest are presented in Table A.4. To a first approximation, these optical thicknesses may be considered to be relatively fixed values, the Rayleigh properties of the atmosphere remaining fairly constant with time and over wide ranges of location. As will be seen in the following sections, several models were proposed for Mie scattering and ozone absorption to obtain a measure of the attenuation limits. No such variability need be assumed in the case of molecular scattering.

A.3.3 Mie Scattering. Unlike the Rayleigh properties of the atmosphere, the Mie or particulate scattering undergoes considerable spatial and temporal variation. Of critical importance in calculating Mie scattering effects is the amount of water vapor present in the atmosphere. In the case of a water-laden cloud, the Mie scattering may be many times larger than for an average non-cloudy atmosphere. In general, it may

be said that Mie scattering effects predominate over Rayleigh effects near the earth's surface and then (neglecting high cloud cover) fall off very rapidly with height. For a cloud-free atmosphere, the Mie optical thickness for any given ray path may be calculated in exactly the same manner as the Rayleigh case.

$$\tau_{n,n+1}^M = \beta_0 \text{Mie} \csc \alpha_{n,n+1} \int_{h_n}^{h_{n+1}} \exp(-h/H) dh \quad (\text{A.15})$$

Where: $\beta_0 \text{Mie}$ = Mie scattering coefficient at sea level
 = 0.12/km for assumed average conditions
 H = typical scale height ≈ 2.5 km for Mie atmosphere

In the event that a light ray encounters cloud formations during its passage through the atmosphere, the situation becomes far more complicated.

To illustrate the effects of local meteorology on the photometric signal data, a storm was assumed to exist at a particular location as follows:

1. Cloud cover was due to a tropical disturbance whose center was located at a constant (over the twilight period) distance of 9 degrees' angular separation (~ 1000 km) directly along an east-west line to the point where debris observations were being made. The cyclonic cloud cover extended for 2

degrees on either side of the disturbance center (445 km diameter) from sea level to an altitude of 16 km.

2. Scattering coefficient within the cloud was $\approx 0.25 \text{ km}^{-1}$ with a scale height, $H = 5 \text{ km}$ (Reference 34).

3. Normal Mie scattering conditions existed at all points outside the cloud area.

The fact that the distance of the storm center from the observation site remains constant means that a light ray following a given path through the earth's atmosphere experiences varying effects due to the encounter with the clouds as the solar depression angle changes. For the assumed case with respect to positions of minimum approach, storm location, and dimensions, the maximum scattering effects due to clouds are experienced at a solar depression angle of 9 degrees, while no effects are noted for angles greater than 15 degrees. Finally, all light rays with minimum refracted altitudes (h_{min}) greater than 16 kilometers are not affected by the assumed cloud conditions.

The above cloud model is not meant to represent a true meteorological situation. Instead it serves to give some indication of the influence that clouds may have on the transmission properties of the atmosphere and resultant signal levels recorded by the photometers.

Tables A.5 and A.6 list total Mie optical depths for ray paths of interest. Table A.5 contains clear atmosphere results, while Table A.6 includes the results of the storm discussed above. In the case of Table A.6, the calculations consist of cloud effects plus ordinary Mie effects for all areas outside the assumed cloud formation. Reference to the tables shows that the optical depths encountered by low-altitude rays are large but fall off rapidly with increasing altitude for the clear atmosphere model. For the cloudy atmosphere model, the optical depths encountered above 16 km are completely due to the ordinary scattering atmosphere. For altitudes below 16 km, the optical thickness may be due to both cloud and normal Mie scattering or due exclusively to normal Mie scattering depending upon the location of the storm.

A.4 OZONE ABSORPTION

Ozone is formed in the upper atmosphere by photochemical reactions activated by solar ultraviolet radiation. Although a relatively minor constituent of the atmosphere, ozone absorbs strongly in the ultraviolet region and to a much lesser degree in the region centered around 6000\AA (Chappius bands). In the 6000\AA region, the absorption coefficient to the base e is approximately 0.044 per cm of ozone (Reference 33).

For a given location, ozone concentration exhibits both a seasonal and diurnal variation. In addition, its altitude distribution is also variable so that several ozone model distributions were considered (Reference 35). For each model, the ozone number density was reduced to normal temperature and pressure (NTP) atmospheric centimeters for altitude increments of 0.1 km by means of a computer. Ray paths through the ozone were then calculated in the same manner as discussed previously in the case of Mie and Rayleigh scattering. Optical thicknesses obtained from considering a total ozone concentration of 0.284 atmospheric centimeter distributed between 0 and 60 km shown in Figure A.6 are presented in Table A.7. Note that for low-altitude rays, the optical thickness due to ozone is small compared to the Mie and Rayleigh optical depths, but as altitude increases, the ozone effect becomes relatively more significant. For altitudes above 40 km, where the Rayleigh atmosphere is assumed to terminate, ozone absorption becomes the unique attenuation mechanism. Above 60 km, solar radiation is assumed unaffected by the earth's atmosphere.

A.5 TOTAL ATMOSPHERIC ATTENUATION

The various atmospheric attenuation processes have each been examined individually in the preceding sections; it is

now necessary to consider their combined effect on a ray of light passing through the atmosphere. The solar energy flux after passage through the earth's atmosphere is given by the expression

$$\begin{aligned}
 F &= F_0 \times \exp(-(\tau_{\text{Mie}} + \tau_{\text{Ray}} + \tau_{\text{Oz}})) \times \text{Refractive Factor} \\
 &= F_0 \times R \times \exp(-\Sigma\tau) \qquad \qquad \qquad (\text{A.16})
 \end{aligned}$$

Attenuation due to atmospheric scattering and absorption ceases after the ray has left the atmosphere but, because of refraction, the light rays emerge at fixed angles to their original direction. Their observed linear separation will then increase as a function of solar depression, and the energy flux will correspondingly decrease. The intensity of the solar illumination will therefore continue to diminish even after the ray has emerged from the attenuating atmosphere. The final expression for the solar flux contained in a given ray at a solar depression (δ) will then be:

$$F(\delta, h) = F_0 \times R(\delta, h_{\text{min}}) \times \exp(-\Sigma\tau[h_{\text{min}}]) \quad (\text{A.17})$$

where both τ and R are functions of the minimum distance of passage of the ray above the earth.

Values for R , τ_{Mie} , τ_{Rayleigh} , and τ_{Ozone} have been presented in Tables A.3 through A.7 for selected ray paths while ray positions after refraction are contained in Table A.2. Final calculations for total attenuation have been carried out using these values, and the ratio F/F_0 has been graphed as a function of observed ray altitude above sea level in increments of one degree for solar depression angles between 6 degrees and 15 degrees and for the 20-degree, 25-degree, and 30-degree cases (Figures A.7-A.10). Both the clear and cloudy atmosphere models previously discussed are presented, and an additional ideally clear atmospheric model having a total ozone concentration of 0.20 atmospheric cm, a Mie scale height (H) of 1.2 km and a $\beta_{\text{O Mie}} = 0.16/\text{km}$ as operating parameters has been included. For later use in data reduction programs, a second altitude scale using the earth's unrefracted shadow height as a reference is given in each graph ($h' = h_{\text{refracted}} - h_0$). Negative values on this scale are an indication of those rays which, because of refraction, penetrate below the earth's ideal shadow line.

In summation, the following atmospheric models are represented on the graphs:

- Ideal Atmosphere
- (1) Mie Scattering ($H = 1.2$ km, $\beta_0 = 0.16$ km⁻¹)
 - (2) Rayleigh Scattering ($H = 8.0$ km, $\beta_0 = 5.7 \times 10^{-3}$ km⁻¹)
 - (3) Ozone Absorption (total $O_3 = 0.2$ cm NTP, $\alpha = 0.044$ cm⁻¹)
 - (4) Refraction according to Link and Equation A.4

- Clear Atmosphere
- (1) Mie Scattering ($H = 2.5$ km, $\beta_0 = 0.12$ km⁻¹)
 - (2) Rayleigh Scattering = same as above
 - (3) Ozone Absorption (total $O_3 = 0.284$ cm NTP, $\alpha = 0.044$ cm⁻¹)
 - (4) Refraction according to Equations A.7 and A.8

- Cloudy Atmosphere
- (1) Mie Scattering ($H = 5.0$ km, $\beta_0 = 0.25$ km⁻¹ storm at 9 degrees angular distance from observation station with angular diameter of 4 degrees at height of 16 km)

(2,3,4) same as clear atmosphere case.

Minimum ray height values are indicated by points on the curves. Even for the ideally clear atmosphere model,

the lower rays suffer severe attenuation, and it is not until minimum altitudes above the effective Mie scattering region (10-15 km) are achieved that the atmosphere becomes reasonably transparent to solar radiation. Complete transparency is achieved only for altitudes above the ozone layer (60 km). For altitudes less than approximately 40 km, the deviation of the actual solar illumination curves from the idealized, non-refractive, non-attenuating atmosphere ($F/F_0 = 1$) is readily apparent.

Application of the computation is accomplished through numerical integration of Equation A.1

$$I(\delta, h) \rightarrow K \sum_{n=1}^{\infty} \epsilon_n(\delta, h) \rho_n(h) \Delta h \quad (A.18)$$

Small height increments of a few kilometers or less were used, and separate values of the illumination function as obtained from the computations were used for each height interval.

An arbitrary debris distribution was chosen, and the resultant signal level was calculated by means of Equation A.18 using values of solar illumination computed for each of the chosen model atmospheres. Figure A.11 shows the assumed debris distribution as a function of altitude, and

Figure A.12 the resultant signal as a function of solar depression for each of the atmosphere models.

The curves of Figure A.12 indicate the effects of extinction due to the three different models. The most significant observation is that although the models represent a wide range of atmospheric conditions, the effect on the signal is relatively small, being at most a factor of 2. This result might be expected since the major changes in the atmospheric attenuation occur at low altitudes where extinction due to long path lengths in a relatively clear atmosphere is high. For such paths, the transmission is so low through a clear atmosphere that a decrease due to increased large particle concentration or low clouds in the path of the solar rays would not appreciably affect the integrated line-of-sight signal.

Although the atmospheric models chosen have not been shown to give the maximum variation which could be attained, the postulated storm is large, and its effect extends to relatively high altitudes. Normal fair weather cloudiness is usually below 5 km, and these would have no effect on rays above this height. Below this level, the attenuation due to a clear atmosphere is so severe that transmission is negligible without consideration of clouds. Likewise, the

uncertain and widely varying distribution of large particle scatter at low levels has only a small effect on the signal.

At altitudes above the level influenced by large particle scattering, attenuation is determined by Rayleigh scattering and ozone absorption. Both of these effects are wavelength dependent, and thus each spectral region of interest must be considered independently. In some instances, latitude and cyclic variations of ozone distribution may be considered if adequate measurements are available. Sporadic local variations will be averaged over the long path lengths.

In general, this investigation indicates that widely varying characteristics of the lower atmosphere influence the results so slightly that analysis utilizing an average model atmosphere provides sufficient accuracy for interpreting the photometric measurements.

TABLE A.1 NON-REFRACTED RAY HEIGHTS (KM)

Min. Ray Height (h ₁) km	Solar Depression (δ) (degrees)									
	6°	7°	8°	9°	10°	11°	12°			
	Height of Earth's Shadow									
0	35.1	47.8	62.6	79.4	98.3	119.2	142.3			
1	36.1	48.8	63.6	80.4	99.3	120.2	143.3			
3	38.1	50.8	65.6	82.4	101.3	122.3	145.4			
5	40.1	52.9	67.6	84.5	103.3	124.3	147.4			
10	45.2	57.9	72.7	89.5	108.4	129.4	152.5			
15	50.2	62.9	77.7	94.6	113.5	134.5	157.7			
20	55.2	68.0	82.8	99.7	118.6	139.6	162.8			
25	60.2	73.0	87.8	104.7	123.7	144.7	167.9			
30	65.3	78.0	92.9	109.8	128.7	149.8	173.0			
40	75.3	88.1	102.8	119.9	138.9	160.0	183.2			
	13°	14°	15°	20°	25°	30°				
0	167.6	195.0	224.7	408.9	658.6	985.6				
1	168.6	196.0	225.7	410.0	659.7	986.7				
3	170.7	198.1	227.8	412.1	661.9	989.0				
5	172.7	200.2	229.9	414.2	664.1	991.3				
10	177.8	205.3	235.1	419.5	669.6	997.1				
15	183.0	210.5	240.3	424.9	675.2	1002.9				
20	188.1	215.6	245.4	430.2	680.7	1008.7				
25	193.2	220.8	250.6	435.5	686.2	1014.4				
30	198.4	225.9	255.8	440.8	691.7	1020.2				
35	203.5	231.1	261.0	446.1	697.2	1026.0				
40	208.6	236.2	266.1	451.5	702.7	1031.7				

TABLE A.3 REFRACTIVE DIMINUTION FACTORS, $F/F_0 = d/D(6)$

Min. Ray Interval	6°	7°	8°	9°	10°	11°	12°
0-1 km	--	--	--	--	--	--	--
0-3	--	--	--	--	0.385	0.357	0.333
3-5	0.526	0.500	0.435	0.417	0.455	0.429	0.408
5-10	0.610	0.543	0.515	0.476	0.554	0.526	0.505
10-15	0.676	0.641	0.608	0.574	0.708	0.699	0.671
15-20	0.820	0.781	0.765	0.743	0.850	0.836	0.823
20-25	0.893	0.877	0.871	0.866	0.927	0.895	0.892
25-30	0.943	0.926	0.935	0.918	0.962	0.962	0.944
30-35	0.980	0.980	0.971	0.971	0.967	0.963	0.959
35-40	0.980	0.980	0.971	0.971	0.967	0.963	0.959
	13°	14°	15°	20°	25°	30°	
0-1 km	--	--	--	--	--	--	--
0-3	--	--	--	--	0.191	0.162	
3-5	0.317	0.313	0.300	0.233	0.239	0.203	
5-10	0.386	0.367	0.354	0.285	0.316	0.275	
10-15	0.477	0.455	0.448	0.371	0.482	0.436	
15-20	0.662	0.638	0.627	0.552	0.679	0.637	
20-25	0.797	0.793	0.788	0.697	0.791	0.763	
25-30	0.888	0.885	0.881	0.841	0.906	0.895	
30-35	0.937	0.929	0.922	0.914	0.940	0.935	
35-40	0.955	0.951	0.947	0.944	0.940	0.935	

TABLE A.4 RAYLEIGH SCATTERING OPTICAL DEPTHS

Min. Ray Height (km)	τ_{Ray}	Min. Ray Height (km)	τ_{Ray}
1	3.58	20	0.26
3	2.81	25	0.13
5	2.09	30	0.07
10	1.02	35	0.04
15	0.51	40	0.00

TABLE A.5 MIE SCATTERING OPTICAL DEPTHS,
CLOUD-FREE ATMOSPHERE

Min. Ray Height (km)	τ_{Mie}
1	32.58
3	16.00
5	6.54
10	0.79
15	0.10
20	0.00

TABLE A.6 MIE SCATTERING OPTICAL DEPTHS,
CLOUDY ATMOSPHERE

Min. Ray Height (h_1)	Solar Depression (δ) (degrees)				
	6°	7°	8°	9°	10°
km	Height of Earth's Shadow				
1	40.00	50.00	60.00	60.00	60.00
3	35.48	46.72	55.31	59.35	55.31
5	19.38	27.83	34.57	37.29	34.57
10	4.53	7.97	11.41	12.81	11.41
15	0.23	1.47	2.72	2.85	2.72
20	0.00	0.00	0.00	0.00	0.00
	11°	12°	13°	14°	15°
1	50.00	40.00	>35.00	>35.00	>32.6
3	46.72	35.48	25.96	19.51	16.55
5	27.83	19.37	12.46	8.28	6.54
10	7.97	4.53	0.79	0.79	0.79
15	1.47	0.23	0.10	0.10	0.10
20	0.00	0.00	0.00	0.00	0.00

TABLE A.7 OZONE OPTICAL THICKNESS

Min. Ray Height (h_1) km	Solar Depression (δ) (degrees)				Remaining values of δ will have same optical depth values as $\delta = 9^\circ$
	6°	7°	8°	9°	
	Height of Earth's Shadow				
3	0.257	0.349	0.361	0.362	
5	0.314	0.374	0.377	0.377	
10	0.404	0.413	0.419	0.419	
15	0.455	0.457	0.457	0.457	
20	0.454	0.455	0.455	0.455	
25	0.422	0.422	0.422	0.422	
30	0.328	0.328	0.328	0.328	
35	0.187	0.187	0.187	0.187	
40	0.062	0.062	0.062	0.062	

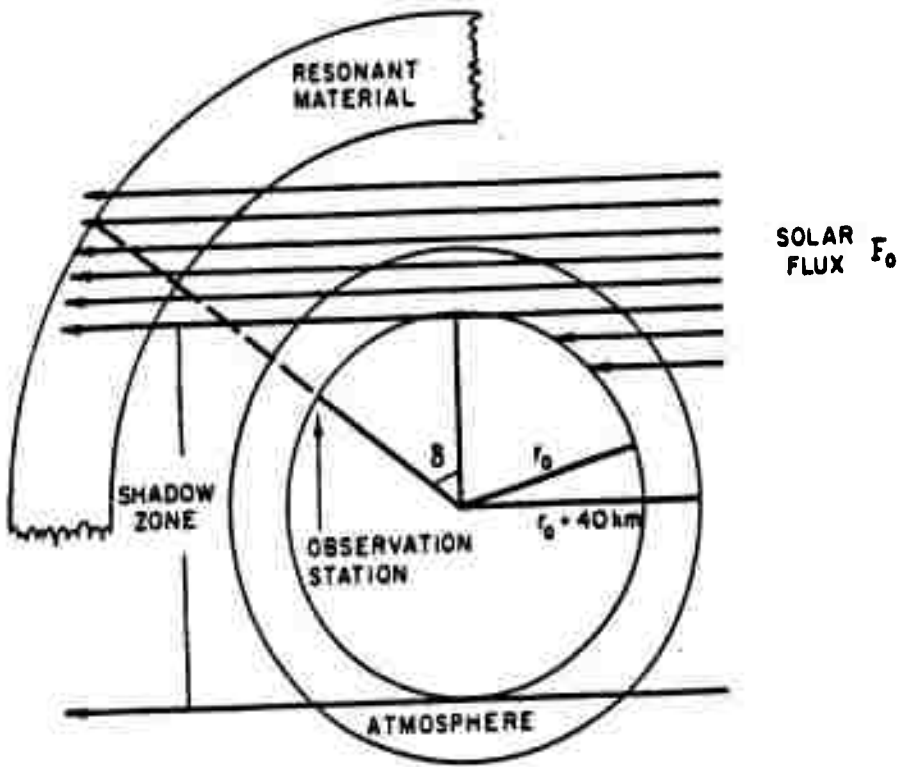


Figure A.1 General geometry of debris observations.

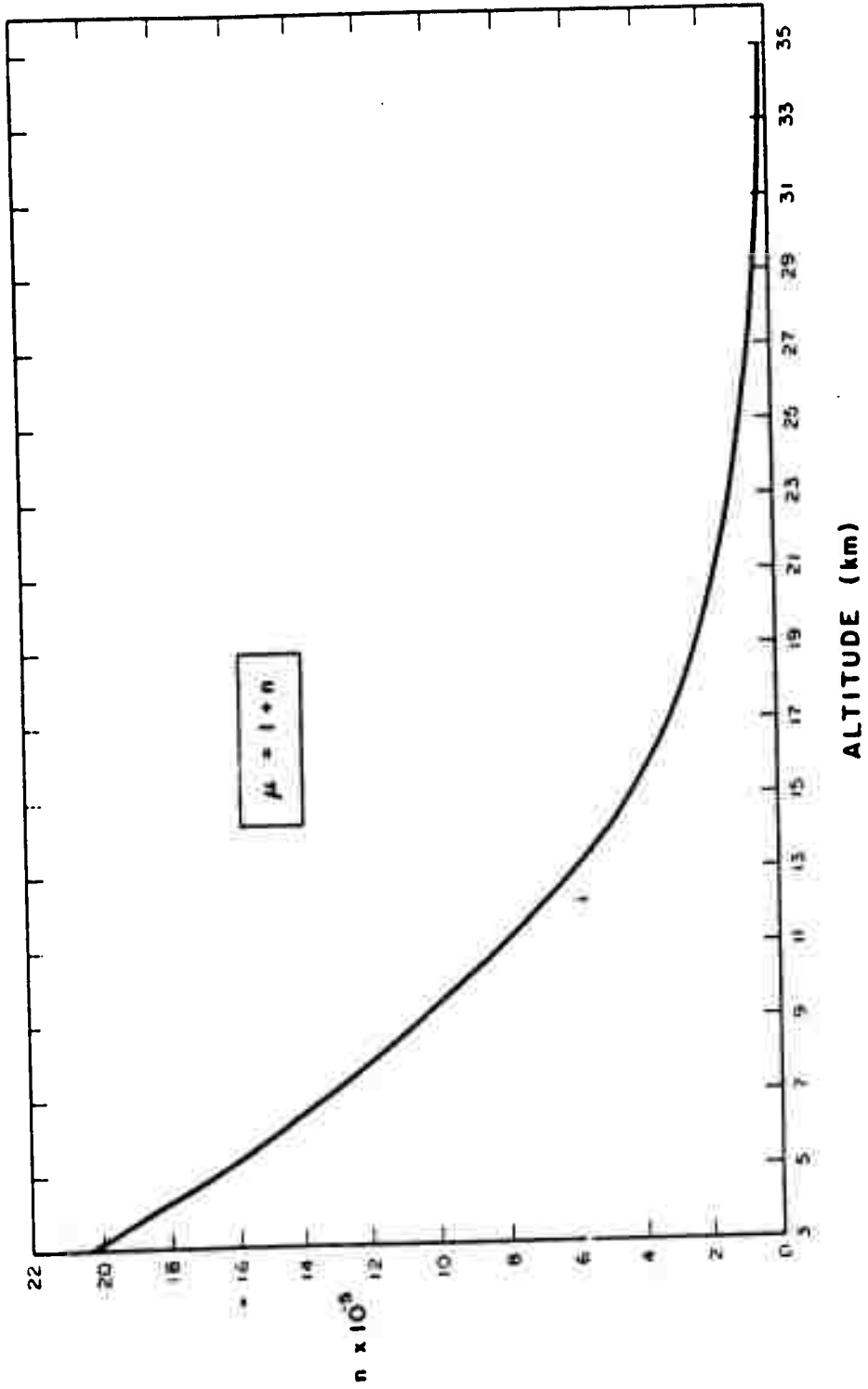


Figure A.2 Index of refraction as a function of altitude.

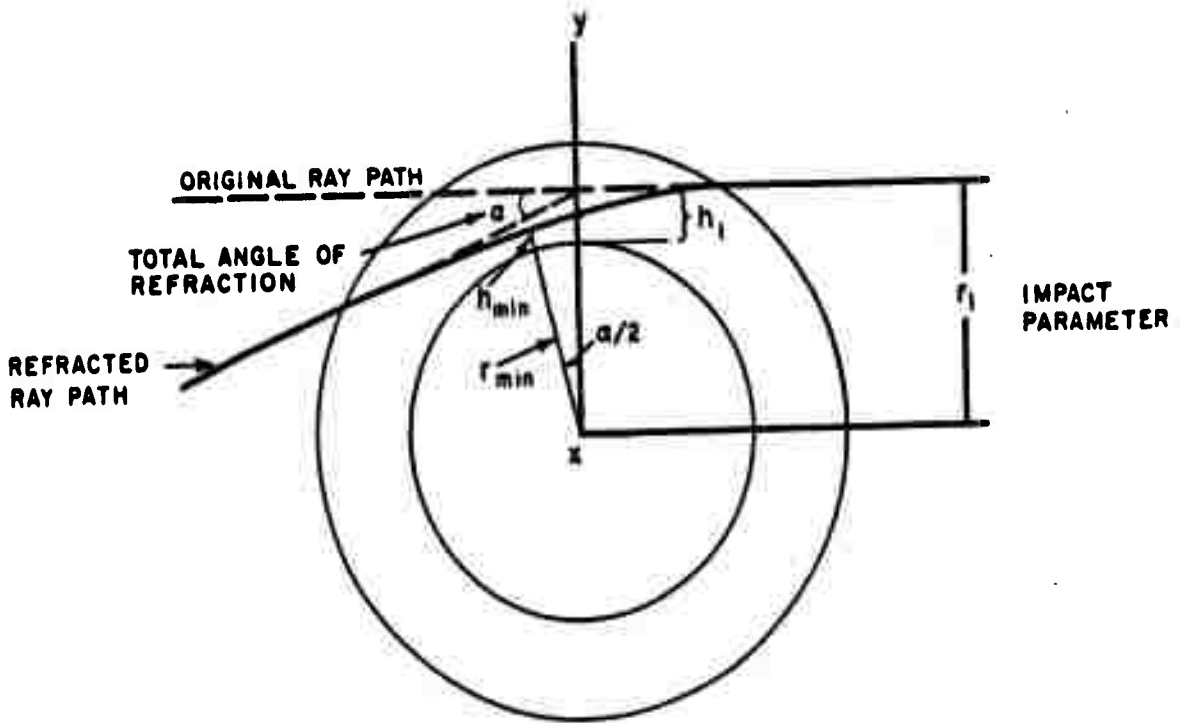


Figure A.3 Passage of light ray through the refracting atmosphere (refractive effects very greatly exaggerated).

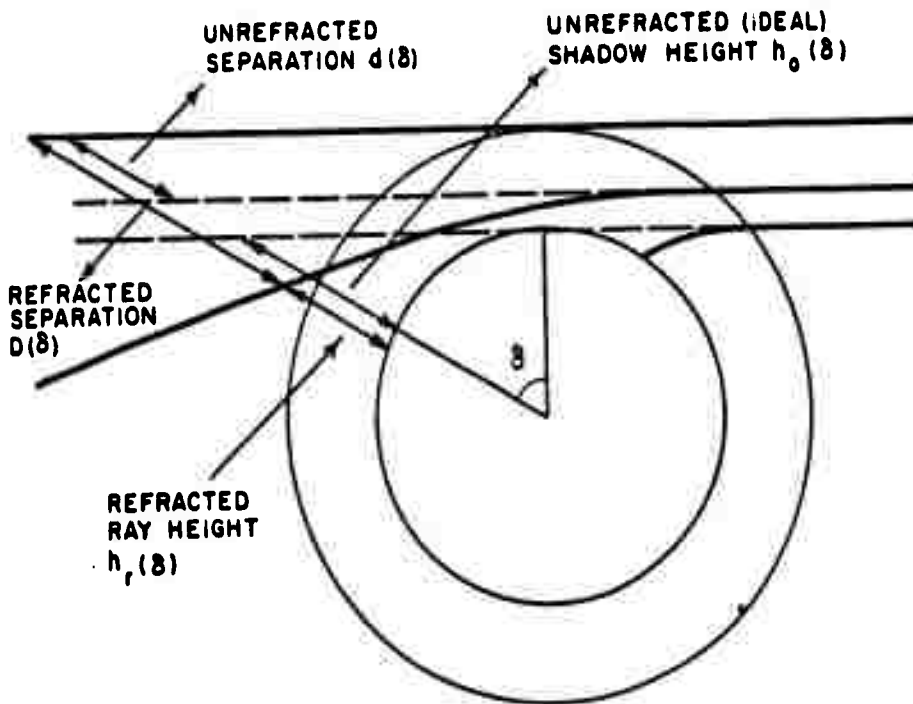


Figure A.4 Ray heights and refractive separations (refractive effects very greatly exaggerated).

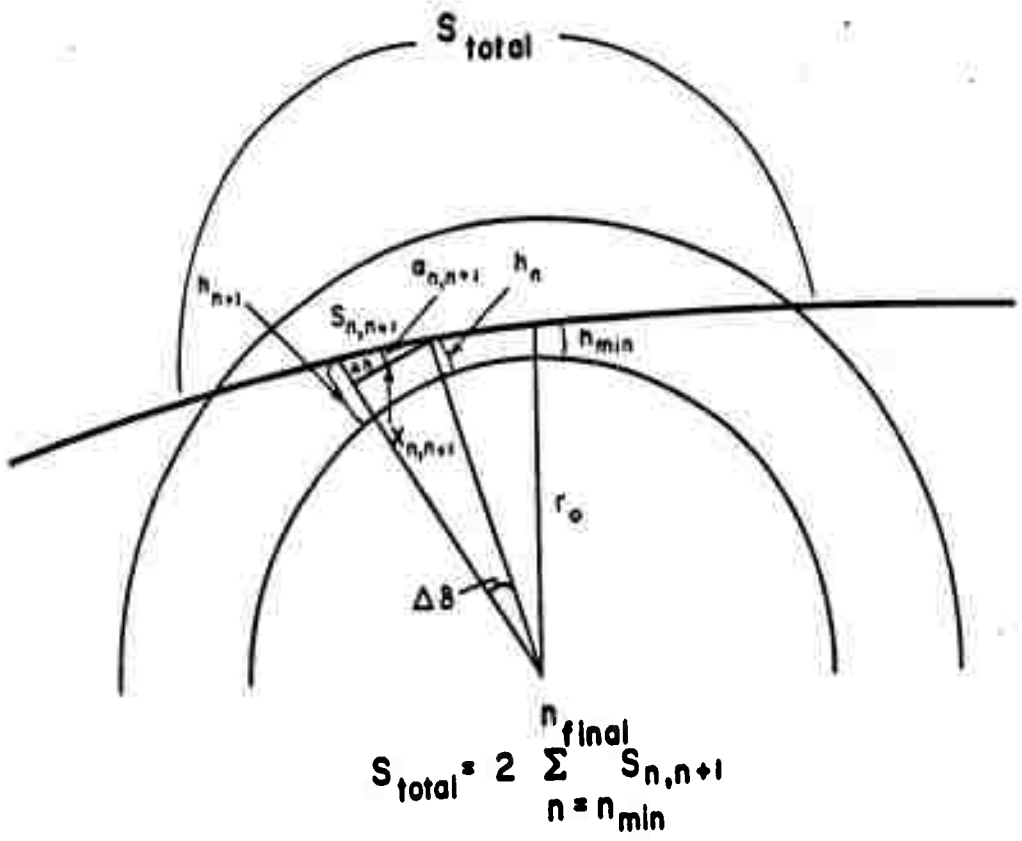


Figure A.5 Method of ray path tracing.

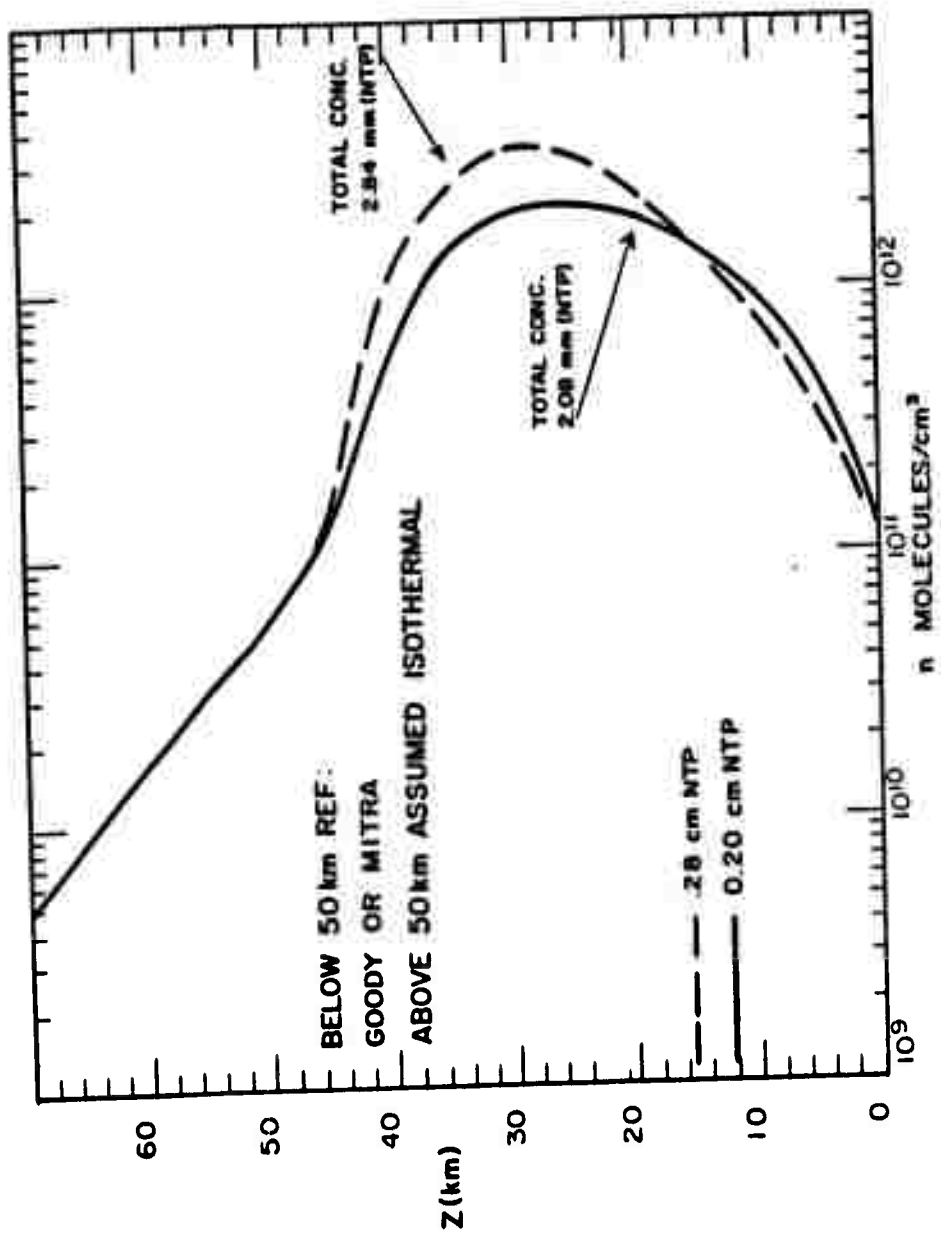


Figure A.6 Ozone concentration models.

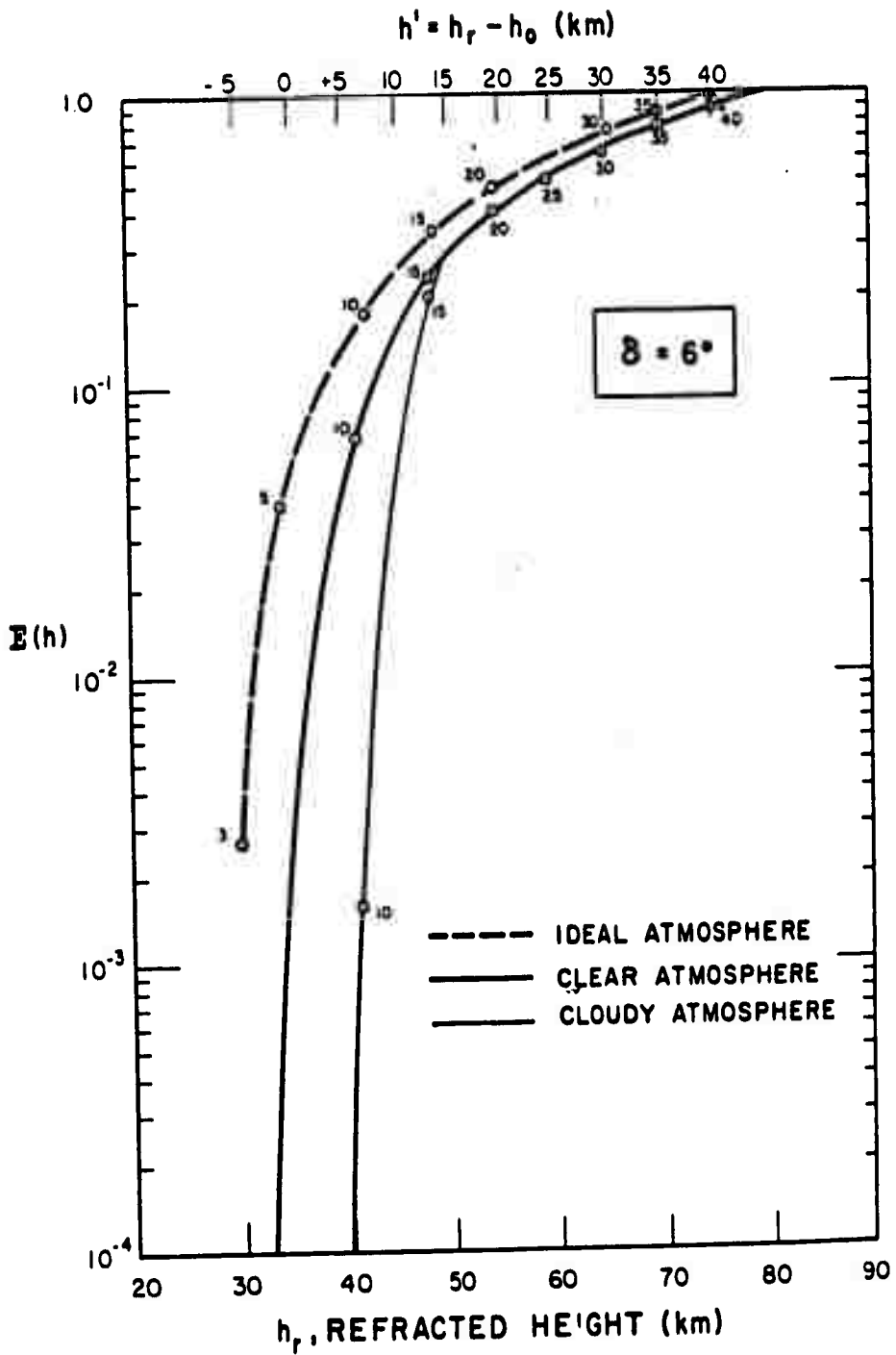


Figure A.7 Solar Illumination curves, 6° solar depression angle.

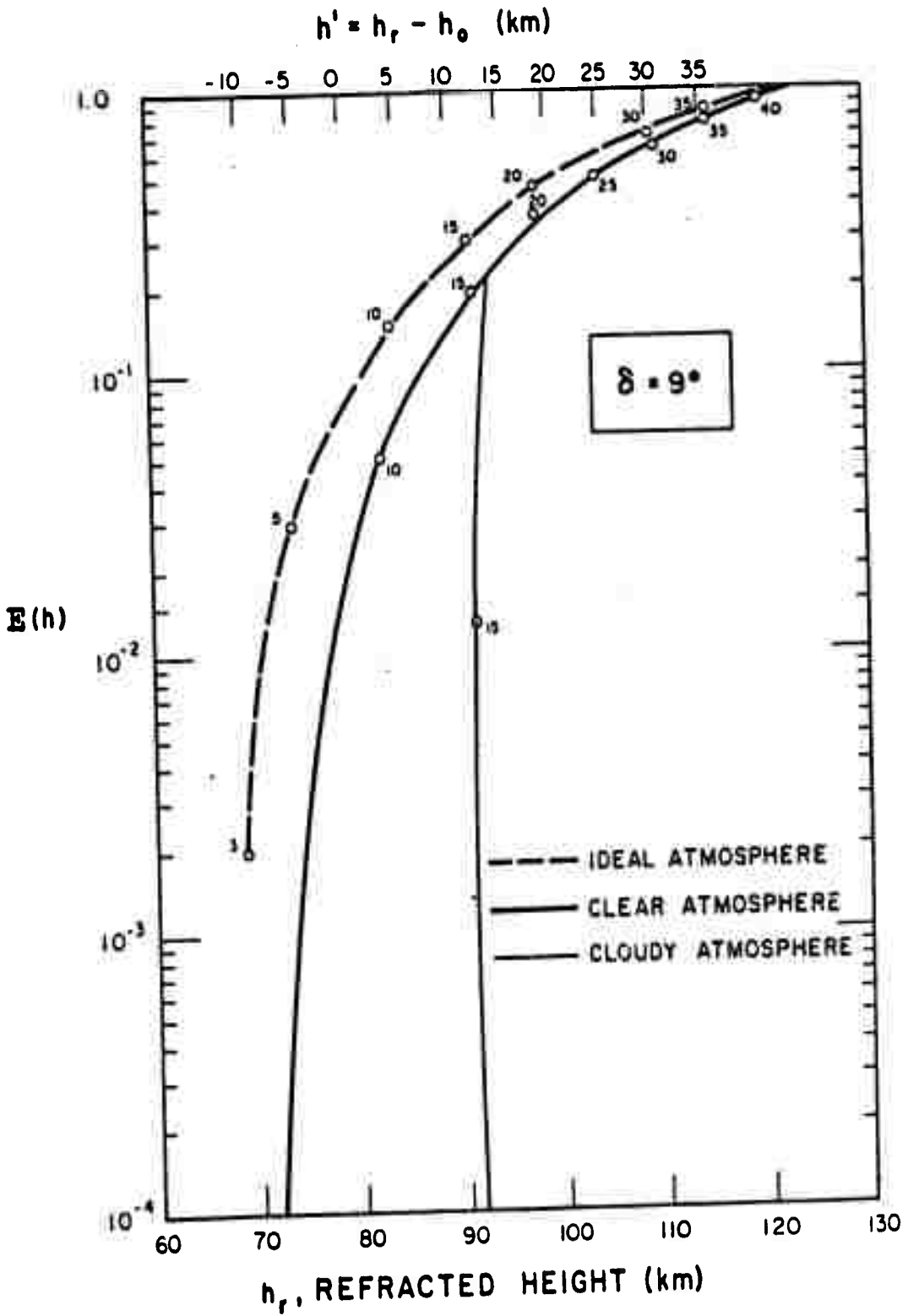


Figure A.8 Solar illumination curves, 9° solar depression angle.

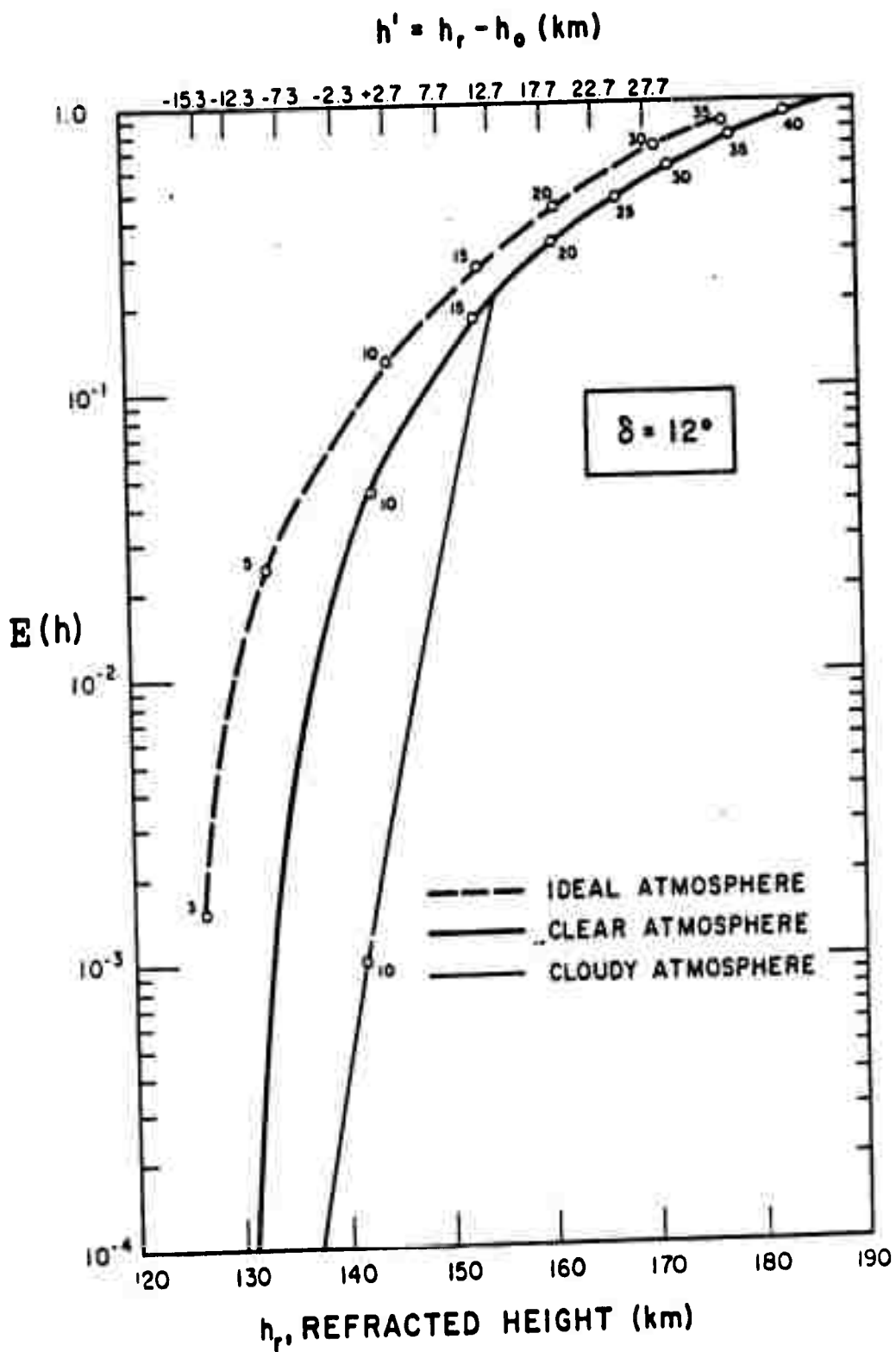


Figure A.9 Solar illumination curves, 12° solar depression angle.

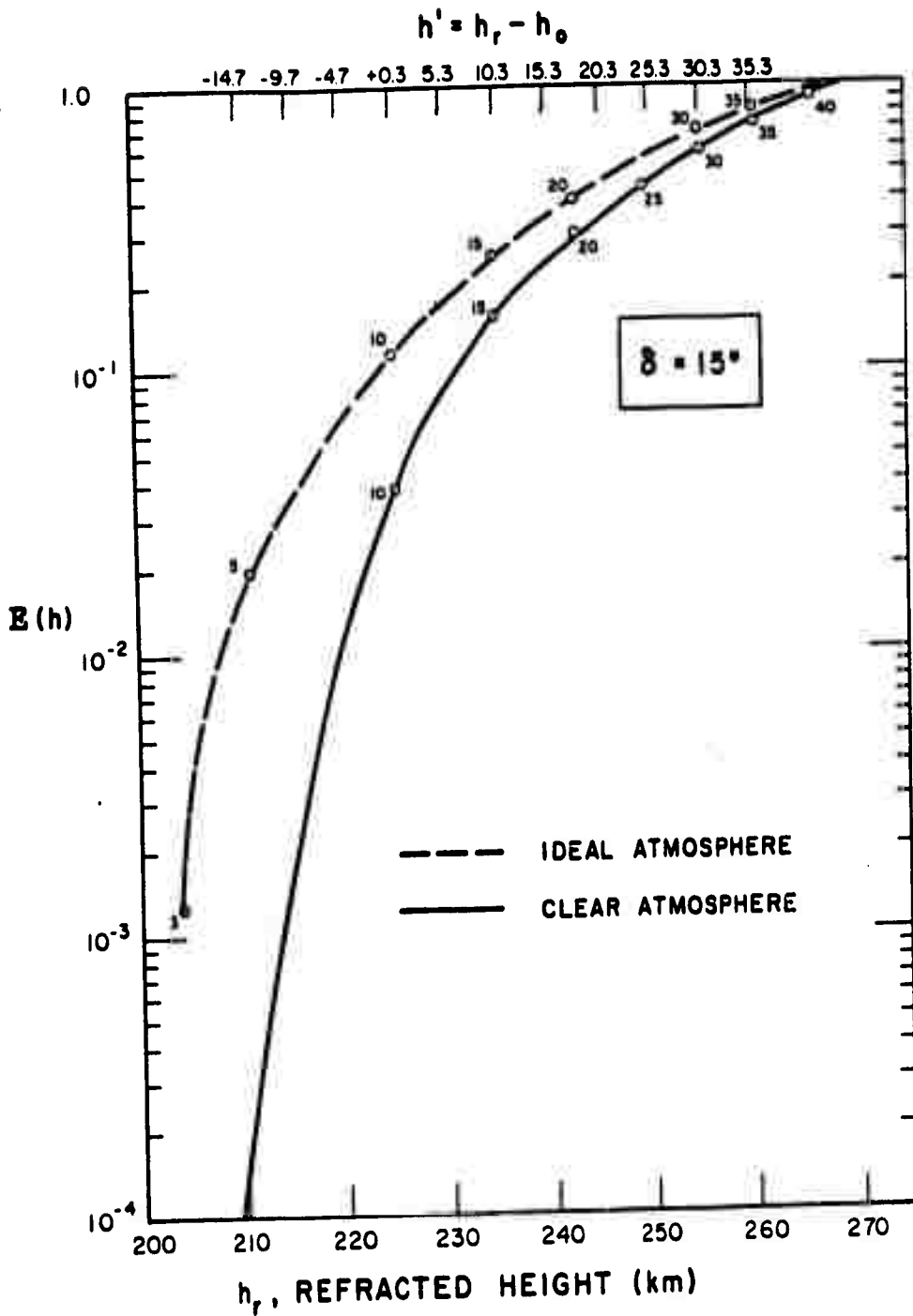


Figure A.10 Solar illumination curves, 15° solar depression angle.

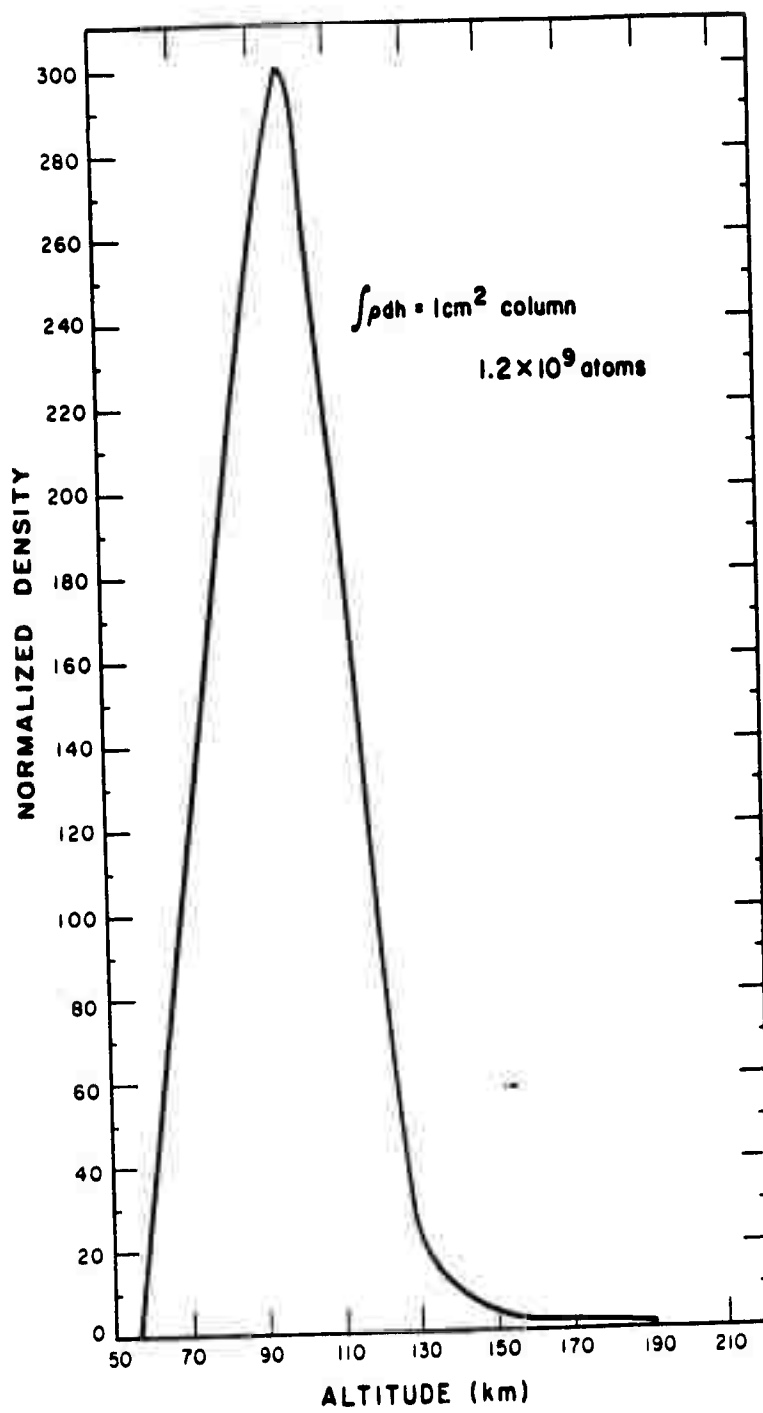


Figure A.11 Upper atmospheric debris model.

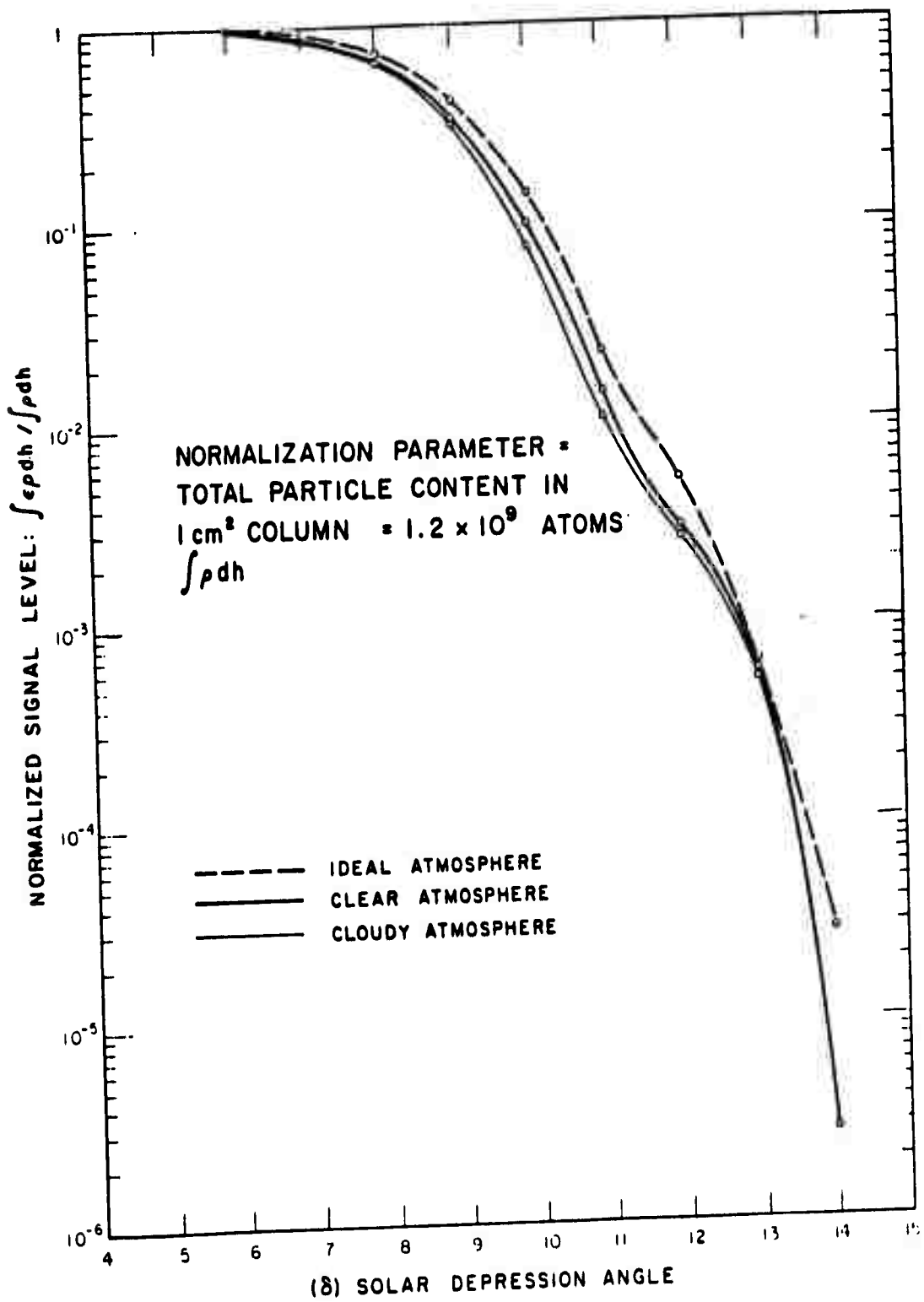


Figure A.12 Photometric signal levels as a function of solar depression.

APPENDIX B

AN EVALUATION OF THE CONCENTRATIONS

This is an evaluation of the concentrations discussed in the main text of this report.

During the course of twilight measurements to determine debris concentrations from resonance scattering, the photometer records an amplitude as a function of time. The relation between the earth's shadow height as a function of time during such measurements, gives the possibility that debris concentration as a function of height may be computed from the photometer records. The main text gives photometer readings taken during Fish Bowl as a function of solar depression angle, and gives concentrations deduced from these measurements by an approximate computational method. It is the purpose of this appendix to evaluate the accuracy of the computational method. It was found that the uncertainty in the reported data, resulting from the approximation in the effective height of the density distribution (ρ -atoms/cm³), was within the overall uncertainty expected from instrument calibration and atmospheric effects.

The reported data were tabulated as a function of intensity (I -atoms/cm²-col) versus solar depression angle (δ) and height (h), where $h = 6371 (\sec \delta - 1)$ kilometers. A first-order exponential interpolation was used between

data points, and several checks showed that no more than a one-percent error was introduced by this process. (See main text for greater detail.)

To obtain a density distribution, a straight numerical differentiation was performed in the integrated intensities according to the following expressions:

$$I(h) = \int_{h_0}^{\infty} \rho(h) dh \text{ atoms/cm}^2\text{-col} \quad (\text{B.1})$$

$$\rho(h_0) = - \frac{dI(h_0)}{dh} \text{ atoms/cm}^3 \quad (\text{B.2})$$

A five-point differentiation formula was used on points tabulated at increments of one kilometer:

$$\frac{dI_0(h)}{dh} = \frac{(I_{-2} - 8I_{-1} + 8I_1 - I_2)}{12 \Delta h} \quad (\text{B.3})$$

This formula is an average of trapezoidal differences that allows the expression of odd-order derivatives in terms of tabulated values at $h \pm \Delta h$ rather than in terms of $h \pm \frac{\Delta h}{2}$. A check was performed by using the calculated values of ρ obtained from Equation B.3 and by approximating the integral (Equation B.1) by a sum:

$$I(h) \text{ calc} = \sum_{j=h_0}^k \rho(j) + C(k) \quad (\text{B.4})$$

where $C(k) = \int_k^{\infty} \rho(h) dh$ = the integrated intensity above
k kilometers.

In summing the calculated values of ρ , it was found that the error between the tabulated data $I(h)$ and the calculated intensities $I(h)$ calc did not exceed 10 percent, and it averaged approximately 4.5 percent.

In plotting the calculated densities [Equation B.3] versus height, twenty kilometers was added to each tabulated height in order to arrive at the best estimated effective shadow height as determined from the atmospheric solar illumination coefficient (ϵ) (Appendix A). To evaluate the validity of this single height adjustment to all points in the data, a process using the numerical differentiation with the illumination coefficients incorporated was performed on several sets of data.

For the purposes of this investigation, a density distribution, $\rho_E(h)$, was assumed that possibly could have existed in the atmosphere after a high-altitude nuclear event. Whether or not this distribution actually existed is not definitely known; however, it is not of importance in the evaluation of the mathematical approximations.

The integrated concentration, $I_{\text{obs}}(h)$, that would have been observed with the photometer had this $\rho_E(h)$ existed can be computed directly according to the following expressions:

$$I_{\text{obs}}(h) = \int_{h_0}^{\infty} \epsilon(h) \rho_E(h) dh \text{ atoms/cm}^2 \cdot \text{col} \quad (\text{B.5})$$

$$\approx \sum_{j=h_0}^k \epsilon(j) \rho_E(j) + C(k) \quad (\text{B.6})$$

The atmospheric illumination coefficients, (ϵ) , used in Equation B.6 were average values for 'five-kilometer increments (Figure .1), and represent a screening layer forty kilometers in thickness applicable to solar depression angle from six to sixteen degrees. The effect of this screening layer in all cases is to lower the apparent height above which a given integrated concentration occurs.

The first density distribution

$$\rho_{\text{calc}}^1(h) = \frac{d I_{\text{obs}}(h)}{dh} + 20 \text{ km} \quad (\text{B.7})$$

was obtained with Equation B.3), and the twenty-kilometer adjustment employed to arrive at the best first approximation (Figure B.2). A point-by-point comparison with $\rho_E(h)$ shows that the $\rho_{\text{calc}}^1(h)$ is ten percent greater at 170 km, a factor

of four greater at 120 km , and 34 percent less than $\rho_E(h)$, at 90 km.

In order to obtain a second and closer approximation to $\rho_E(h)$, a process of iteration was employed in the following manner. Operating directly on the first approximation $\rho_{\text{calc}}^1(h)$ with the ϵ coefficients, a new integrated intensity is summed:

$$I_{\text{calc}}^1(h) = \sum_{j=h_0}^k \epsilon(j) \rho_{\text{calc}}^1(j) + C(k) \quad (\text{B.8})$$

The second approximation $\rho_{\text{calc}}^2(h)$ is then computed:

$$\rho_{\text{calc}}^2(h) = \rho_{\text{calc}}^1(h) + \frac{d[I_{\text{obs}}(h) - I_{\text{calc}}^1(h)]}{dh} \quad (\text{B.9})$$

The results of this computation are also seen in Figure B.2. A comparison with $\rho_E(h)$ indicates that the second approximation $\rho_{\text{calc}}^2(h)$ is converging for points above approximately 105 km, but diverging for points less than this height.

A similar computation was performed starting with the same $\rho_E(h)$ distribution except that the first approximation was

$$\rho_{\text{calc}}^{\text{la}}(h) = \frac{d I_{\text{obs}}(h)}{dh} \quad (\text{B.10})$$

without the 20-km adjustment to estimate the effect of the solar illumination coefficient. This initial approximation assumes no atmospheric effects, i.e., a sharply defined shadow line where ϵ was equal either to unity or zero.

Figure B.3 shows $\rho_{\text{calc}}^{1a}(h)$ in this instance is consistently low, by a factor of 3 at 160 km, a factor of 5 at 110 km, and 64 percent at 80 km. An iteration process (Equation B.9) showed that $\rho_{\text{calc}}^{2a}(h)$ is converging to $\rho_E(h)$ at all points, although there is still a substantial difference in magnitude at a given height.

Figure B.4 shows the results of operating in a similar manner for a first approximation to a density distribution quite unlike $\rho_E(h)$. This arbitrary distribution $[\rho_x(h)]$ covers two orders of magnitude in a height of less than twenty kilometers and may be likened to the concentration of free sodium atoms occurring in the atmosphere. The first approximation $\rho_{x\text{-calc}}(h)$ differs from $\rho_x(h)$ by a factor of eight at the maxima of the distribution and by as much as a factor of fifteen at the upper end of the concentration. A twenty-kilometer adjustment would be entirely inappropriate in this case and would result in even greater differences in magnitude and location of the maxima of the assumed concentration.

The results of the investigations on these three sets of data may be interpreted in the following manner:

CASE I (Figure B.2). When the ratio of the height of the particle distribution to the thickness of the screening layer operating on that distribution is large (\geq a factor of three) and the ϵ coefficients are very nearly a linear function over this screening layer, then a twenty-kilometer height adjustment ($h = 6371 (\sec \delta - 1) + 20$ km) to the densities as derived from measured intensities (Equation B.2) would give the best first approximation to the actual particle distribution in the atmosphere. Since there is no single valued constant of proportionality applicable to all heights of the distribution, the agreement between $\rho_E(h)$ and $\rho_{calc}^1(h)$ is less in the middle portion of the distribution than it is at either end. It is of importance that the agreement near the maxima of the concentration is within fifty percent. It is felt that the uncertainty resulting from this method of approximating the effective height of the density distributions reported in the main text is within the overall uncertainty expected from instrument calibration and atmospheric effects.

The method of iteration employed to compute $\rho_{calc}^2(h)$ resulted in a second approximation that was closer to $\rho_E(h)$ except at the lower portion of the distribution. This

computation was hampered at this point by the use of the five-point numerical differentiation formula and a dh of five kilometers that resulted in the loss of four data points with each differentiation. The computation on this portion of the curve where the shape is changing rapidly is extremely sensitive to small errors and an extrapolation of the data is not advisable. However, with the proper choice of formulas, height increment (dh), and exactness in the computations, it is expected that successive iterations should increasingly succeed to approximate the original distribution. Inherent in the application of this method is a smoothing operation on the calculated intensities between successive iterations, i.e., restrictions dictated by the physical phenomena involved. These boundary conditions are such as (1) particle density cannot be negative although it may be zero at a given height, and (2) sharp changes in the shape of density curves vs. height are highly unlikely to occur in the differential height used (in this case 5 km which is very much less than the scale height of the measured species at these altitudes). These restrictions serve to eliminate the fluctuations introduced by the inexactness of the input data and the resulting instabilities in the differentiation processes.

CASE II (Figure B.3). The methods employed were the same in this case as in Case I with the exception of the 20-km height adjustment to the first approximation. Although $\rho_{\text{calc}}^{1a}(h)$ is equal to or slightly better than $\rho_{\text{calc}}^1(h)$ as a first approximation in the center portion of the curves (~ 120 km), it is not as close at all other points on the curve. If the criteria of comparison of these approximations to $\rho_E(h)$ were the area between the curves instead of a point-to-point magnitude ratio, $\rho_{\text{calc}}^1(h)$ in Case I would still be the best first approximation to $\rho_E(h)$. The result of an iteration, $\rho_{\text{calc}}^{2a}(h)$, shows that the curve is approaching $\rho_E(h)$ at all points, and the comments on this process in Case I are relevant here.

CASE III (Figure B.4). This example points out the inadequacies of the methods employed in Cases I and II to a distribution with a thickness much less than that of the screening layer. A differential height of one km was used in this case in an attempt to give a fine resolution to the rapidly changing densities. However, by any criteria, $\rho_{x\text{-calc}}(h)$ is a poor approximation to $\rho_x(h)$. Fortunately, most of the data reported in the main text does not fall in this category.

For future applications, an extension of the techniques of data reduction methods discussed in this paper is the use of electronic differentiation directly on the analog or digital signal as received from the photometer. With the proper use of calibration factors and the elimination of obviously inconsistent data (due to weather, instrumental difficulties) an approximation of the density distribution may be obtained from the integrated intensity measured in the field. The magnitude of the concentration of the species as well as the height determination can only be as accurate as the degree with which the solar coefficients (ϵ) are known.

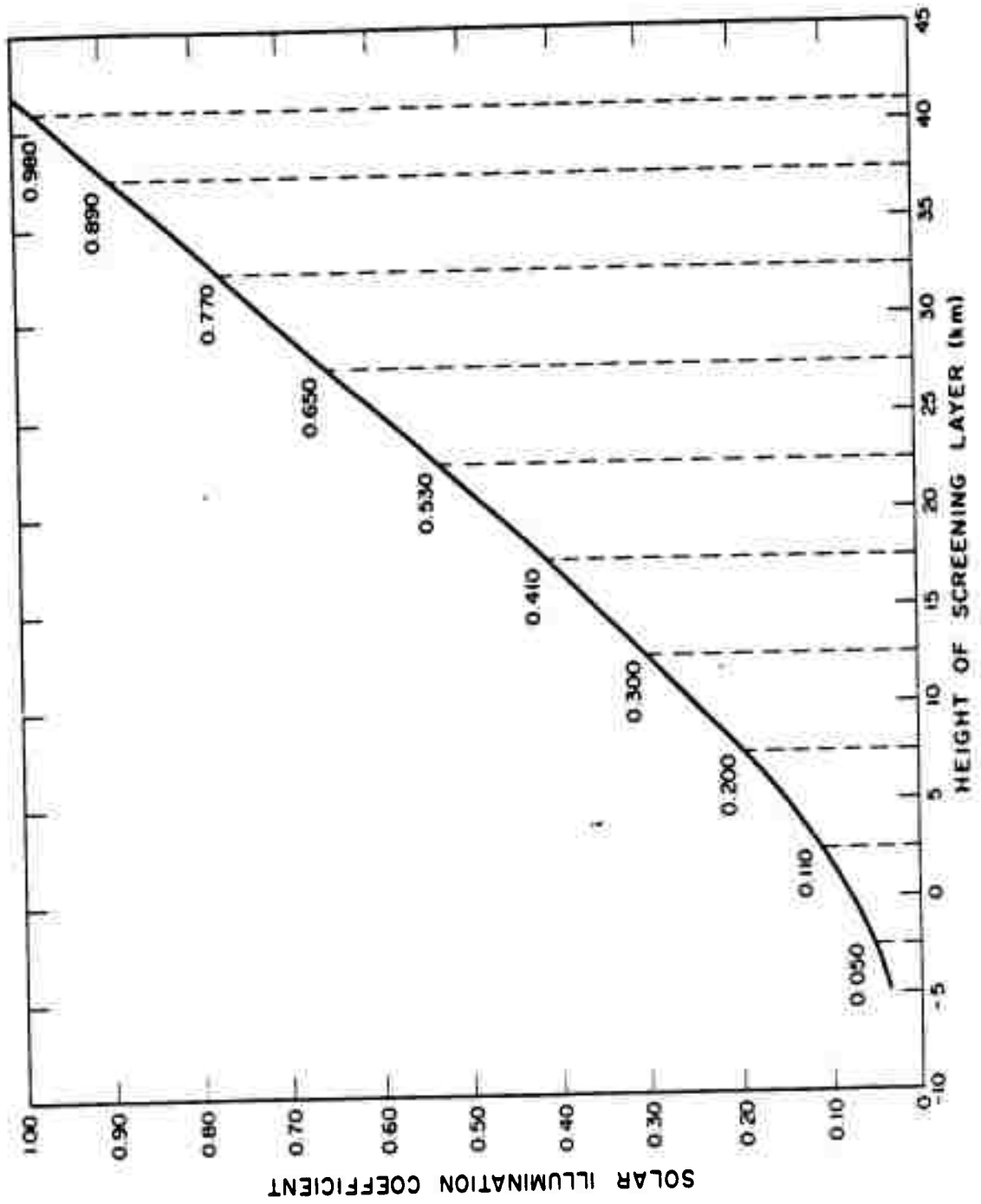


Figure B.1 Solar illumination coefficient (ϵ); average values for SDA 6 through 16 degrees.

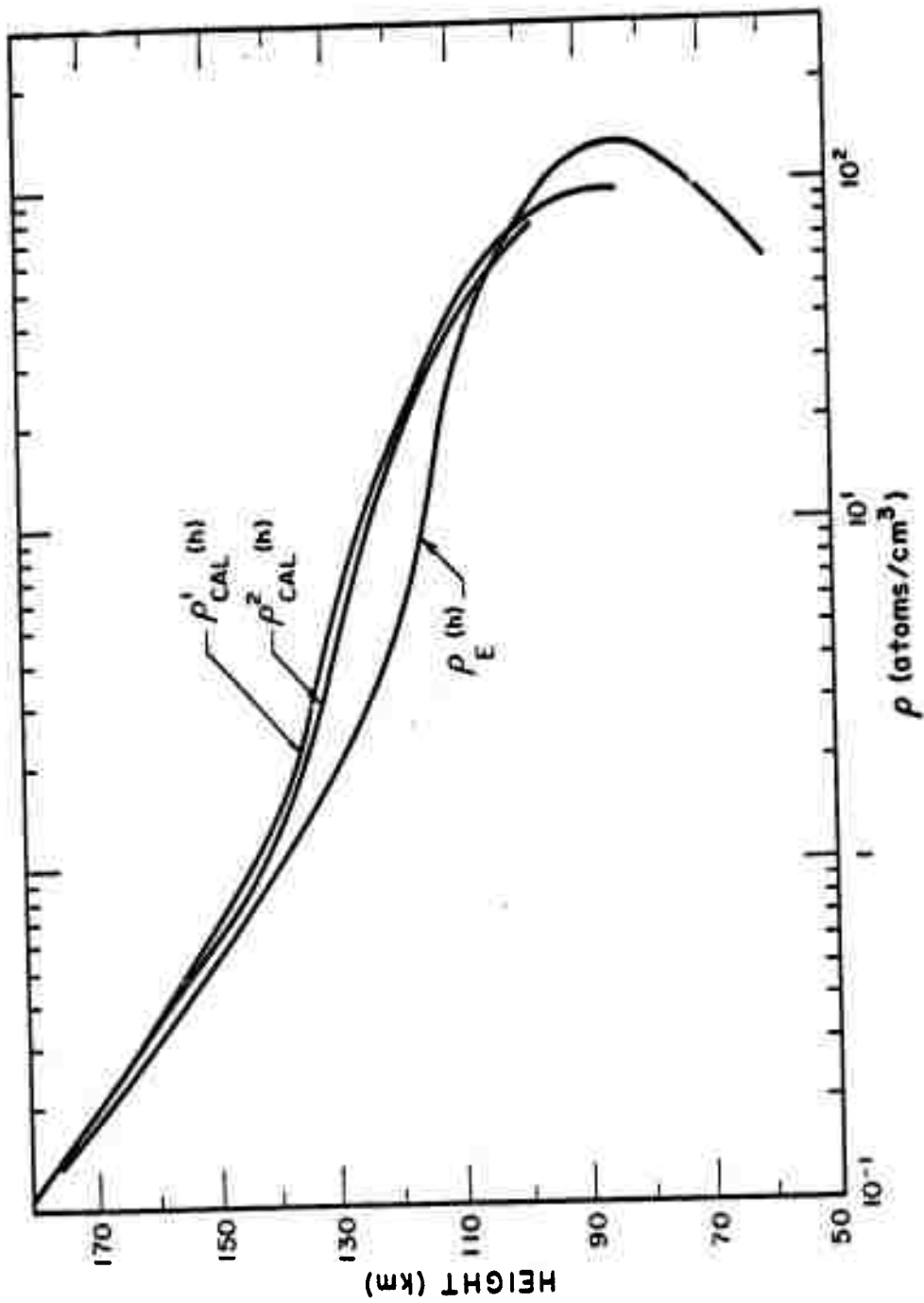


Figure B.2 Density distribution, Case I.

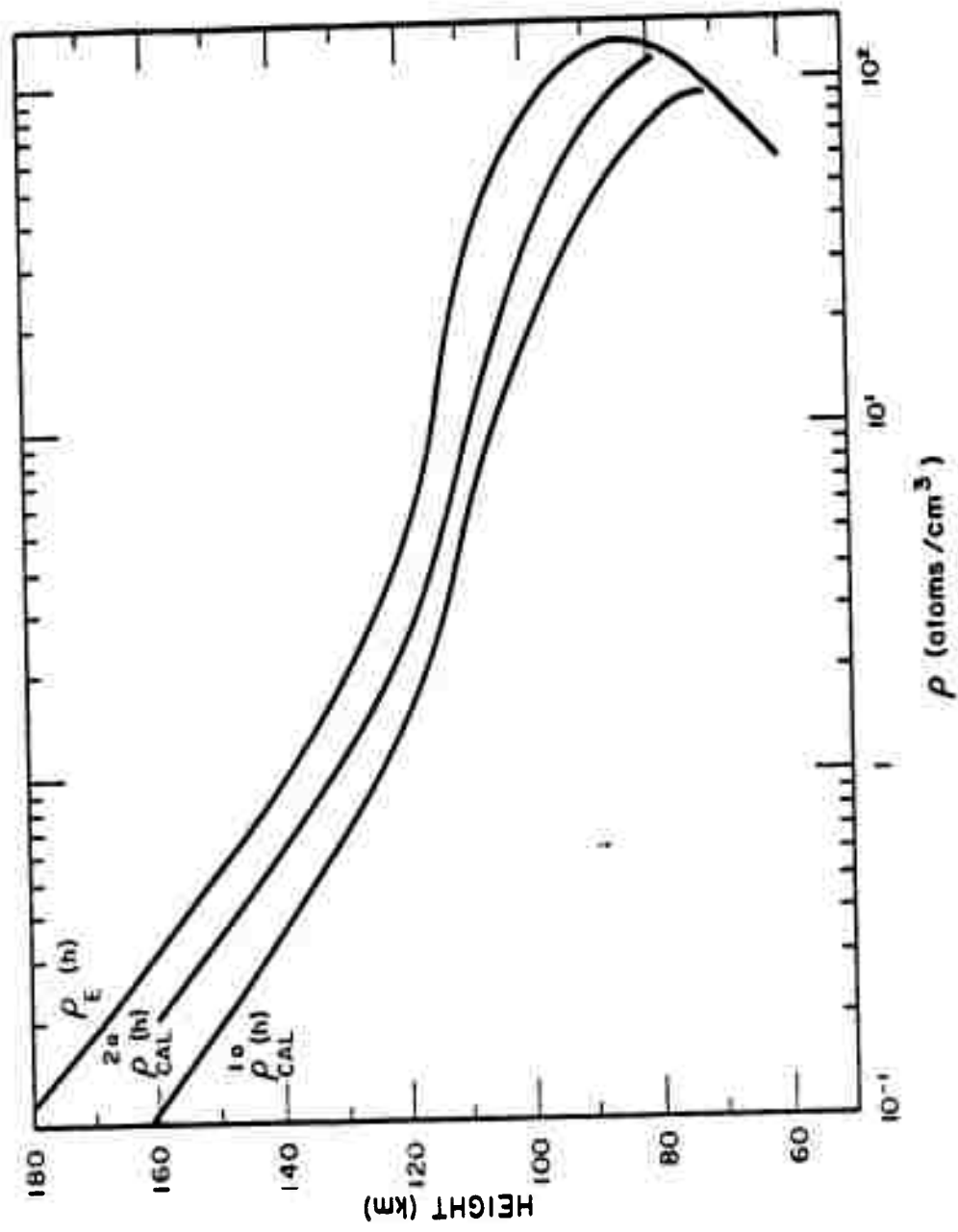


Figure B.3 Density distribution, Case II.

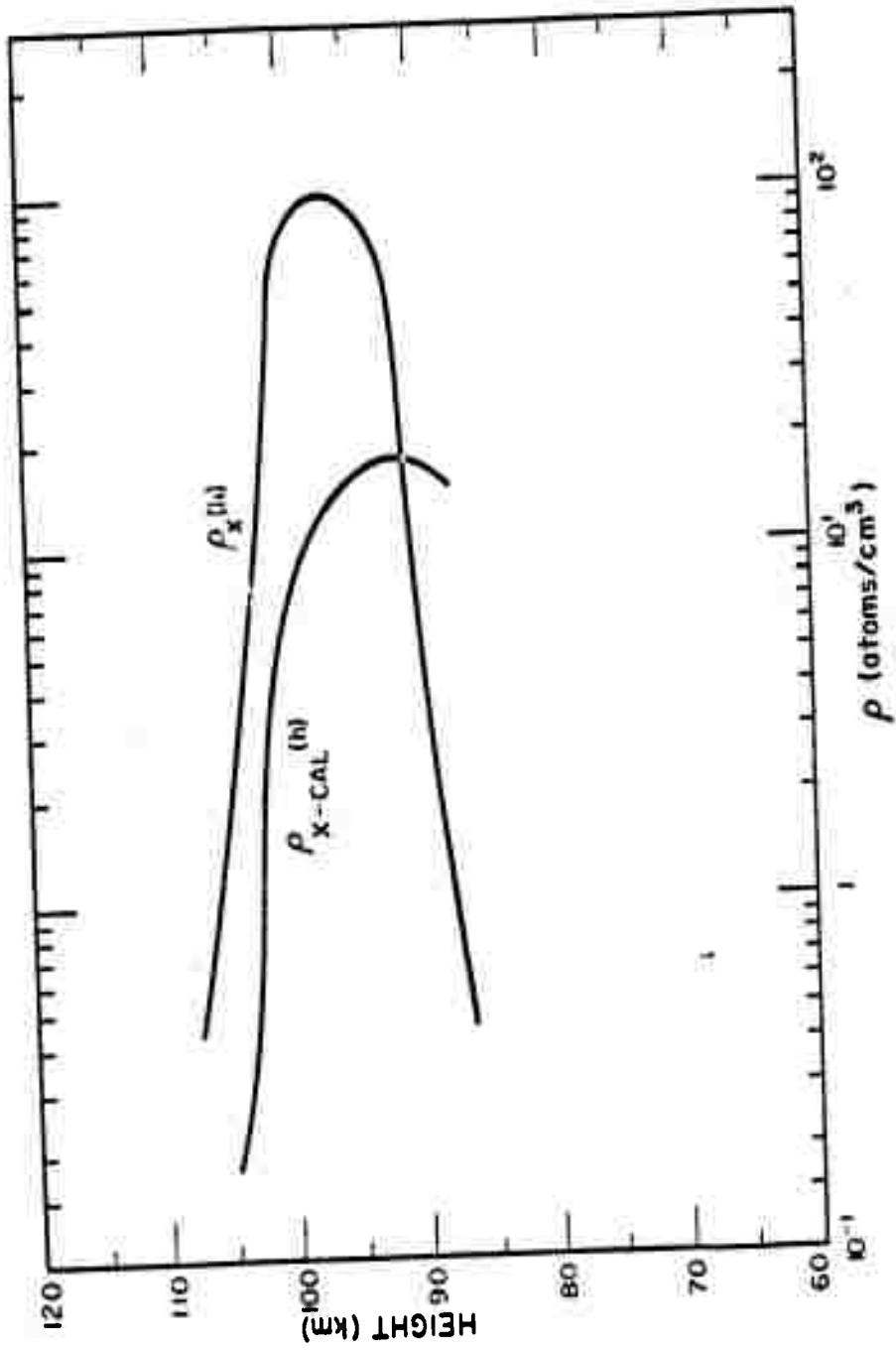


Figure B.4 Density distribution, Case III.

APPENDIX C

DETERMINATION OF THE RELATIVE INTENSITY OF PHOTON FLUX CAUSED BY NUCLEAR DEBRIS-RESONANCE SCATTERING

This is an extension of the determination of the relative intensity of the photon flux caused by nuclear debris resonance scattering first reported in Project Vela—Nuclear Debris Detection by Resonance Scattering of Sunlight, GCA Technical Report No. 61-42-A, Part I.

C.1 GENERAL EQUATION FOR THE PHOTON FLUX

In case of resonance scattering, the number of photons P emitted per atom per sec is proportional to the original photon flux ϕ , measured in photons/sec $\text{cm}^2 \text{ \AA}$.

$$P = \alpha \phi \quad (\text{C.1})$$

The factor α has the dimension cm^3 and is designated for the present work as the absorption coefficient for the transition in question and defined by

$$\alpha = \frac{g_2}{g_1} \cdot \frac{A_{2-1}}{8\pi C} \cdot \lambda^4 \quad (\text{C.2})$$

where g_i is the statistical weight of the term

$$g_i = 2J_i + 1 \quad (\text{C.2a})$$

$$i = 1, 2$$

with

J_1 the total angular momentum of the lower term

J_2 the total angular momentum of the upper term

A_{2-1} the transition probability for emission of the line in question

C the speed of light

and λ the wavelength of the line emitted.

(Details of the derivation of this equation can be found in the "Vela Report" pages 115-117.)

If R_e is the relative abundance of one particular fission product (number of atoms of this particular element produced per 50 fission events), the total photon flux scattered isotropically by this element will be for N fission events

$$F = \frac{P \cdot R \cdot N}{50} \quad (C.3)$$

Considering the fact that the detection device has a quantum efficiency η and disregarding geometrical consideration, the relative intensity of the signal can be determined by

$$\bar{S}_r = \eta \cdot F = \eta \cdot P \cdot R_e \cdot \frac{N}{50} \quad (C.4)$$

In order to compare the signals resulting from different species it is necessary to compare the values of \bar{S}_r and not only the absorption cross sections α which may lead to completely erroneous conclusions. Combinations of Equations (C.2) and (C.4) yield for the number of photons emitted per 50 fission events

$$\bar{S}_r = \frac{1}{8\pi C} \cdot \eta \cdot \frac{g_2}{g_1} \cdot A \cdot \lambda^4 \cdot R_e \cdot \frac{N}{50} \cdot \phi \quad (C.5)$$

Dimensions:

Using the cgs system, the following dimensions for the different parameters have to be used as mentioned in the table below:

<u>Symbol</u>	<u>Magnitude</u>	<u>Dimensions</u>
C	3×10^{10}	$\left[\frac{\text{cm}}{\text{sec}} \right]$
η	var. from 0 to 1	$\left[\frac{\text{unit signal}}{\text{photons}} \right]$
g_1	var. from 0 to 10	dimensionless
g_2	var. from 0 to 10	dimensionless
A	var. from 10^7 to 10^9	$\left[\frac{1}{\text{sec}} \right]$
λ	var. from 3×10^{-5} to 8×10^{-5}	[cm]
R_e	var. from 0 to .15	dimensionless
N	-----	dimensionless
ϕ	var. from 2×10^{21} to 6×10^{21}	$\left[\frac{\text{photons}}{\text{cm}^2 \cdot \text{sec} \cdot \text{cm wavelength interval}} \right]$

C.2 DETERMINATION OF ABUNDANCE OF FISSION PRODUCTS

The relative abundance of the major fission products was determined as follows:

- (1) The total fission yields per mass number (i.e., number of atoms of a particular mass number produced per 100 fission events) as listed in Column 2 of Table C.1

was taken from References 36 and 37.

(2) The decay schemes for every fission product were examined, and the stable end product for every mass number was determined. In every single case, there was only one stable end product per mass number; therefore, the total fission yield for a particular mass number could be interpreted as the fission yield for a particular isotope. The fission yields of these isotopes are listed in Column 4 of Table C.1. A blank in Column 4 next to an isotope, indicates that this isotope is not present in nuclear debris.

(3) The relative abundance of all the major fission products are listed in Column 5 of Table C.1.

Relative abundance R_1 of an isotope is defined as the number of atoms of this particular isotope per 100 atoms produced by nuclear fission. Because ternary fission (division into three fragments) is very rare (5×10^{-6} per binary fission) (Reference 38), the relative abundance of a stable element is just $\frac{1}{2}$ of the fission yield for the particular mass number of this element; in other words the relative abundance can also be defined as number of stable isotopes of

one particular mass number produced per 50 fission events.

(4) The relative abundance R_e of the different elements were determined by adding up all the abundances of the respective isotopes as shown in Table C.2. Again the definition of relative abundance of an element is the number of atoms of this particular element out of 100 atoms produced by fission or the number of atoms per 50 fission events.

C.3 DETERMINATION OF RESONANCE ABSORPTION CROSS SECTION

The values of α as defined by Equation (C.2) and published in the Vela Report were originally computed from theoretically obtained values of A (transition probabilities), because no reliable experimental data were available at that time for the elements in question. In the meantime, however, a comprehensive table of experimentally determined transition probabilities was published (Reference 39).

Resonance lines of the elements in question were examined, but only those were used which have a $g_2 \cdot A$ value greater than or approximately equal to 1.0. The results of these calculations are given in Table C.3.

In order to evaluate the different resonance lines, the relative signal strength S_r was calculated by

multiplying α of an individual element with its relative abundance, and with ϕ , the solar flux density. $S_r(\lambda, Z)$ can be interpreted as the number of photons of wavelength λ (resonance line of the element Z) scattered into the solid angle of 4π by the atoms of the fission product Z produced by 50 fission events.

The wavelength dependence of the sensitivity of the detection device is characterized by the value of η (quantum efficiency of typical photo cathode S-20). The observable relative signal strength \bar{S}_r then becomes

$$\bar{S}_r = S_r \cdot \eta$$

\bar{S}_r yields a realistic value for comparison of the different intensities. \bar{S}_r multiplied by the attenuation factor and the solid angle of the detection device gives the absolute value for the observed signal.

C.4 DISCUSSION

A comparison of the \bar{S}_r values leads to the selection of the lines in Table C.3.

It was desirable to have a pair of strong resonance lines for every selected element, one line of the neutral state and one of the element ion. Unfortunately, this is

only the case for Sr and Ba. Furthermore, the ion lines are weaker by at least one order of magnitude or more. This, on the other hand, is compensated by the fact that at least initially (up to approximately 48 hours) the ion concentration in the debris may exceed the neutral atom concentration by approximately a factor of 100.

The resonance lines for the Mo and Nd ions are in the far UV and therefore unsuitable for optical observations.

Table C.3 gives several values for comparison. Column 3 lists the value of α which is designated as the cross section for resonance absorption. The general value is of the order of 10^{-22} cm³. Column 4 lists the number of photons/sec scattered from the sunlight by one atom of the particular element. Column 5 lists the number of photons/sec scattered from the sunlight by 1 kg of the element in question. Column 6 gives the number of photons/sec scattered from the sunlight by the amount of atoms of a particular element produced by a fission device of 1-kt yield. This number was

obtained by using the well-known value

$$1 \text{ kt} \rightarrow 1.45 \times 10^{23} \text{ fission events}$$

This value, multiplied by the relative abundance of the fission product and the number of photons/sec scattered per atom of this fission product, yields this value listed in Column 6. Column 7 gives the quantum efficiency or relative phototube sensitivity for the best now available photocathode S-20. The values from Column 5 and Column 6 multiplied by this quantum efficiency give an adjusted signal strength as listed in Columns 8 and 9. For the fission products, such as Al and Li, only the number of photons/sec kg are listed for comparison.

In the case of U, an efficiency for fission of 80 percent was assumed. This gives a relative abundance of 20 percent for uranium in the debris. This fraction seems to be an average value and therefore can be used as a good approximation.

Note: All values listed in Columns 5, 6, 8 and 9 are the number of atoms scattered into the total solid angle 4π . Also, no adjustments have been made for attenuation of radiation by the lower part of the atmosphere.

TABLE C.1 FISSION YIELDS PER MASS NUMBER

Mass Number	Total Fission Yield For Mass Number (%)	Stable Element Present	Fission Yield For Stable Element (%)	Relative Abundance of Isotope (Total Number of Isotopes Created by Fission)
84	1.0	Kr ⁸⁴	1.0	0.5
		Sr ⁸⁴	-	-
85	1.3	Rb ⁸⁵	1.3	0.65
86	2.0	Kr ⁸⁶	2.0	1.0
		Sr ⁸⁶	-	-
87	2.5	Sn ⁸⁷	-	-
		Rb ⁸⁷	2.5	1.3
88	3.6	Sr ⁸⁸	3.6	1.8
89	4.8	Y ⁸⁹	4.8	2.4
		Sr ⁸⁹	-	-
90	5.8	Zr ⁹⁰	-	-
		Sr ⁹⁰	5.8	2.9
91	5.8	Zr ⁹¹	5.8	2.9
92	6.0	Zr ⁹²	6.0	3.0
		Mo ⁹²	-	-
93	6.5	Nb ⁹³	-	-
		Zr ⁹³	6.5	3.3
		Mo ⁹³	-	-
94	6.4	Zr ⁹⁴	6.4	3.2
		Mo ⁹⁴	-	-
		Nb ⁹⁴	-	-
95	6.3	Mo ⁹⁵	6.3	3.1
96	6.3	Zr ⁹⁶	6.3	-
		Ru ⁹⁶	-	-
97	6.1	Mo ⁹⁷	6.1	3.0
		Tc ⁹⁷	-	-

TABLE C.1 (Continued)

Mass Number	Total Fission Yield For Mass Number (%)	Stable Element Present	Fission Yield For Stable Element (%)	Relative Abundance of Isotope (Total Number of Isotopes Created by Fission)
98	5.8	Mo ⁹⁸	5.8	2.9
		Tc ⁹⁸	-	-
		Ru ⁹⁸	-	-
99		Tc ⁹⁹	6.06	3.0
100	6.3	Mo ¹⁰⁰	6.3	3.1
		Ru ¹⁰⁰	-	-
101	5.0	Ru ¹⁰¹	5.0	2.5
102	4.1	Ru ¹⁰²	4.1	2.0
		Pd ¹⁰²	-	-
103	3.0	Rb ¹⁰³	3.0	1.5
104	1.8	Ru ¹⁰⁴	1.8	0.9
		Pd ¹⁰⁴	-	-

TABLE C.1 (Continued)

Mass Number	Total Fission Yield For Mass Number (%)	Stable Element Present	Fission Yield For Stable Element (%)	Relative Abundance of Isotope (Total Number of Isotopes Created by Fission)
129	0.9	I ¹²⁹ Xe ¹²⁸	0.8	0.4
130	2.0	Te ¹³⁰ Xe ¹³⁰ Ba ¹³⁰	2.0	1.0
131	2.9	Xe ¹³¹	2.9	1.5
132	4.4	Xe ¹³² Ba ¹³²	4.4	2.2
133	6.6	Cs ¹³³ Ba ¹³³	6.6	3.3
134	7.9	Xe ¹³⁴ Ba ¹³⁴	8.1	4.0
135	6.4	Cs ¹³⁵ Ba ¹³⁵	6.4	3.2
136	6.5	Xe ¹³⁶ Ba ¹³⁶ Ce ¹³⁶	6.5	3.2
137	6.1	Cs ¹³⁷ Ba ¹³⁷ La ¹³⁷	6.1	3.0
138	5.7	Ba ¹³⁸ La ¹³⁸ Ce ¹³⁸	5.7	2.8

TABLE C.1 (continued)

Mass Number	Total Fission Yield For Mass Number (%)	Stable Element Present	Fission Yield For Stable Elements (%)	Relative Abundance of Isotope (Total Number of Isotopes Created by Fission)
139	6.2	La ¹³⁹	6.5	3.2
		Ce ¹³⁹		
140	6.4	Ce ¹⁴⁰	6.4	3.2
141	6.0	Pr ¹⁴¹	6.0	3.0
142	5.0	Ce ¹⁴²	6.0	3.0
		Nd ¹⁴²		
143	6.0	Nd ¹⁴³	6.0	3.0
144	5.7	Ce ¹⁴⁴		
		Nd ¹⁴⁴	5.6	2.8
		Sm ¹⁴⁴		
145	4.0	Nd ¹⁴⁵	4.0	2.0
		Pm ¹⁴⁵		
146	3.1	Nd ¹⁴⁶	3.0	1.5
		Sm ¹⁴⁶		
147	2.4	Pm ¹⁴⁷	2.4	1.2
		Sm ¹⁴⁷		
148	1.7	Nd ¹⁴⁸	1.7	0.9
		Sm ¹⁴⁸		
		Cd ¹⁴⁸		
149	1.1	Sm ¹⁴⁹	1.1	0.5
150	0.7	Nd ¹⁵⁰	0.7	0.4
				<u>49.3</u>

TABLE C.2 RELATIVE ABUNDANCE OF DIFFERENT ELEMENTS

M/Z	36 Kr	37 Rb	38 Sr	39 Y	40 Zr	41 Nb	42 Mo	43 Tc	44 Ru	45 Rh	46 Pd
84	.5										
85		.8									
86	1.0										
87		1.3									
88			1.8								
89			(2.3)→2.3								(50d)
90			2.9								
91					2.9						
92					3.0						
93					3.3						
94					3.2						
95							3.1				
96							3.1				
97							3.0				
98							2.9				
99								3.0			
100							3.1				
101									2.5		
102									2.0		
103									(1.5)→1.5		(41d)
104									9		
TOTAL	1.5	2.1	4.7 (7.0)	2.3	12.4		15.2	3.0	5.4 (6.9)	1.5	→ 48.1

TABLE C.2 (Continued)

M Z	52 Te	53 I	54 Xe	55 Cs	56 Ba	57 La	58 Ce	59 Pr	60 Nd	61 Pm	62 Sm	
129		0.4										
130	1.0											
131			1.5									
132			2.2									
133				3.3								
134			4.0									
135					3.2							
136			3.2									
137					3.0							
138					2.8							
139						3.2						
140							3.2					
141								3.0				
142							3.0					
143							.		3.0			
144									2.8			
145									2.0			
146									1.5			
147										1.2		
148									.9			
149											0.5	
150									.4			
TOTAL	1.0	0.4	10.9	3.3	9.0	3.2	6.2	3.0	10.6	1.2	0.5	49.3%

TABLE C.3 RESONANCE LINES OF ELEMENTS

	1	2	3	4	5	6	7	8	9
Element	λ \AA	α 10^{-23} cm^3	Photons atom, sec	Photons kg, sec 10^{24}	Photons 1 KT, sec $\cdot 10^{21}$	PM Tube Sensitivity	Adjusted Photons kg, sec 10^{24}	Adjusted Photons 1 KT, sec 10^{21}	
Sr I	4607	52	2.5	17.2	35	.19	3.3	6.6	
Sr II	4215	8	0.3	2.4	4.1	.20	0.5	0.8	
Mo I	3864	14	0.3	2.0	10.0	.20	0.4	2.0	
Ba I	5535	246	13.2	58.0	350.0	.11	6.4	38.5	
Ba II	4554	7.5	0.33	1.45	8.6	.19	0.28	1.6	
Nd I	4955	13	0.65	2.7	20	.16	0.43	3.2	
	4925	17	0.85	3.5	26	.16	0.56	4.2	
	4634	14	0.70	2.9	22	.19	0.48	4.2	

REFERENCES

1. J. E. Blamont; "Observations de l'emission atmospherique des raies du sodium au moyen d'un appareil a balayage magnetique"; The Aurora and the Airglow, 1955; edited by E. B. Armstrong and A. Dalgarno, Pergamon Press; Unclassified.
2. R. Dunn and E. Manring; "Recording Night Sky Photometer of High Spectral Purity"; J.O.S.A., 1956, Vol. 46, Page 572; Unclassified.
3. E. Manring and others; "Some Wind Determinations in the Upper Atmosphere Using Artificially Generated Sodium Clouds"; J. Geophys. Res., 1959, Vol. 64, Page 587; Unclassified.
4. J. Bedinger, E. Manring, and S. Gosh; "Study of Sodium Vapor Ejected into the Upper Atmosphere"; J. Geophys. Res., 1958, Vol. 63, Page 19; Unclassified.
5. R. J. Jenkins and E. Manring; "The Design, Construction and Operation of Ground-Based Tracking Equipment for Experiments Utilizing Optical Trace Materials to Study Atmospheric Parameters"; GCA Tech. Rpt. 61-2-N, March 1961, Contract No. NAS5-215; Geophysics Corporation of America, Bedford, Massachusetts; Unclassified.

6. E. Manring and others; "Upper Atmospheric Wind Profiles Determined from Three Rocket Experiments"; GCA Tech. Rpt. 61-1-N, February 1961, Contract No. NAS5-215; Geophysics Corporation of America, Bedford, Massachusetts, 'Unclassified.

7. E. Manring and H. Knaflich; "Some Measurements of the Coefficient of Diffusion in the Upper Atmosphere"; GCA Tech. Rpt. 61-3-N, March 1961, Contract No. NAS5-215; Geophysics Corporation of America, Bedford, Massachusetts; Unclassified.

8. J. Pressman, F. Marmo, and L. Aschenbrand; "Artificial Electron Clouds VI: Low Altitude Study, Release of Cesium at 69, 82 and 91 km"; Planet. Space Sci., 1960, Vol. 2, pages 228-237; Unclassified.

9. L. Pauling and E. Wilson; "Introduction to Quantum Mechanics"; McGraw-Hill, N.Y., 1935; Unclassified.

10. E. Condon and G. Shortley; "The Theory of Atomic Spectra"; Univ. Press, Cambridge, Mass., 1957; Unclassified.

11. P. Nawrocki and R. Papa; "Atmospheric Processes"; Geophysics Corporation of America, Bedford, Mass., 1961, Unclassified.

12. J. Bedinger, E. Manring, and S. Gosh; J. Geophys. Res., 1958, Vol. 63, Page 19; Unclassified.
13. W. Schottsky, Ann. Physik, 1918, Vol. 57, Page 541; Unclassified.
14. A. Ljunghall; "The Intensity of Twilight and Its Connection with the Density of the Atmosphere"; Meddlelande Fran Lunds Astronomiska Observatorium, 1948, Vol. 125, Pages 7-170; Unclassified.
15. E. V. Ashburn; "The Density of the Upper Atmosphere and the Brightness of the Twilight Sky"; J. Geophys. Res., 1952, Vol. 57, Pages 85-93; Unclassified.
16. J. J. Reesnick; "The Measurement of Twilight"; Physicas Grav., 1944, Vol. 11, Pages 61-77; Unclassified.
17. F. Volz, and R. N. Goody; "Twilight Intensity at 20° Elevation"; Sci. Rpt. No. 1, Prepared by Harvard Med. Obs. for AFCRC under Contract No. AF19(604)4546, 1960; Air Force Cambridge Research Center, Bedford, Mass.; Unclassified.
18. R. Penndorf; J.O.S.A., 1957, Vol. 47, Page 176; Unclassified.
19. R. Tousey and E. O. Hulburt; J.O.S.A., 1947, Vol. 37, Page 78; Unclassified.

20. J. A. Debrowolski; J.O.S.A., 1959, Vol. 49, Page 794;
Unclassified.
21. R.B. Dunn and E. R. Manring; J.O.S.A., 1956, Vol. 46,
Page 572; Unclassified.
22. J. W. Evans; J.O.S.A., 1949, Vol. 39, Page 229;
Unclassified.
23. B. Lyot; Ann. Astrophys., 1944, Vol. 7, Page 31;
Unclassified.
24. H. P. Klein and K. Yu; "Calculations of the Diffusion
of Small particles in a non-Uniform Atmosphere"; GCA Tech. Rpt.
62-1-G, July 1962, Contract No. DA-49-146-XZ-075; Geophysics
Corporation of America, Bedford, Massachusetts; Unclassified.
25. J. W. Chamberlain; "Physics of the Aurora and
Airglow"; Academic Press, 1961, New York; Unclassified.
26. D. M. Hunten; "A Study of Sodium in Twilight";
Journal of Atmospheric and Terrestrial Physics"; 1954, Vol 5,
Pages 44 - 56; Unclassified.
27. Link and Frantesek; "Eclairment Crepusculaire en
Luminere Jaune 5893Å"; Studie Geophysiques and Geodesie,
1958, Vol 2, Pages 47 - 53; Unclassified.
28. V. G. Fesenkov; "On the Optical State of the
Atmosphere Illuminated by Twilight"; Soviet Astronomy, 1959;
Vol 3, Pages 207 - 213; Unclassified.

29. F. E. Volz and R. M. Goody; "The Intensity of Twilight and Upper Atmospheric Dust"; Journal of the Atmospheric Sciences, 1962, Vol 19, Pages 385 - 406; Unclassified.

30. J. C. Johnson; "Physical Meteorology"; Technology Press of M.I.T. and John Wiley, Inc., 1954, New York; Unclassified.

31. D. H. Menzel; "Optical Refraction in a Planetary Atmosphere"; GCA Report 61-33-A, July 1961; Unclassified.

32. A. Engelman and L. Colin; "An Analysis of the Time and Space Scale Problems in Radio Meteorology"; Astia No. AD-131-392, December 1957, Rome Air Development Center; Unclassified.

33. Handbook of Geophysics; the MacMillan Co., New York, 1960; Unclassified.

34. J. A. Curcio and others; "Atmospheric Scattering Coefficients in the Visible and Infrared Regions"; Journal of the Optical Society of America, 1962, Vol 52, Page 1010; Unclassified.

35. S. K. Mitra; "The Upper Atmosphere"; The Asiatic Society, 1952, Calcutta; Unclassified.

36. W. H. Sullivan; "Trilinear Chart of Nuclines"; Oak Ridge National Laboratory (January 1959).

37. Seymour Katcoff; "Fission Product Yields from Neutron-Induced Fission"; Nucleonics, November 1960, Vol 18, p. 203.

38. I. Kapian; "Nuclear Physics"; P. 490; Addison-Wesley Publishing Company, 1956.

39. C.H. Corliss and W.R. Bozman; "Experimental Transition Probabilities"; NBS Monograph 53, July 20, 1962.